

CHAPTER 1

INTRODUCTION

The Southeastern Aerosol and Visibility Study (SEAVS) was conducted from July 15, 1995 through August 25, 1995 in Great Smoky Mountains National Park. The study was a collaborative effort between several universities, consulting firms, the Electric Power Research Institute (EPRI), and the National Park Service (NPS). This report, however, focuses primarily on summarizing the work conducted by the NPS sponsored groups. The report includes: (1) the optical and meteorological measurements made by Air Resource Specialists, Inc. (ARS), (2) the aerosol chemical composition and size distribution measurements made by the University of California at Davis (UCD), and (3) the measurements of aerosol hygroscopicity made by Colorado State University (CSU).

The overall objectives of this group's research efforts were to: (1) better understand the physical, chemical, and overall optical characteristics of the ambient aerosol under the humid conditions observed in the southeastern United States during the summer months and how these characteristics related to visibility issues. Specific technical objectives included:

- Document the intensity of haze and estimate the contributions of scattering and absorption components to the total light extinction.
- Compare the chemical composition data from the IMPROVE sampler with data from other sampling systems.
- Document the chemical composition of the aerosol and identify each components contribution to mass and light extinction.
- Document the aerosol size distribution, how the distribution changes in time, and how these changes impact scattering efficiencies.
- Measure the hygroscopic properties of the ambient aerosol and compare measured water uptake to theoretical model predictions.

Chapter 1 of this report gives an overview of the study, explains the study's objectives, and describes the sampling site. Chapter 2 overviews the measurements that were made by the NPS group of researchers, illustrates the instrument and sampler configurations, and explains the field measurement protocol of the samplers and instruments. Chapter 3 summarizes calibrations of the various instruments, the uncertainty of the measurements, and the quality assurance procedure enlisted for this study. Chapter 4 gives the results of the measurements of aerosol hygroscopicity. Chapter 5, in general, is composed of data analyses and gives the results of various model calculations, which were compared to the measurements made during the study.

CHAPTER 2

INSTRUMENTATION

All instrumentation and particle samplers operated during the SEAVS study for the National Park Service (NPS), except the transmissometer, were located either in the fenced compound or in the NPS trailer. Figure 2.1 shows: (1) the fenced compound in which there are three sampler stands mounted on a concrete slab, (2) the meteorological instrument tower, and (3) the NPS trailer (located in the background). The sampler stands had roofs to protect the instruments and samplers from precipitation and excess heating by direct sunlight. Sampler stands A and B (the Stanford and nephelometer stands, respectively) had rain gutters and downspouts so rainwater runoff would not contaminate the aerosol samples being collected. The roofs also served to protect technicians, aerosol samples, and log sheets while filters were being changed during inclement weather. Although the stands had roofs, they were open on the sides and ends to allow free ventilation of air through the shelter.

The IMPROVE particulate samplers obtained sample aerosol via inlets through the roof of the stand as shown in Figure 2.2. The samplers were mounted on the east and west facing sides of the shelter. The samplers' pumps were located under the floor of the sampler stand to reduce noise levels and to minimize the possibility of sample contamination from the pumps' exhaust. Figure 2.3 shows the east side of the nephelometer stand. The nephelometers obtained sample aerosol via the open west side of the shelter. The nephelometers' pumps were housed in ventilated and insulated boxes located on the floor of the stand. Carbon vane rotary pumps were used during SEAVS for the nephelometers; therefore, their exhaust was filtered and ported out of the box near ground level on the north side of the shelter.

Campbell 21X data loggers with storage modules were used to: (1) collect data from most of the instruments, (2) control regularly timed events such as clean air calibrations of the nephelometers, and (3) to input voltage to various sensors. Data from most instruments and sensors was logged by the 21X and stored on its accompanying storage module using two-minute averages. The two minute averaged data from the various loggers was subsequently sent to a central computer in the NPS trailer and stored in a single ASCII file. A second computer was used to copy and store the data as a data backup system. Data was displayed by the central computer in real time, which aided in detection of malfunctioning instruments and sensors.

2.1 METEOROLOGICAL MEASUREMENTS OVERVIEW

Surface meteorological data including temperature, relative humidity, barometric pressure, wind speed, wind direction, and solar radiance, were collected continuously during SEAVS.

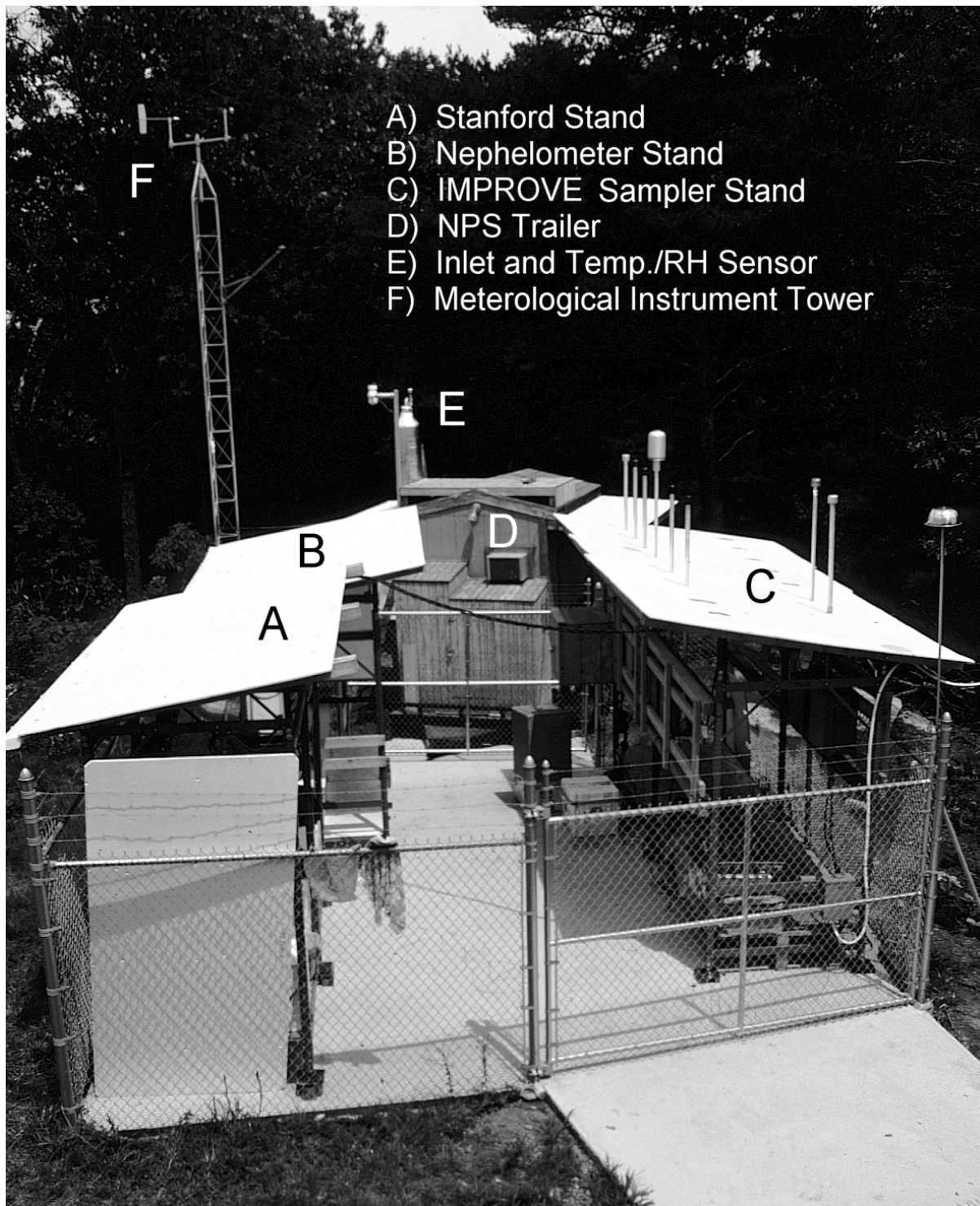


Figure 2.1 NPS fenced compound showing: (A) the Stanford sampler stand, (B) the nephelometer stand, (C) the IMPROVE sampler stand, (D) the NPS trailer with aerosol inlet (E) on roof, and (F) the meteorological instrument tower.

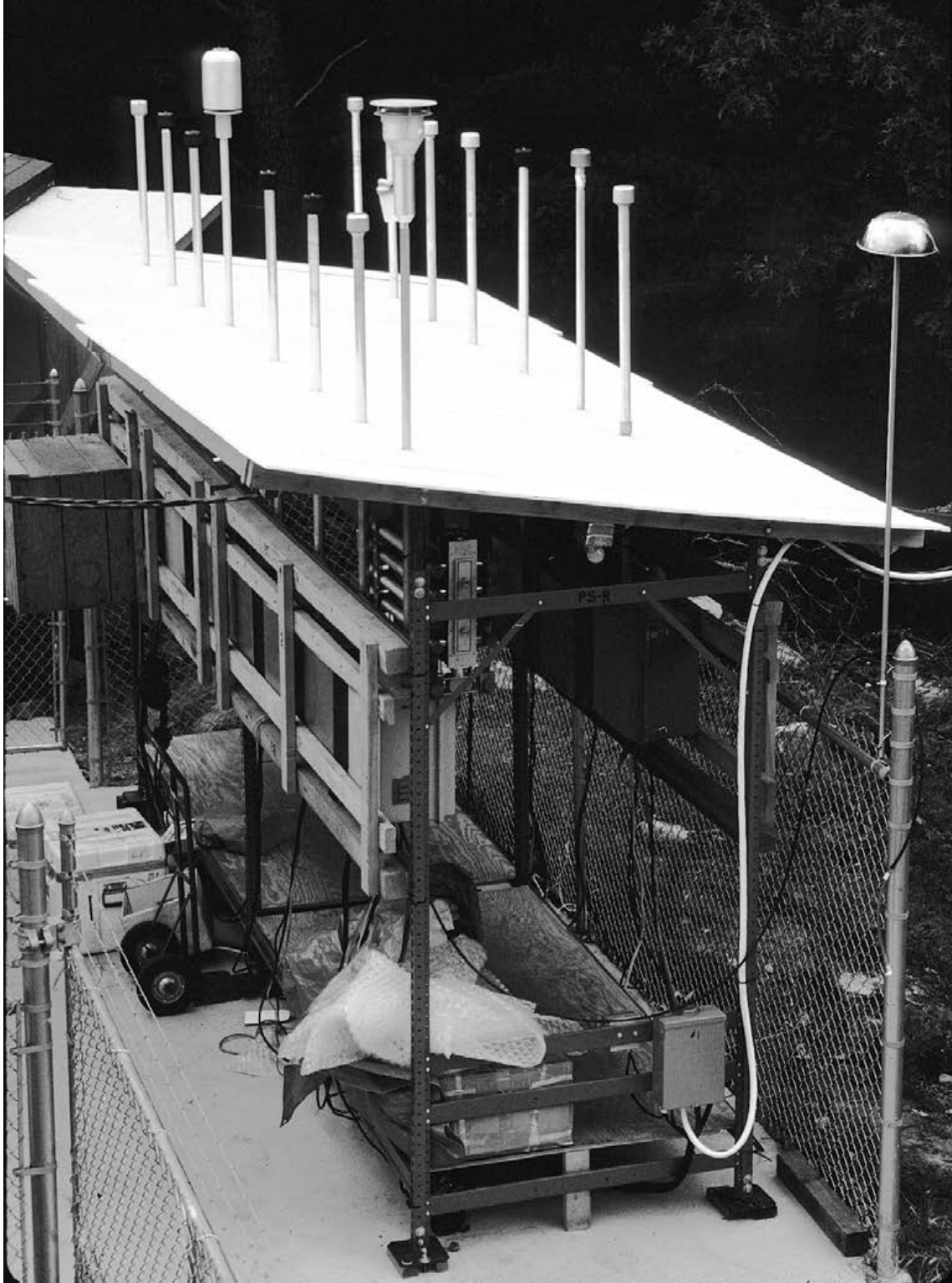


Figure 2.2 IMPROVE sampler stand showing location of samplers and sampler inlets through the stand's roof.



Figure 2.3 Nephelometer stand showing placement of nephelometers.

Campbell 21X data loggers were used to collect and store data using two-minute averages. Data was relayed from the Campbell 21X data logger to a central computer located in the NPS trailer.

2.1.1 Meteorological Instrumentation

Table 2.1 gives an overview of the instrumentation, manufacturer and model number, parameter measured, and the instrument manufacturer's reported uncertainty in the measurement parameter for the meteorological measurements made during SEAVS.

2.1.2 Meteorological Instrument Location and Operation

Three Rotronics mp 100f combination relative humidity/temperature sensors were mounted on the west facing side of the stand that housed the Optec nephelometers. These sensors were housed in PVC holders and aspirated by a fan. The flow rate through the holder was approximately 120 liters per minute. The sensors were approximately six feet above ground level and six feet from each other. The sampler stand housing these sensors had a plywood roof to shelter the sensors from direct sunlight and precipitation. There was also a heavy screen mesh on the west side of the

Table 2.1 Meteorological instrumentation overview.

Parameter Measured (units)	Method	Manufacturer and Model #	Manufacturer's Reported Uncertainty
Temperature (°C)	platinum RTD	Rotronics mp 100f	± 0.5 °C
Relative Humidity (%)	solid state capacitive polymer	Rotronics mp 100f	± 2%
Wind Speed (mph)	3 cup anemometer	Met One 014A	± 1.5% threshold of 0.45 m sec ⁻¹
Wind Direction (degrees)	wind vane	Met One 024A	± 5° threshold of 0.45 m sec ⁻¹
Solar Irradiance (kw m ⁻²)	solid state pyranometer	Li-Cor li200s	± 5%
Barometric Pressure (mbar)	variable capacitance barometer	Setra SBP 270	± 0.2 mbar

shelter to reduce the amount of direct late afternoon sunlight incident upon the sensors. The open sides of the shelter and sunscreen, however, allowed free ventilation of air through the shelter. There was a fourth temperature and relative humidity (RH) sensor housed in an aspirated PVC holder operated on top of the NPS trailer. This sensor had no protection from precipitation or direct sunlight other than the PVC holder. The wind speed, wind direction, and solar radiance sensors were mounted on a 10 m tower located at the northwest corner of the fenced compound. The barometric pressure sensor was mounted on the north side of the NPS trailer.

2.2 OPTICAL MEASUREMENTS OVERVIEW

During SEAVS, several key parameters related to the ambient aerosol were monitored on a continuous or semi-continuous basis using various optical instrumentation. The ambient light scattering coefficient (b_{scat}) was monitored continuously using one standard and four modified Optec NGN-2 integrating nephelometers. The ambient light extinction coefficient (b_{ext}) was monitored semi-continuously using an Optec LPV-2 transmissometer. Aerosol light scattering and aerosol size distributions were measured as a function of RH using: (1) an inlet designed to vary the RH of the sample aerosol, (2) a Radiance Research M903 nephelometer, and (3) a Particle Measuring Systems ASASP-X probe. The concentration of cloud condensation nuclei (CCN) was also monitored continuously using a TSI model 3010 optical particle counter.

2.2.1 Optical Instrumentation

Table 2.2 gives an overview of the optical instruments operated during SEAVS and the parameter being measured by the instrument.

Table 2.2 Optical instrumentation overview.

Parameter Measured	Instrumentation	Manufacturer Model #
scattering coefficient (b_{scat})	<ul style="list-style-type: none"> •ambient nephelometer •2.5 μm size cut nephelometer 	<ul style="list-style-type: none"> •Optec NGN-2 •modified Optec NGN-2
extinction coefficient (b_{ext})	transmissometer	Optec LPV-2
scattering as a function of RH	nephelometer/variable RH inlet	Radiance Research M903
size distribution as a function of RH	ASASP-X probe/variable RH inlet	PMS ASASP-X
condensation nuclei counter	optical particle counter	TSI-3010

2.2.2 Integrating Nephelometers

Nephelometers measure the scattering coefficient (b_{scat}) of the aerosol passing through an optical chamber. An ideal integrating nephelometer collects light scattered by ambient aerosols and gases from 0 to 180° over a defined band of visible wavelengths and would thus yield a direct measure of ambient aerosol scattering. Historically, however, integrating nephelometers have underestimated ambient scattering because of: (1) heating the aerosol, (2) ill-defined size cut of aerosol particles caused by inlet, sample train, and optical chamber, (3) large truncation angle, and (4) electronics that cause large nonlinear drifts in calibrations when operated at ambient temperatures, which can change significantly in time [Watson *et al.*, 1988, 1990; Molenaar, 1992].

The Optec integrating nephelometer was developed to minimize the limitations of integrating nephelometry described above. This instrument utilizes a unique open-air design that allows high aerosol flow rates (≈ 240 lpm) and thereby a short aerosol residence time in the nephelometer's optical chamber. The high flow rate and short residence time enhances accurate measurement of the ambient scattering coefficient (b_{scat}) by minimizing the heating of the aerosol sample in the nephelometer's optical chamber. Heating the ambient aerosol causes a reduction in measured light scattering by reducing the relative humidity of the sample aerosol and thereby reducing the liquid water content of particles. A reduction in the water content of a particle will reduce the size of the particle, which in general, will reduce the amount of light scattered by the particle. This problem is particularly acute under high (>70%) RH conditions and for aerosols that are hygroscopic. Heating may also cause the loss of volatile species other than water from the particle phase; this also could cause a reduction in the measured scattering coefficient. This instrument employs solid-state electronics to minimize drift caused by temperature variations and the open-air design reduces particle losses from impaction.

Five Optec NGN-2 integrating nephelometers, in various configurations, were operated during SEAVS. All these nephelometers were mounted on a covered instrument stand located inside the fenced compound as shown in Figure 2.1 and Figure 2.3. One of the five Optec nephelometers utilized the open-air configuration and was operated using standard IMPROVE protocols [ARS, 1995]. The other four Optec nephelometers were operated at reduced flow rates ($\approx 113 \text{ l min}^{-1}$) and were fitted with an inlet, to which a Bendix-240 cyclone could be attached. Two of these nephelometers were operated with an inlet and a cyclone. The other two nephelometers were operated with the inlet but without the cyclone. The four nephelometers that were operated with the inlet and at a reduced flow rate were much more susceptible to heating the sample aerosol in the optical chamber than was the open-air nephelometer. These nephelometers were therefore configured with a water jacket mounted on the back wall of the scattering chamber. This water jacket surrounded the light source where most of the heat in the system is generated. Water was circulated through the water jacket inside the nephelometer, then through a heat exchanger outside the nephelometer that was kept near ambient temperature by a large fan. Thermistors were placed inside the inlet, where sample air was assumed to be at ambient temperature, and at the sample air's exit from the scattering chamber, where sample air should be hottest if heating of the aerosol had occurred. Monitoring the difference in sample temperature between the inlet and the outlet of each nephelometer allowed us to determine if heating of the sample had occurred and if there was a subsequent change in sample RH. Figure 2.4 shows a schematic diagram of the modified Optec nephelometers.

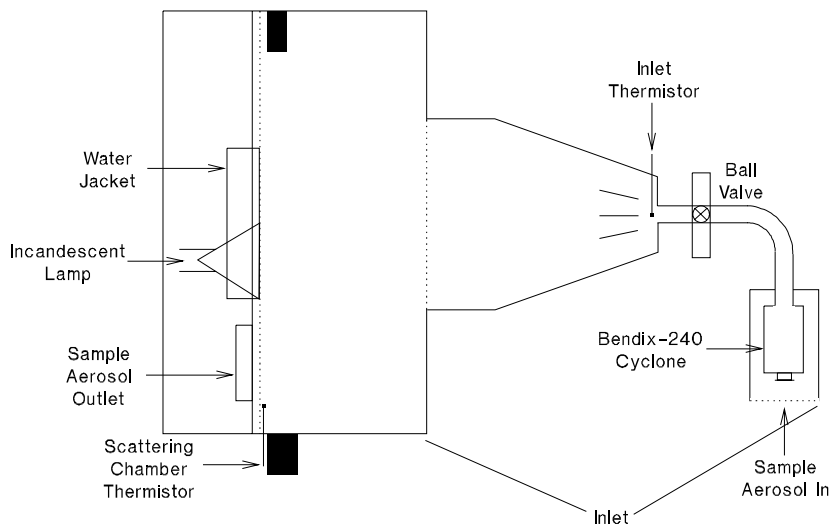


Figure 2.4 Schematic diagram of modified Optec NGN-2 nephelometer showing placement of thermistors, inlet with cyclone, and water jacket to cool area around lamp.

2.2.3 Transmissometer

An Optec Inc. LPV-2 transmissometer was used during the study to monitor the ambient light extinction coefficient (b_{ext}). It was operated over a path length of 0.8121 km. This transmissometer measures the irradiance, at 550 nm, of a light source after the light has traveled over a finite atmospheric path. The transmittance of the path is calculated by dividing the measured irradiance at the end of the path by the calibrated initial intensity of the light source. The transmission calculation is determined from an absolute (as opposed to relative) measurement of irradiance of a light source of known intensity. The average extinction of the path is calculated using Bouger's law from the transmittance and the path length. The measurement is ambient in that the sample is not drawn through an enclosed chamber; however, the measurement is made through optics that are exposed to the ambient atmosphere. The optics are cleaned regularly and are assumed to be free of dust and films, which tend to build up on optical surfaces. The light extinction measurements made by transmissometers are affected by meteorological interferences that are present along the site path (i.e., rain or fog).

The transmissometer's transmitter was located above a road cut; the receiver was located in the Lookout observation tower. Batteries that were recharged using solar cells powered the transmitter. There was an approximate difference in elevation between the transmitter and receiver of 300 feet. Transmissometer data was collected via radio modem by the central computer in the NPS trailer and by a Campbell 21X data logger. Figures 2.5, 2.6, and 2.7 show the layout of the transmissometer on a topographic map, the tower in which the receiver was located, and the site path of the transmissometer, respectively

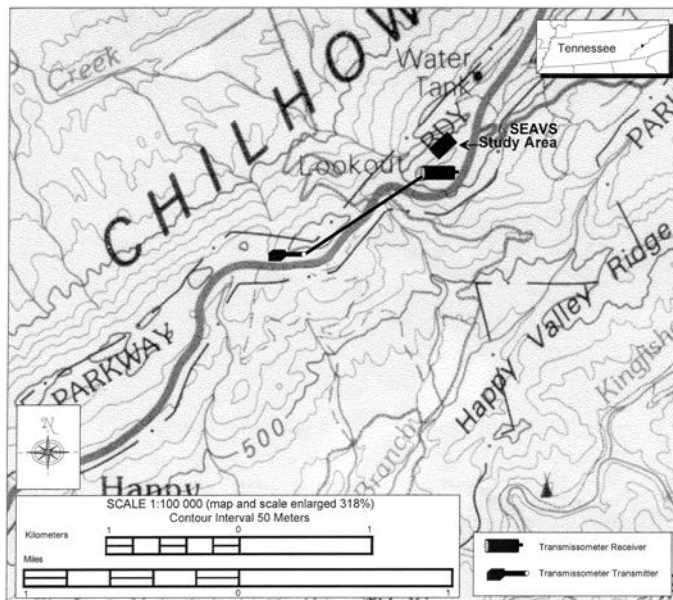


Figure 2.5 Topographical map showing the location of the transmissometer.



Figure 2.6 Observation tower that housed the receiver.



Figure 2.7 Transmissometer receiver and site path.

2.2.4 Aerosol Light Scattering and Size Distribution as a Function of RH

In this experiment, the change in aerosol light scattering coefficient and the change in aerosol size distribution were measured as a function of relative humidity. The goal of this experiment was to examine the hygroscopic nature of the ambient aerosol. To achieve this goal, an inlet was constructed that allowed the sample aerosol's relative humidity to be varied from <10% RH to >90% RH. Using this inlet, the aerosol light scattering coefficient was measured as a function of RH by a Radiance Research M903 nephelometer and the aerosol size distribution was simultaneously measured as a function of RH using a Particle Measuring Systems ASASP-X.

2.2.4.1 RH Control Inlet

The integral features of this inlet include: (1) a cyclone with 2.5 μm cut point, (2) Perma Pure Nafion drying tubes, (3) manual or automated control of sample RH, (4) a water bath to maintain nearly constant temperature of the sample aerosol, and (5) real-time monitoring of temperature and RH so that a given RH could be maintained throughout a sampling run. Each aspect of this inlet is described in detail below.

At the front end of this inlet, a protective cover was used to eliminate rain or insects from entering the sample train. After the sample passed through the cover it entered a cyclone with an approximate cut point of 2.5 μm . This cyclone has a d_{50} of 2.5 μm when operated at 21.7 liters per minute (1 min^{-1}). The total flow through the inlet was therefore maintained near 22 l min^{-1} required for the cyclone to give an aerosol cut point near 2.5 μm . To obtain a total flow rate of 22 l min^{-1} through the cyclone, 23 Perma Pure drying tubes, in parallel, were used. Each Perma Pure Nafion drying tube had an approximate sample flow rate of 1 l min^{-1} . The flow through each drying tube was not measured but is inferred from the total sample flow through the system, which was monitored using a rotameter after the aerosol sample passed through the nephelometer. The sample required by the ASASP-X was less than 1 l min^{-1} , therefore, most of the sample passing through the inlet went to the nephelometer and was subsequently measured by the rotameter.

The RH of the sample aerosol was controlled using Perma Pure Nafion drying tubes; a schematic diagram is shown in Figure 2.8. These dryers consist of an inner tube of Nafion through which the aerosol sample flows at approximately 1 l min^{-1} and an outer tube of stainless steel through which purge air flows at approximately 2 l min^{-1} . The flow of purge air was directed opposite to the flow of sample air. The driving force behind water movement across the Nafion tubing wall is the difference in water vapor pressure on either side of the wall. Therefore, the RH of the sample air could be decreased as well as increased by controlling the RH of the purge air used.

The RH of purge air was controlled by splitting a stream of pressurized ($\approx 20 \text{ psi}$), dried (<1% RH), and particle free air into two streams and sending each stream to a mass flow controller. The purge air from one mass flow controller was passed into a humidifier, while the air stream from the other mass flow controller remained dry. Purge air output from the mass flow controllers were regulated by varying the voltage input to the mass flow controllers. Voltage input could be controlled manually using a potentiometer or automated using voltage output from a Campbell 21X data logger. By appropriately mixing the humidified and dried purge air streams, any desired sample RH between $\approx 10\%$ and $\approx 90\%$ could readily be achieved.

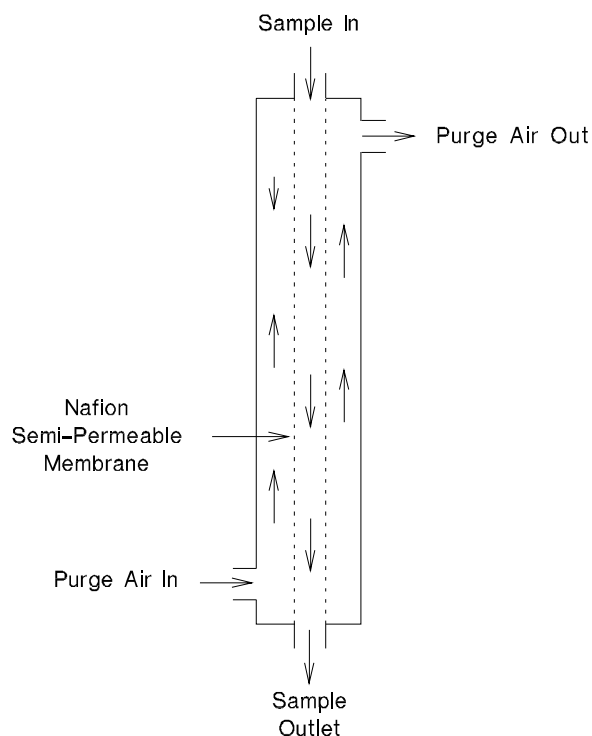


Figure 2.8 Schematic diagram of Perma Pure Nafion drying tube.

A circular array of 23 Perma Pure dryers were mounted in an insulated aluminum cylinder that was filled with water as shown in Figure 2.9. The water bath temperature varied by less than 4°C per day and thus the sample aerosol entering the plenum had only small variations in temperature throughout the day. The small variations in temperature of the sample at the plenum made it easier to keep the instrument enclosure at the same temperature as the plenum. This was necessary to keep the RH of the sample aerosol constant, while passing from the plenum to the instruments. Sample temperature and RH were monitored in the plenum and at the outlets of the Radiance Research nephelometer and PMS ASASP-X.

2.2.4.2 Radiance Research Nephelometer

A Radiance Research nephelometer was used in this experiment to measure the light scattering as a function of RH because of the relatively low flow rate required by the instrument and its small aerosol volume. The instrument was essentially unaltered from its factory configuration except that all air leaks were sealed, the system pressure checked, and the installed fan was replaced with a vacuum pump. Analog signal data was recorded using a Campbell 21X data logger on two-minute averages and serial data was logged by the instrument using five-minute averages.

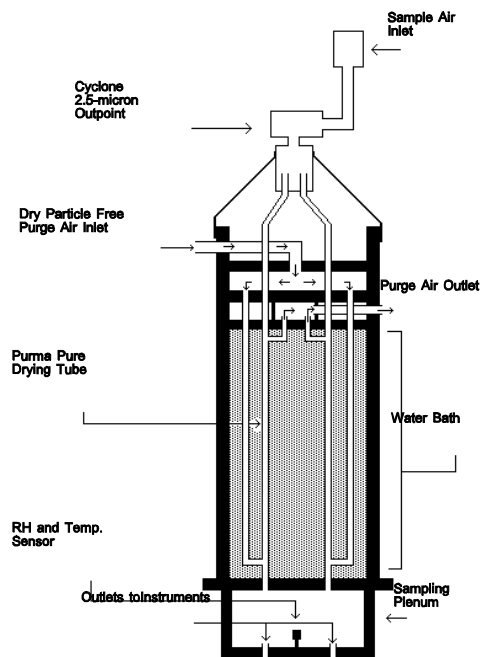


Figure 2.9 *Schematic diagram of variable RH constant temperature inlet. Only two Perma Pure Nafion drying tubes are shown, however, there were 23 tubes placed in a circular array in the actual inlet.*

2.2.4.3 Particle Measuring System ASASP-X

Aerosol size distributions were measured as a function of RH using a PMS ASASP-X optical particle counter. This instrument uses a flow of sheath air to hydrodynamically focus a flow of sample air through the instrument's optical chamber. The ratio of sheath air to sample air is about 20:1, therefore, to keep the RH of the sample constant for a given sampling period, air from the plenum was used as both sample and as sheath air. The sheath air, however, passed through a Teflon filter to remove particles before use in focusing the sample through the system's optics. The RH of the sample aerosol was continuously monitored at the exit of the instrument's optical chamber.

2.2.5 Condensation Nuclei Counter

The concentration of ambient condensation nuclei (particles > 0.015 μm) was continuously monitored during SEAVS using a TSI 3010 optical particle counter [TSI, Inc., 1992].

2.3 AEROSOL SAMPLERS

Bulk aerosol samples were collected for chemical analysis using the IMPROVE (Interagency Monitoring of Protected Visual Environments) sampler. Size-resolved aerosol samples were also

collected using an impactor (UCD DRUM sampler). The sampler configuration, field operation, and analysis of samples are briefly explained.

2.3.1 IMPROVE Sampler

The IMPROVE sampler was designed for the IMPROVE/NPS network and has been operated extensively in the network and during field studies since 1988. The IMPROVE sampler, shown in Figure 2.10, is a cyclone based modular unit designed for the collection of atmospheric particles. Ambient air enters via an inlet designed to eliminate rain, insects, and particles larger than about 15 μm . The sample then passes through an aluminum tube (approximately 8 ft long for the modules operated during SEAVS) and into a cyclone that provides 50% collection efficiency for 2.5 μm particles at a flow rate of 21.7 l min^{-1} . The sample air stream then passes through a filter, which collects particles, then to a critical orifice that regulates the sample flow rate. A vacuum pump at the end of the assembly produces the sample flow.

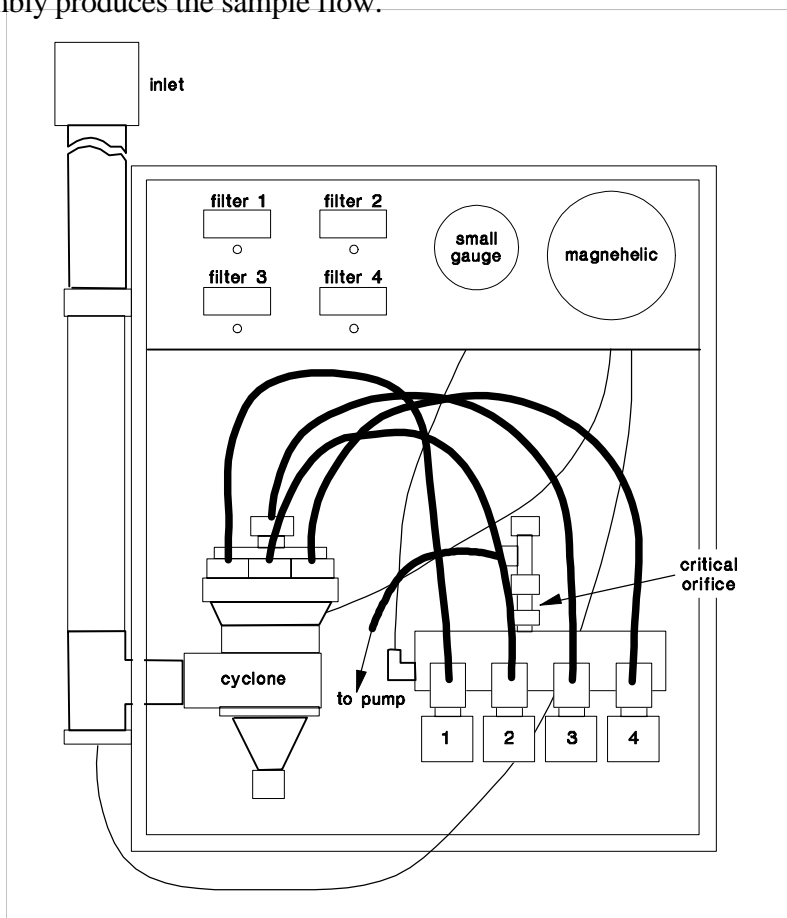


Figure 2.10 IMPROVE sampler.

The IMPROVE sampler consists of four independent modules. Each module incorporates a separate inlet array, filter pack, and pump assembly; however, all modules are controlled by the

same singular timing mechanism. It is convenient to consider a particular module, its associated filter, and the parameters measured from the filter as a channel of measurement (i.e., Channel A). With this designation, each channel as operated during SEAVS, is described below and summarized in Table 2.3.

The Channel A module was equipped with a cyclone. It utilizes a filter pack (cassette) with two tandem filters. The sample aerosol flows through each filter sequentially; the primary filter is Teflon, which collects particles, the second is a citric acid impregnated filter to trap ammonia gas. The primary Teflon filter is analyzed for: (1) fine mass ($PM_{2.5}$) gravimetrically, (2) nearly all elements with atomic mass number >11 (which is Na) and <82 (which is Pb) by proton induced x-ray emission (PIXE) and by x-ray florescent (XRF), (3) elemental hydrogen by proton elastic scattering analysis (PESA), and for light absorption by the laser integrating plate method (LIPM).

The Channel B module is also equipped with a cyclone. It utilizes a single Nylasorb filter to collect fine particles. The material collected from the filter is extracted ultrasonically in an aqueous solution that is subsequently analyzed by ion chromatography for the anions: sulfate, nitrate, nitrite, and chloride. The ammonium ion concentration was also measured, using extracts from these filters, however, in a separate colorimetric analysis.

The Channel C module is equipped with a cyclone and utilizes tandem quartz fiber filters for the collection of fine particles, and to estimate the organic carbon artifact from organic gases collected on the secondary filter. These filters are analyzed by thermal optical reflectance (TOR) for elemental and organic carbon. Because there are several similar techniques or procedures for carbon analysis, the following is a detailed description of the analytical process used for determining the carbon data reported here.

The TOR process involves subjecting a 0.5 cm^2 punch from the quartz fiber filter to a series of temperature increases. The organic carbon is volatilized at 120, 250, 450, and 550°C in a pure He atmosphere, followed by combustion of elemental carbon in a 2% $\text{O}_2/98\%$ He atmosphere at temperatures of 550, 700, and 800°C . The carbon compounds volatilized at each step are converted to CO_2 by passing them through an oxidizer (MnO_2 at 212°C). The CO_2 is then reduced using a methanator (firebrick impregnated with nickel catalyst at about 550°C in a stream of hydrogen), and finally detection of CH_4 equivalents is accomplished with a flame ionization detector (FID). Throughout the analysis cycle a He-Ne laser with a photodetector monitors sample reflectance. During the intermediate heating steps (from 250 to 550°C under He atmosphere) some nonvolatile organic carbon is pyrolyzed to elemental carbon (light-absorbing carbon), thus the measured reflectance decreases. Reflectance, however, increases rapidly when oxygen is added and the light-absorbing carbon is combusted and removed from the filter. When the reflectance returns to its initial value, the amount of carbon, which evolved since the introduction of O_2 , is considered to be pyrolyzed carbon and is assigned to the organic component. Figure 2.11 shows a typical time development of the TOR process.

Channel D module utilizes a filter pack (cassette) with two tandem filters. The first filter is a Teflon filter, which is gravimetrically analyzed for mass (PM_{10}). The second filter is a sodium carbonate impregnated Teflon filter, which collects SO_2 gas.

Two filter samples were collected each day and each filter collected sample aerosol for a 12-hour time period. Sampling periods were from 7:00 a.m. through 7:00 p.m. EST and from 7:00 p.m. through 7:00 a.m. EST. Two filter cassettes were loaded each evening around 7:00 p.m. and the sampler was started. At 7:00 a.m. the next morning, the sampler automatically switched and started sampling from the second filter cassette. Exposed cassettes from Channels A, B, and D were stored in sealed plastic bags and shipped to UCD for storage and analysis, while exposed sample cassettes from Channel C were stored in a freezer for the duration of the study. The Channel C carbon filters were packed in a cooler and shipped on ice to UCD.

Table 2.3 Summary of IMPROVE modules used during SEAVS.

Channel	Filter 1/Filter 2	Parameter Measured/Analytical Technique
A	Teflon/citric acid impregnated Teflon	mass (PM _{2.5})/gravimetric, Na-Pb/(PIXE and XRF), total H/PESA, NH ₃ gas from Filter 2
B	Nylasorb	anions (SO ₄ ²⁻ , NO ₃ ⁻ ,...)/IC
C	Quartz/Quartz	Carbon/TOR
D	Teflon/Sodium carbonate impregnated Teflon	mass (PM ₁₀)/gravimetric SO ₂ gas from Filter 2

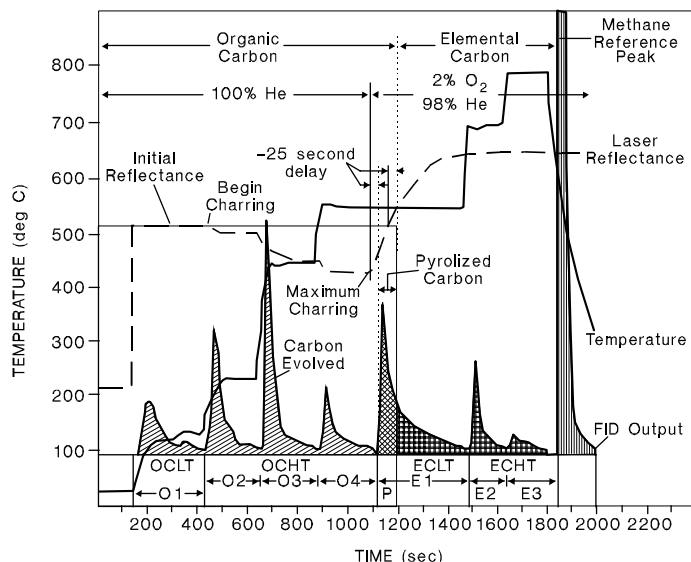


Figure 2.11 Time development of the TOR carbon analysis.

2.3.2 Davis Rotating-Drum Universal-Size Cut Monitoring (DRUM) Sampler

The size segregating DRUM sampler is an eight-stage cascade impactor. Particles are collected on grease-coated Mylar strips that cover the outside circular surface of a slowly rotating cylinder. Particles are accelerated through a jet and the surface of the cylinder is placed an appropriate distance from the jet to produce impaction of particles over a given size range. The size cuts for the eight stages are 10.00, 5.00, 2.50, 1.20, 0.56, 0.34, 0.24, and 0.07 μm . A backup filter located at the outlet of the last stage is employed to collect particles smaller than 0.07 μm or to collect particles that have “bounced” off the Mylar strips. The last five stages (2.5 μm and below) were analyzed for chemical composition using PIXE.

2.4 REFERENCES

Air Resource Specialists, Inc., Standard operating procedure and technical instructions for nephelometer systems, 4200-2000, 4100-3100, 1995.

Instruction Manual Model 3010 Condensation Particle Counter, copyright 1992, published by TSI Incorporated, St. Paul, MN, 1992.

Molenaar, J.V., D.S. Cismoski, and R.M. Tree, Intercomparison of Ambient Optical Monitoring Techniques, in Proceedings of the Air & Waste Management Association Annual Meeting, 92-60.09, Kansas City, MO, 1992.

Watson, J.G., J.C. Chow, L.C. Pritchett, W.R. Pierson, C.A. Frazier, R.G. Purcell, and I. Olmez, The 1987-88 metro Denver brown cloud study, Desert Research Institute, Doc 8810 1F2, Desert Research Institute, Reno, NV, 1988.

Watson, J.G., J.C. Chow, L.W. Richards, D.L. Haase, C. McDade, D.L. Dietrich, D. Moon, L. Chinkin, and C. Sloane, The 1989-90 Phoenix urban haze study, Volume I: program plan. DRI document 8931.3F, prepared for Arizona Department of Environmental Quality, Phoenix, AZ, by Desert Research Institute, Reno, NV, 1990.

CHAPTER 3

CALIBRATIONS, UNCERTAINTIES, AND QUALITY ASSURANCE PROCEDURES

This chapter presents the instrument and sampler calibration schemes, a discussion of measurement uncertainty, and the quality control/quality assurance (QA/QC) procedures implemented by the NPS group of researchers during SEAVS. An important aspect of the QA/QC for the study was redundancy of measurements wherever it was economically feasible and practical to do so, therefore, comparisons between the redundant measurements are shown in this section. Comparisons between redundant measurements can give estimates of measurement precision, accuracy, and an insight into the general quality of the data. However, before discussing the calibrations, uncertainties, and QA/QC procedures, the importance of sample relative humidity (RH) and temperature are discussed to give the reader an estimate of how the uncertainty in these parameters relates to comparisons made between the measurements and the model calculations, which are presented in later sections of this report.

3.1 DEPENDENCE OF MEASUREMENTS ON SAMPLE RH AND TEMPERATURE

Some important objectives of SEAVS were: (1) to determine the hygroscopicity (water uptake) of the ambient aerosol as a function of relative humidity (RH), (2) to relate the measured aerosol growth from water uptake to the aerosol growth predicted from model calculations, and (3) to integrate measurements of aerosol mass, size distribution, and ambient relative humidity to reconstruct both the measured scattering and extinction coefficients. The water uptake of the aerosol was measured as a function of RH using: (1) an optical particle counter that measured the change in particle size distribution and (2) a nephelometer that measured the change in light scattering coefficient. Both data sets (aerosol size distributions as a function of RH and aerosol light scattering coefficient as a function of RH) can be compared to theoretical model calculations. Theoretical calculations can also be applied to the measurements of aerosol bulk chemical composition and mass size distributions to reconstruct the “ambient” scattering or extinction coefficients. All of these comparisons, however, require accurate measurement of the aerosol sample’s relative humidity during the measurement. For instance, the RH of the aerosol sample in the nephelometer’s scattering chamber is the RH of importance for the calculations mentioned above as opposed to the ambient RH, which could be significantly different.

The RH of an aerosol sample will depend strongly on changes in the temperature, as shown in Figure 3.1. Given an initial relative humidity for an aerosol sample (abscissa in Figure 3.1) and an increase in temperature (ΔT), the subsequent reduction in sample RH is shown on the ordinate.

These calculations demonstrate that a small increase in temperature, $\Delta T = 0.5^\circ\text{C}$, for an aerosol sample initially at 50% RH and 25°C , would result in a decrease in RH to about 48.5%. However, at an initial RH of 95% the aerosol sample's RH would decrease to about 92.5% for the same ΔT increase. An aerosol sample initially at 50% RH and at 25°C that underwent an increase in temperature of 4°C would have a final RH of about 40%, whereas if the sample were initially at 95% RH and underwent the same 4°C increase in temperature the final RH of the sample would be about 76%.

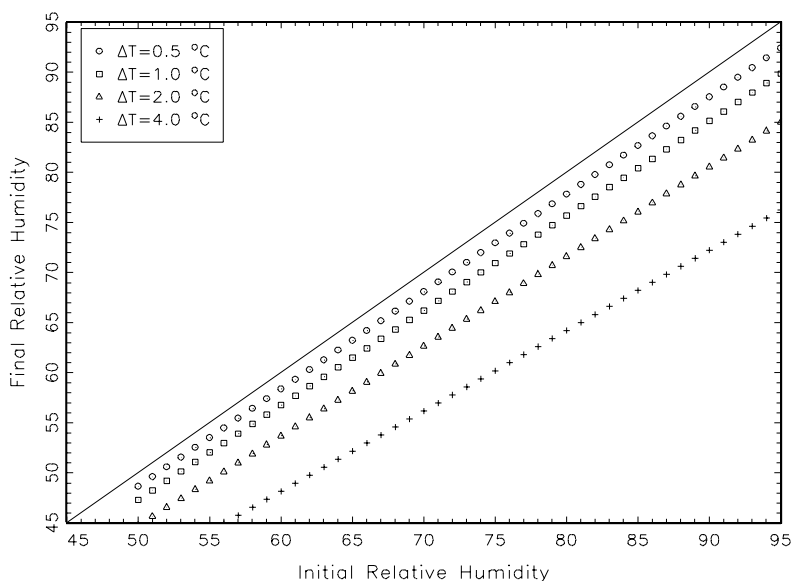


Figure 3.1 Plot showing the initial RH and the final RH given an initial temperature of 25°C and a change in temperature, ΔT .

The influence a small change in sample temperature has on sample RH is graphically demonstrated in Figure 3.1. These changes in sample temperature and the subsequent changes in sample RH will have a significant impact upon any measurement that depends upon the sample's relative humidity. To demonstrate this, Figure 3.2 shows the percent change in aerosol scattering coefficient (b_{scat}) for a given change in sample temperature and an initial sample relative humidity. This plot was generated using data obtained from a nephelometer, which measured the aerosol light scattering coefficient as a function of RH during SEAVS. The final data from this nephelometer was in the form of a ratio ($b_{scat}(\text{RH})/b_{scat}(\text{RHD})$), where $b_{scat}(\text{RH})$ is the scattering coefficient at a measured RH value and $b_{scat}(\text{RHD})$ is the scattering coefficient of the "dry" ($<15\%$ RH) aerosol. By fitting all data points to a curve, the average ratio over the entire study period as a function of RH was obtained. By calculating the ratio at an initial RH and then recalculating the ratio for the RH after a given temperature increase, the percent difference in scattering coefficient that would be expected for a given change in temperature was obtained. These calculations, shown in Figure 3.2, demonstrate that a 0.5°C increase in temperature for an aerosol initially at 50% RH will produce a 1% decrease in b_{scat} . However, if the aerosol were initially at 95% RH and underwent the same change in temperature the decrease in b_{scat} would be about 17%.

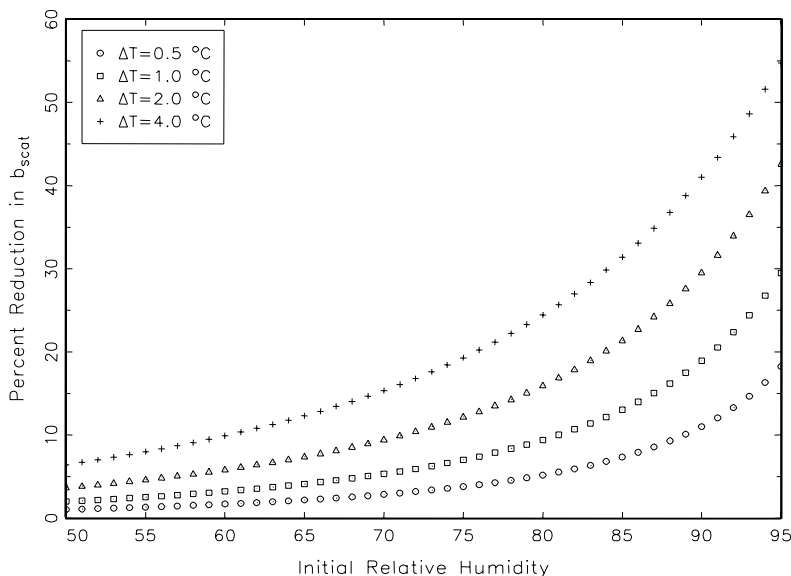


Figure 3.2 Plot showing the percent reduction in scattering coefficient, b_{scat} given an initial RH, temperature, and a change in temperature, ΔT . The increase in temperature reduces the sample's RH inside the nephelometer's scattering chamber thereby reducing the measured scattering coefficient.

Figures 3.1 and 3.2 graphically illustrate how changes in the temperature of an aerosol sample will affect the sample's relative humidity and hence the light scattering coefficient. This example demonstrates the magnitude of the light scattering coefficient's dependence on RH and demonstrates the need for accurate measurement of the ambient temperature and humidity as well as the sample aerosol's temperature so that any changes in RH can be compensated for when comparing field measurements to theoretical calculations. Although this example demonstrated the sensitivity of the light scattering coefficient, a change in aerosol temperature will have an impact on any measurement that depends upon RH.

3.2 METEOROLOGICAL INSTRUMENTS

The instruments used to collect meteorological data during SEAVS were set up and calibrated in accordance with IMPROVE protocol, except that the tower was closer to trees than is normally acceptable [Air Resource Specialists, Inc., 1995]. The manufacturers' reported uncertainties for each instrument are presented in Table 2.1. The meteorological measurements considered particularly crucial to SEAVS were ambient relative humidity (RH) and the RH of the aerosol during sampling. Therefore, the combined RH/temperature sensors used during SEAVS were tested for accuracy and precision by an independent auditor before and after the sensors were deployed in the field.

3.2.1 RH Sensor Comparison

Three RH/temperature sensors were mounted on the nephelometer stand inside the fenced compound near the inlets of the nephelometers (see Figure 2.3). The sensors were placed about six feet from each other at roughly the same height above the ground (± 1 foot). In this discussion, the sensors are referred to as sensors 1 through 3. Sensor 1 was mounted on the southern end of the nephelometer stand, while sensor 3 was approximately twelve feet away at the northern end of the stand. Figure 3.3 shows a scatter plot of RH measured by sensor 2 versus RH from sensor 1. This plot shows there is reasonably good agreement between these two sensors. About half of the data points (55%) are less than one RH unit different ($\pm 1\%$ RH), 91% of the data points are less than 2% different in RH, and nearly all the data (98%) are less than 3% different in RH. Summary statistics for all three sensors are shown in Table 3.1. The statistics show that there is fairly good agreement between the sensors on average. The average difference between sensors 1 and 3 is 1.24% RH, which is less than the manufacturer's reported uncertainty of $\pm 2\%$ RH.

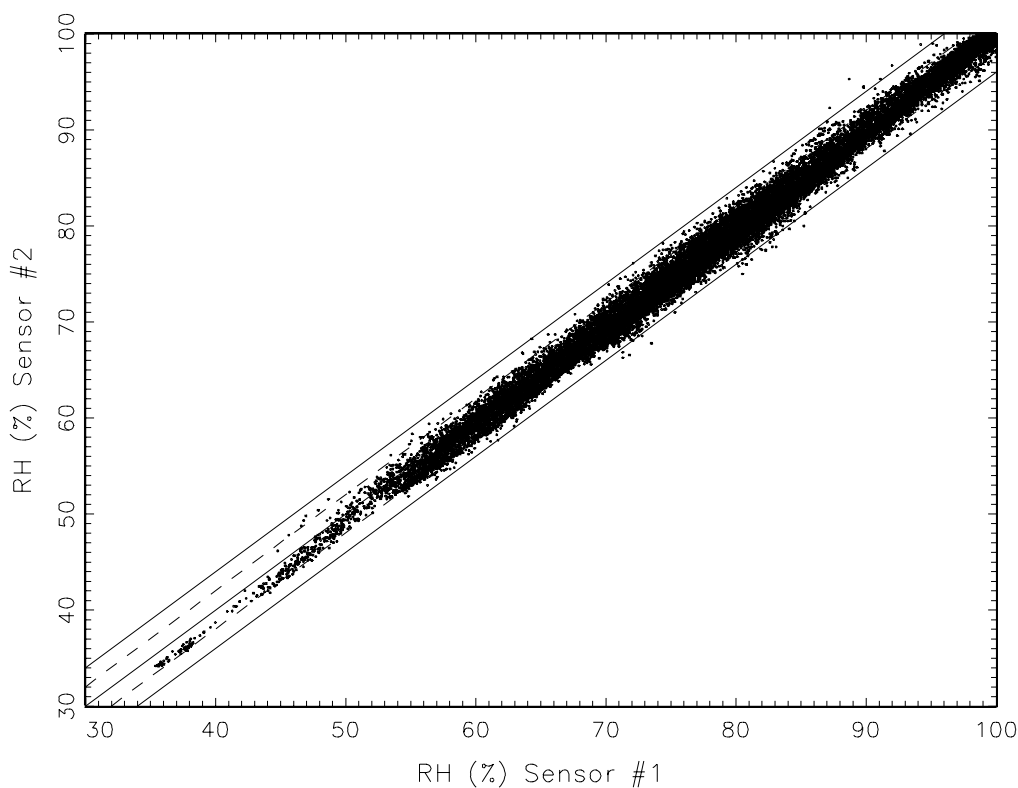


Figure 3.3 Scatter plot showing a comparison of RH sensor 1 with RH sensor 2. The dashed lines indicate ± 2 RH units ($\%RH$) and the solid lines indicate ± 4 RH units.

Table 3.1 Summary statistics of RH sensors.

Variable	Mean	Standard Deviation	Minimum	Maximum	Number of Observations
Sensor 1	77.46	12.37	35.39	102.8	22,171
Sensor 2	76.92	12.63	34.16	102.2	22,171
Sensor 3	76.22	12.59	35.26	100.1	22,171

To simultaneously compare all three sensors and to calculate the maximum difference between the sensors, the percent difference, as defined by Equation (3.1), was used:

$$\% \text{ Difference} = \frac{(\text{Max} - \text{Min})}{\text{Mean}} * 100\%, \quad (3.1)$$

where *Max*, *Min*, and *Mean* are the maximum value, minimum value, and average value, respectively, that were observed by any of the three sensors during a given measurement period. Figure 3.4 shows a histogram of the number frequency (the number of times each percent difference was observed) versus the percent difference calculated using Equation (3.1). The maximum difference between the three sensors ranges from 0 to about 6%. The average difference was 2.3%. Ninety two percent of the data points are less than 4% different and 98% of the data points are less than 5% different. Thus, 98% of the time the variability between sensors is less than 5%. If the mean of the three sensors is used as a measure of the “true” RH and the variability is used as an uncertainty, then at 77% RH, which was close to the mean humidity for the entire study period, the uncertainty would be 77% ± 3.8% RH.

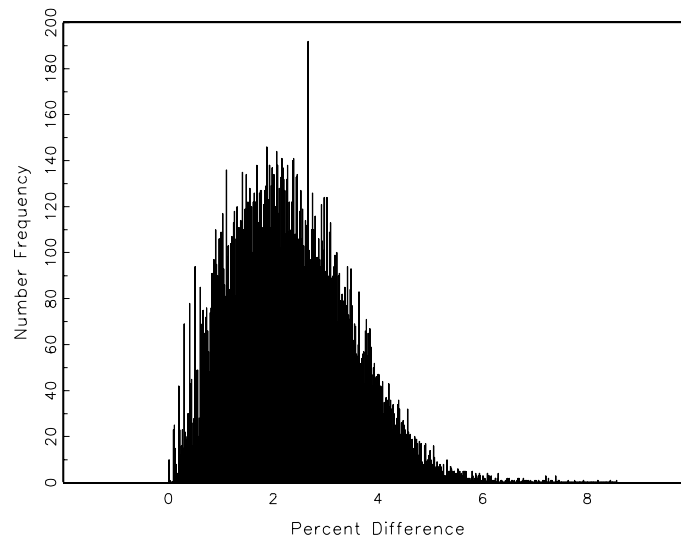


Figure 3.4 Histogram showing the maximum percent difference between all three RH sensors that were mounted on the nephelometer stand.

3.3 OPTICAL INSTRUMENTS

3.3.1 Optec NGN-2 Nephelometer Calibrations

There were five Optec nephelometers operated during SEAVS. Figure 2.3 and Figure 2.4 showed the nephelometer stand and the configuration of the instruments. Four of the nephelometers were modified as described in Chapter 2; the fifth nephelometer was operated as it came from the factory in “open air” configuration. In this section, the calibration of the nephelometers is discussed and the scattering coefficients, b_{scat} , obtained from nephelometers, which were configured similarly, are compared to estimate the uncertainty in the scattering coefficient. Throughout this discussion the nephelometers are referred to as neph 1 through neph 5 or N1 through N5. The labeling system depicts the order in which the nephelometers were mounted on the stand. Neph 1 was the nephelometer on the southern end of the stand and neph 5 was on the northern end of the stand. Neph 1 and neph 3 were operated with cyclones, which provided a 2.5 μm cut point for the sample aerosol; neph 2 and neph 4 were operated without cyclones.

The scattering coefficient (b_{scat}) for ambient air is obtained from nephelometry by calibrating the instrument using clean air as a zero calibration point and a span gas as an upscale calibration point. The span gas used during SEAVS was SUVA-134A, which is a commonly used refrigerant gas. Calibration of the nephelometer allows conversion of the nephelometer’s response (normalized counts) to aerosol scattering (b_{scat}) by the following two-step process.

1. A simple linear equation:

$$y = m x + b \quad (3.2)$$

where

- y = multiple of Rayleigh scattering,
- m = slope of calibration line,
- x = normalized nephelometer counts, and
- b = intercept (usually interpreted as wall scatter)

relates normalized nephelometer counts to multiples of Rayleigh scattering.

The slope, m , of the calibration line is given by:

$$m = \frac{S_{SUVA} - S_{CA}}{C_{SUVA} - C_{CA}}, \quad (3.3)$$

where

- S_{SUVA} = span gas multiple of Rayleigh Scattering (7.2),
- S_{CA} = clean air multiple of Rayleigh Scattering (1.0),
- C_{SUVA} = nephelometer’s normalized response for span gas,
- C_{CA} = nephelometer’s normalized response for clean air.

The intercept, b , is calculated using:

$$b = S_{CA} - m C_{CA}. \quad (3.4)$$

2. The scattering coefficient (b_{scat}) is then calculated by multiplying the output of Equation (3.2) by the Rayleigh scattering coefficient, which is estimated from the elevation of the site. A value of 0.010363 km^{-1} is used for calculating b_{scat} at the Great Smoky Mountains sampling site. The error resulting from not correcting for temperature and pressure variations in the value of the Rayleigh scattering coefficient has been determined to be on the order of $\pm 5\%$ [Malm *et al.*, 1994a].

During SEAVS, the Optec nephelometers were zeroed automatically using dry, particle free air three times each day. The automated clean air calibrations were done by circulating clean air through the nephelometer for thirty minutes at midnight, 8:00 a.m., and 6:00 p.m. The clean air calibration value, obtained from each calibration period, is an average of the last 20 minutes of the 30-minute calibration period. The average of the last 20 minutes of a calibration period was used because it took several minutes to purge the entire sample aerosol from the nephelometer's inlet and scattering chamber and for a stable signal to be achieved by the nephelometer during a calibration.

Span gas calibrations were done every four to seven days. The frequency of span gas calibrations depended upon how consistent the clean air calibrations had been over the previous few days. Whenever successive clean air calibration values (zeros) appeared to drift or change significantly, a span gas calibration was performed to determine the new slope of the calibration lines for the nephelometers. The span gas used most often was SUVA-134A, however, three additional calibrations were done using Freon-12 and Freon-22. Span gas calibrations were done manually and usually immediately after the automatic clean air calibration occurring at 6:00 p.m., however, some span gas calibrations were also performed after the midnight clean air calibration to ensure there was no significant bias in the slope of the calibration line due to temperature variations.

Figure 3.5 shows a time series plot of the automated clean air calibration values (zeros) versus time for neph 2. This nephelometer was operated with an inlet but without a cyclone during SEAVS (see Figure 2.4). The two lines on the plot represent: (1) all the automated clean air calibrations performed during SEAVS and (2) the daily averaged clean air calibrations. The time line shows this nephelometer's response to clean air varied from about 114 mV early in the study (Julian day 200) to about 121 mV at the end of the study (Julian day 237). The increase in the value of the clean air calibration over time is usually attributed to "wall scatter"; that is, aerosol particles deposit and accumulate on the walls of the scattering chamber during normal operation of the nephelometer, as they accumulate they scatter more light and therefore the background light scattering increases. The time line also shows there is a small variation in the clean air calibration values from one calibration period to the next. The standard deviations of the daily averaged clean air calibrations for this nephelometer ranged from 0.4 to 1.2.

The drift in the clean air calibration values (zeroes) with time, the variation in the zeroes from one calibration period to the next, and the variation in the span gas calibration values cause the slope and intercept of the calibration line to also vary and drift in time as shown in Figure 3.6.

These seven calibration lines represent the entire range of slopes and intercepts encountered during the study for neph 2. That is, the maximum and minimum values of both the slope and intercept are represented in this plot. The seven calibration lines, calculated from clean air and span gas calibrations, conducted between Julian day 197 and Julian day 230, show the amount of variation present in the calibration lines. Each span gas calibration was performed approximately six days apart. Since the slopes and the calibration lines varied in time, a linear interpolation was done from one calibration period to the next calibration period to calculate continuous calibration values. These calibration values were used to calculate a new calibration line for each nephelometer output (2-minute averaged data point).

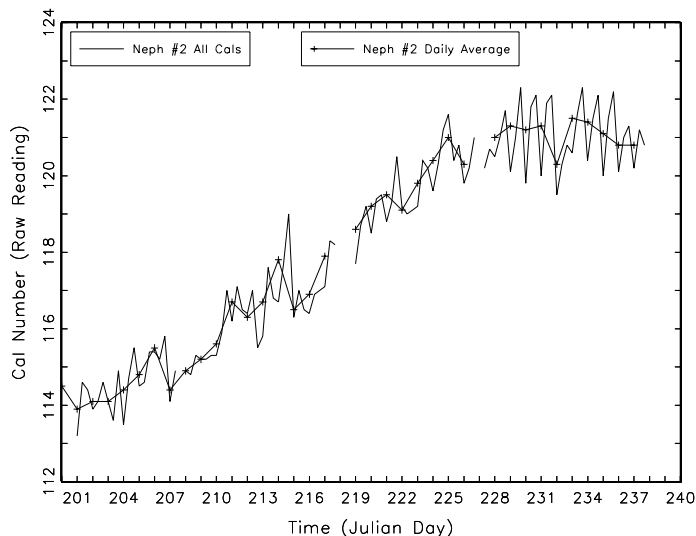


Figure 3.5 Time line showing the daily variation and the increase in clean air calibration values for neph 2 during SEAVS.

3.3.1.1 Comparison of Optec NGN-2 Nephelometers

The uncertainty associated with the calibration values (i.e., span and clean air calibrations) determines the uncertainty in the calibration line and therefore a large part of the uncertainty in the measured b_{scat} . The uncertainty for the Optec NGN-2 nephelometer has been reported in previous studies to be around 10% [Molenaar *et al.*, 1992]. In this analysis, nephelometers that were operated without cyclones (neph 2 and neph 4) are compared and nephelometers that were operated with cyclones (neph 1 and neph 3) are compared to estimate the uncertainty in b_{scat} between nephelometers, which are expected to give the same scattering coefficient. It should be noted that the comparisons here are made using 2-minute averaged b_{scat} data. This short averaging period inherently leads to more scatter in the data because the random fluctuations in the instrument response are smoothed somewhat when data are averaged over longer time periods. However, the 2-minute averaged data points are used because they allow the best resolution when comparing the instruments over short time intervals.

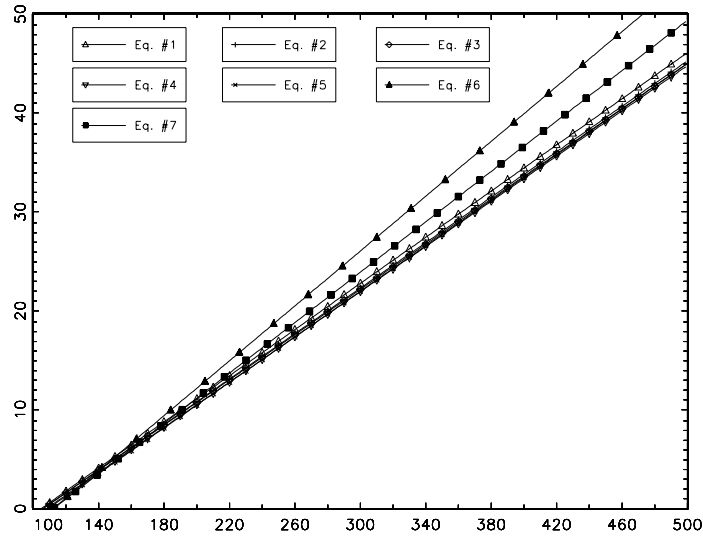


Figure 3.6 Plot showing the variation and change in time of the calibration lines for neph 2 during SEAVS. The equations are numbered in chronological order with Eq. #1 calculated from calibrations done on Julian day 197 and Eq. #7 calculated from calibrations done on Julian day 230.

Figure 3.7 shows a scatter plot of neph 4 versus neph 2 and the results of an ordinary least squares regression (OLS). The plot of measurements from nephelometers 2 and 4, which were both operated without cyclones, shows there is some scatter in the data. However, neph 4 gave moderately higher scattering coefficients quite consistently and was about 4% higher at the highest recorded b_{scat} values. The R^2 from the linear regression was 0.997, which shows the data fit the linear model exceptionally well, however, the high R^2 should be viewed with caution as the R^2 from OLS regression is generally high when the range of the variables is much greater than the differences between the variables as is the case with this data. The regression lines obtained by OLS regression analysis of data from nephs 2 and 4 and the results obtained by regression analysis of data from nephs 1 and 3 are given in Table 3.2.

Summary statistics are given below in Table 3.3. The mean values show there is good agreement between the nephelometers on average as there is just over two percent (2.1%) difference between neph 1 and neph 3, while there is slightly more than five percent difference (5.4%) between nephs 2 and 4. The number of observations for each comparison is different between the two pairs because both nephs 1 and 4 were inoperable for short but different time periods during the study.

The summary statistics and regression analyses show there is good agreement between the nephelometers on average. To determine the difference between two instruments, the percent difference, $(N4-N2)/[(N4+N2)/2]*100$, was calculated for each b_{scat} measurement. The results are shown using a histogram in Figure 3.8. The frequency (number of occurrences) is plotted on the

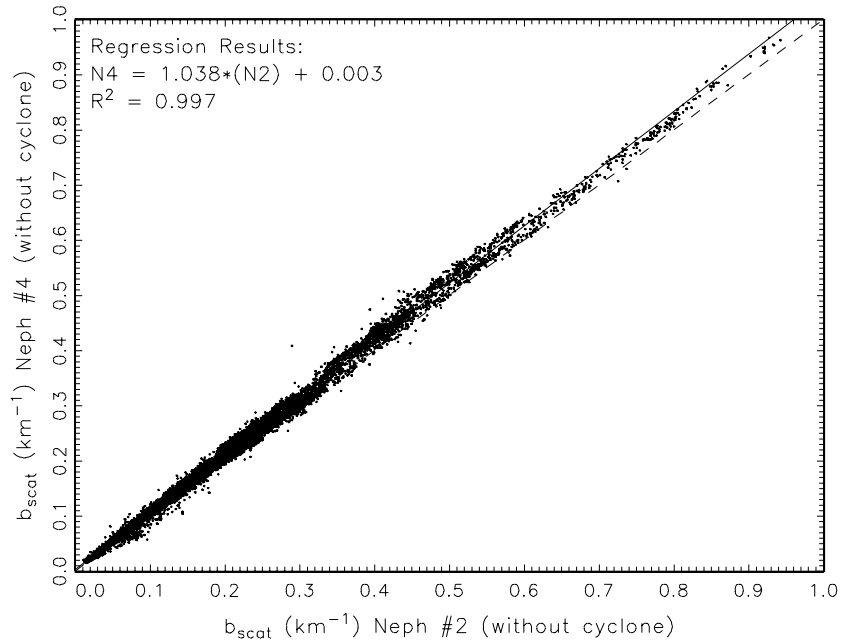


Figure 3.7 Scatter plot showing 1:1 line (dashed), regression line (solid), and results of OLS regression analysis for neph 2 and neph 4.

Table 3.2 Results of regression analysis.

Regression Line: Coefficient \pm Standard Error	R^2	Number of Observations
$N4 = (1.0382 \pm 0.0004)(N2) + (0.0029 \pm 0.0001)$	0.997	21,970
$N3 = (0.9712 \pm 0.0006)(N1) + (0.0085 \pm 0.0001)$	0.993	22,303

Table 3.3 Nephelometer summary statistics.

Nephelometer	Mean	Std. Dev.	Minimum	Maximum	# of Obs.
Neph 1 with cyclone	0.1702 (km^{-1})	0.1349	0.0108	0.9653	22,303
Neph 3 with cyclone	0.1738	0.1314	0.0181	0.9274	22,303
Neph 2 no cyclone	0.1451	0.1325	0.0109	0.9421	21,970
Neph 4 no cyclone	0.1535	0.1378	0.0151	0.9674	21,970

ordinate versus the percent difference on the abscissa. This plot shows the percent difference between neph 4 and neph 2 ranges from about -10% to about 20% . The mean value was 6.61% difference. Thirty three percent of the data points for nephs 2 and 4 are less than 5% different, 78% of the data points are less than 10% different, and 96% of the data points are less than 15% different. Table 3.4 summarizes the results of this type of an analysis for both the nephelometers with and without cyclones.

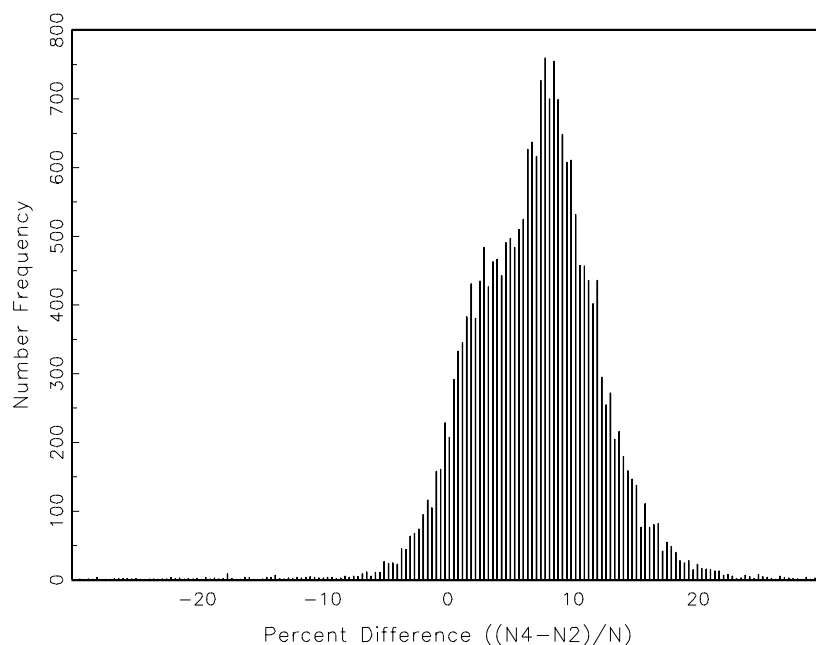


Figure 3.8 Histogram showing the distribution of percent differences between neph 4 and neph 2.

Table 3.4 Summary of percent differences.

Comparison Pair	Mean Percent Difference	% of Data Points < 5% Different	% of Data Points < 10% Different	% of Data Points < 15% Different
$(N4-N2)$ $(N4+N2)/2$ no cyclone	6.61%	33%	78%	96%
$(N3-N1)$ $(N3+N1)/2$ with cyclone	4.05%	50%	75%	90%

The total error in the b_{scat} measurement is composed of two components: (1) determinate error or systematic error and (2) indeterminate error or random error. The determinate error in this set of data most likely arises from imperfections in instrumentation (i.e., differences in electronic

components) or from personal errors in calculating the calibration lines. The causes of the random error are more difficult to identify and can arise from many sources. Although the sources of these errors are difficult to identify, the magnitude of each type of error can be estimated. Results of the OLS regression, given in Table 3.2, can be used to predict the b_{scat} value of one nephelometer from the value measured by another nephelometer. In Table 3.2, for instance, the regression line predicts a b_{scat} value for neph 4 from the measured b_{scat} value of neph 2. The slope of the regression line plus the additive term together comprises a measure of the “bias” between the two nephelometers. This “bias” can be interpreted as a systematic error because it represents, in general, a unidirectional difference between the two measurements of b_{scat} . Therefore, the regression analysis shows there is about a 4% systematic error between neph 2 and neph 4 and about a 3% systematic error between neph 3 and neph 1. The OLS regression is not the most rigorous approach for this type of analysis because this technique assumes all of the uncertainty is in the Y variable, however, for an estimation of systematic and random uncertainties this technique is sufficient.

The random error can be estimated by calculating a residual term, which is the difference between the b_{scat} value of neph 4 predicted from the regression line (N4p) and the value of b_{scat} actually measured (N4m). Figure 3.9 shows a histogram of the frequency of occurrence versus the residual (N4p-N4m). The residual is in units of km^{-1} and can be compared directly to the scattering coefficient. This plot shows that most data are within $\pm 0.02 \text{ km}^{-1}$. Taking the absolute value of the residual, the number of occurrences less than a particular value is shown in Table 3.5. For instance, this analysis shows that 66% of the residual data points are less than 0.005 km^{-1} different and about 85% are less than 0.01 km^{-1} different.

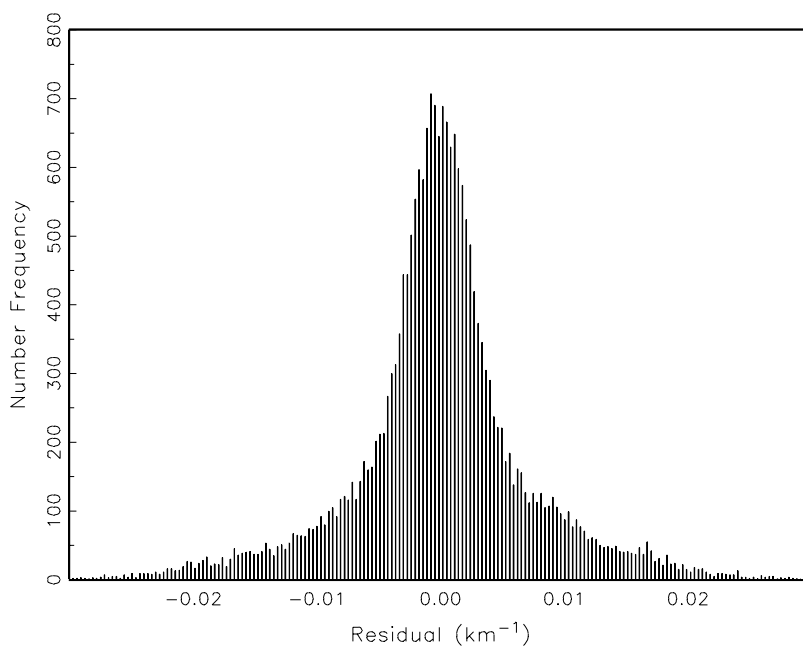


Figure 3.9 Histogram showing residual, $N4p-N4m$, where $N4p$ is the predicted value of $N4$ from regression and $N4m$ is the measured value of $N4$. This plot shows the distribution and magnitude of the random error in b_{scat} as estimated from $N4$ and $N2$.

Table 3.5 Summary of random error.

Residual	% of Residuals < 0.005 km⁻¹ Different	% of Residuals < 0.010 km⁻¹ Different	% of Residuals < 0.016 km⁻¹ Different	% of Residuals < 0.021 km⁻¹ Different
N4p-N4m	66%	85%	95%	98%
N3p-N3m	46%	75%	91%	95%

Table 3.5 shows that for neph 4, 95% of the data points, or 95% of the time, there is less than 0.016 km⁻¹ difference between the N4p and N4m. This result can be interpreted as an uncertainty due to random error (i.e., $N4=N4m\pm 0.016 \text{ km}^{-1}$). Therefore, the random error represents an uncertainty of about 2% at the higher values of the scattering coefficient, which were observed during SEAVS, about 10% at the mean value of the scattering coefficient, and about 90% near the Rayleigh scattering limit.

3.3.1.2 Comparison of Nephelometer Temperatures

The relative humidity (RH) averaged about 77% during SEAVS. The sulfate aerosol composition (or degree of neutralization) was, on average, close to ammonium bisulfate, which deliquesces at about 40% RH. This combination of a highly hygroscopic aerosol under high humidity conditions results in the water content of the aerosol being a considerable fraction of aerosol mass and volume. Since the light scattering coefficient is a function of particle size and since particle size is related to water uptake and hence RH, it is imperative that the RH inside the nephelometer be the same as the RH of the ambient aerosol if the ambient scattering coefficient is to be measured accurately. Excessive heating of the sample aerosol inside the nephelometer has historically prevented the measurement of ambient light scattering. At high humidity, a small change in temperature will produce a significant change in RH. For instance, at 25°C and 90% RH a 1°C increase in temperature will drop the RH to 84%, while a 2°C increase in temperature will reduce the RH to about 80%. At 90% RH, a two degree increase in temperature translates to about an 18% reduction in particle diameter and about a 20% reduction in the scattering coefficient b_{scat} .

During SEAVS, the modified Optec nephelometers were equipped with a water jacket that surrounded the light source and with an exhaust fan to remove heat generated by the incandescent lamp to keep aerosol heating inside the nephelometer's optical chamber to a minimum. The nephelometers were also equipped with thermistors inside the inlet, where the aerosol was assumed to be at ambient temperature and at the optical chamber outlet to measure the sample aerosol's temperature a few centimeters from where the light scattering was measured. The thermistors were tested over a range of temperatures prior to installation in the nephelometers. Matched thermistors (those which were the closest over the range of test temperatures and had less than 0.05°C difference) were installed in a nephelometer's inlet and near the scattering chamber.

Figure 3.10 shows the aerosol temperature measured in the inlet versus the aerosol temperature measured near the scattering chamber for neph 2. This plot shows there is generally less than one-

degree difference between the inlet and scattering chamber temperatures. Close analysis reveals that 20% of the data points are less than 0.5°C different, 93% of the data points are less than 1.0°C different, and 99% are less than 1.5°C different. However, there are a few data points that show about a two-degree difference in temperature between the inlet and the scattering chamber. Results of temperature comparisons for all the nephelometers are similar. Table 3.6 below shows the summary statistics of all chamber and inlet temperatures for nephs 1 through 4. All temperature units are reported in degrees Celsius.

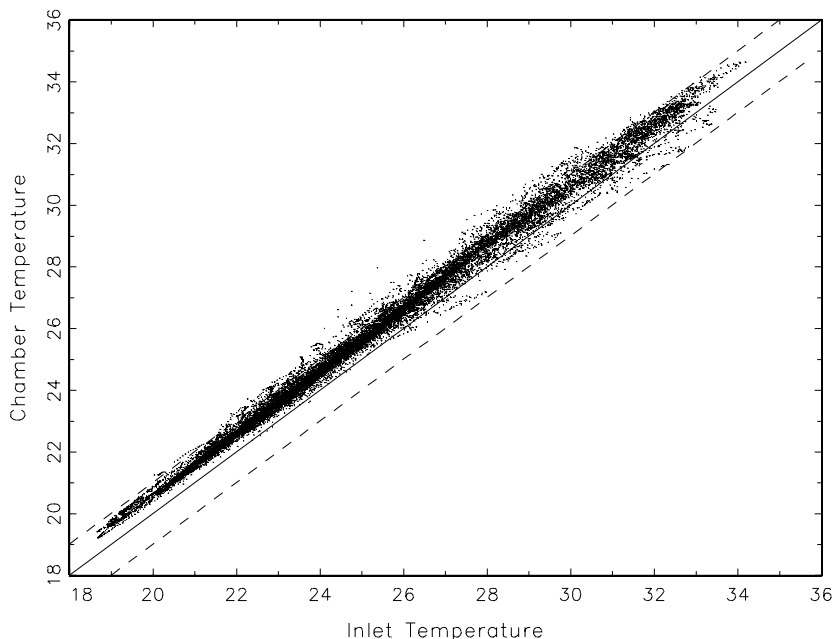


Figure 3.10 Scatter plot showing a typical comparison of nephelometer chamber and inlet temperatures during SEAVS. The dashed lines indicate $\pm 1^\circ\text{C}$ difference in temperature.

The difference in temperature between the inlet and the chamber for each nephelometer is summarized below by subtracting the mean inlet temperature from the mean chamber temperature.

$$\text{Mean } \Delta T = (\text{Mean Chamber Temperature}) - (\text{Mean Inlet Temperature})$$

Where Mean ΔT :

$$N1 = 26.03 - 25.06 = 0.97$$

$$N2 = 25.83 - 25.20 = 0.63$$

$$N3 = 25.48 - 24.68 = 0.80$$

$$N4 = 25.61 - 25.02 = 0.59$$

This analysis shows there was, on average, about 0.75°C heating of the ambient aerosol inside the nephelometers during SEAVS.

Table 3.6 Nephelometer temperatures.

Inlet Temperature	Mean Temperature	Standard Deviation	Minimum	Maximum	Number of Observations
N1	25.06	3.38	18.51	34.05	20,717
N2	25.20	3.37	18.66	34.18	20,717
N3	24.68	3.29	18.18	33.61	20,717
N4	25.02	3.33	18.41	34.03	20,717
Chamber Temperature					
N1	26.03	3.41	19.37	35.04	20,717
N2	25.83	3.36	19.21	34.64	20,717
N3	25.48	3.31	18.92	34.18	20,717
N4	25.61	3.34	19.05	34.42	20,717

3.3.2 Transmissometer

The transmissometer measures the light extinction coefficient (b_{ext}) over a given path length. Historically, transmissometry has been thought of as a teleradiometric measurement of the intensity of a light source placed at some distance, r , from an observation point. The equation governing the amount of light received at the observation point is:

$$I = \frac{I_o}{r^2} [e^{-(b_{ext})(r)}], \quad (3.5)$$

where I = the irradiance at some distance r from the light source,
 I_o = the irradiance of the light source, and
 b_{ext} = the extinction coefficient of the atmosphere.

The term (I_o/r^2) can be thought of as a calibration term that can be determined by comparison of the transmittance measurements to other optical measurements such as: (1) teleradiometer measurements made under “standard” lighting conditions, or to integrating nephelometer measurements made near the Rayleigh limit, (2) by placing the receiver and transmitter within a few hundred feet from each other and assuming $e^{-(b_{ext})(r)} \approx 1$, then $I_o = (I)(r^2)$, or (3) measurement of I at two different distances. This third technique, which was performed almost daily during SEAVS, utilizes measurement of a signal I at two different distances r , as shown below by Equations (3.6) and (3.7):

$$I_1 = \frac{I_o}{r_1^2} [e^{(-b_{ext})(r_1)}] \quad (3.6)$$

$$I_2 = \frac{I_o}{r_2^2} [e^{(-b_{ext})(r_2)}]. \quad (3.7)$$

By measuring r_1 , r_2 , I_1 , and I_2 , which are the distances between receiver and transmitter and the light intensity measured by the receiver at each distance, respectively, and by assuming the atmosphere is homogeneous over the two path lengths, then Equations (3.6) and (3.7) can be solved for b_{ext} . Once the extinction coefficient is calculated, then I_o can be calculated using either Equation (3.6) or (3.7). The daily measurement of I_o by the differential path length method reduces the uncertainty in the measurement of the extinction coefficient by reducing the uncertainty caused by lamp brightening and window transmittance and effectively calibrates the instrument daily.

3.3.3 Radiance Research Nephelometer Calibration

The calibration of the Radiance Research nephelometer is similar to the calibration of the Optec nephelometers in that the instrument is calibrated using clean air as a zero point and SUVA gas as an upscale calibration point. However, the calibration line of this instrument and the scattering coefficient are calculated internally by the instrument's computer during operation of the nephelometer as opposed to being calculated by the operator after data has been collected. The calibration technique was discussed previously in Section 3.3.1. To check the calibration of the instrument, clean air was ported into the instrument each day for one half hour and the instrument's signal was monitored. If the measured scattering coefficient went to zero during the daily clean air calibration checks, then it was assumed the calibration line was good. Once a week, however, the instrument was calibrated according to the manufacturer's guidelines in the instrument manual (Operating Procedures M903 Nephelometer), which requires setting parameters for the instrument to use in calculating the calibration line and scattering coefficient.

3.3.4 Active Scattering Aerosol Spectrometer Probe (ASASP-X) Calibration

Two aspects of this instrument are of fundamental importance for field operations: (1) focussing the aerosol stream through the center of the laser cavity and (2) maintaining the proper balance of sheath and sample air flow through the instrument's optical chamber. Polystyrene latex spheres (PSL) of a known diameter (usually 0.41 μm) were used in the field to check the alignment and ensure the instrument was sizing the particles correctly. While PSL spheres were sampled, their flow through the optical chamber could be adjusted to optimize the intensity of the instrument's signal. The sample and sheath air flows were also adjusted, while PSL was sampled, to give a single sharp monodispersed peak. At least three sample flow rate readings were taken prior to and subsequent to data acquisition for a given size distribution to ensure consistency in the sample flow during collection of size distribution data. The sample flow rate was measured using a

Gilibrator primary calibration flow meter fitted with a 250 cm³ cell. The sample flow rate was set by differencing the combined sheath plus sample flow and the sheath flow. A total flow rate of 1200 cm³ min⁻¹ and sheath flow of 1140 cm³ min⁻¹ were common, although, the sample flow rate was the only routinely measured quantity.

Calibration of the ASASP-X was performed subsequent to SEAVS. The first step in the post-experiment calibration was to measure the instrument's internal pulse height analyzer (PHA) threshold voltages. Values for the PHA threshold voltages are provided by the manufacturer [ASASP-X Operating Manual, 1977]; post-experiment calibration values were typically within 1% of the manufacturer's values. The second step in the post-experiment calibrations was to determine instrument specific calibration constants that relate particle scattering cross section to PHA threshold voltages. PSL spheres of six different diameters, ranging from 0.19 to 0.87 μm, were sampled to derive instrument calibration constants. The PHA channel with maximum counts for a given PSL size gave a PSL diameter to PHA voltage relationship. The size dependent scattering cross section (cm²) for PSLs was found from Mie theory assuming a PSL refractive index of 1.580-0i. Four calibration constants, with units of V cm⁻², were determined, which corresponded to the four amplification settings on the ASASP-X PHA. Using the instrument specific calibration constants, particle size corrections for ambient aerosol with refractive indices different from PSLs were found by Mie theory inversion [Garvey and Pinnick, 1983; Hand and Kreidenweis, 1996]. A more thorough discussion of the post-experiment calibration work, data inversion techniques, and uncertainty in derived quantities are presented in Ames and Kreidenweis [1996].

3.4 AEROSOL SAMPLERS

Bulk aerosol samples were collected for analysis of chemical composition using the IMPROVE sampler and size segregated samples were collected using an impactor (UCD DRUM sampler). The total uncertainty in the concentration of any measured species includes the combined uncertainties from: (1) measurement of sampler flow rate, (2) analytical technique, and (3) the extent of filter substrate contamination. The analytical uncertainty is a laboratory issue and is not addressed here but can be found in Eldred *et al.*, [1990] and Malm *et al.*, [1994b]. The uncertainties in flow rate and sample contamination are field issues and are discussed in the following sections.

3.4.1 IMPROVE Sampler

The IMPROVE sampler uses a critical orifice to regulate aerosol flow through the sampler. The equation for the flow rate (Q) is given by

$$Q = Q_o \left(1 - \frac{\Delta P}{P}\right) \left(\frac{T}{T_o}\right)^{1/2}, \quad (3.8)$$

where ΔP is the pressure drop across the filter, P is atmospheric pressure (assumed to be constant at a given site), T is the absolute temperature at the orifice, and Q_o is the flow rate with no filter at temperature T_o . Thus, for a given orifice the flow rate will depend on the pressure drop across the

filter and on the temperature. The flow rate change with temperature is generally small for short sampling durations because the change in temperature is generally small. From Equation (3.8) a 6°C change in temperature (for $T = 300\text{K}$) results in a change of only 1% in the flow rate. The major cause of flow rate variations is the change in pressure drop across the filter as the sample is collected. An average flow rate change due to filter loading for this sampler is approximately 3% [Eldred, 1988].

The flow rate is measured before and after collection by measuring the pressure drop across the cyclone and inlet using a Magnehelic gauge. In general, the desired parameter is the average flow rate for the duration of sample collection. If ΔP_1 and ΔP_2 are the readings before and after collection, the average flow rate for the collection period is

$$Q_{avg} = \frac{a}{2} [(\Delta P_1)^b + (\Delta P_2)^b] \left(\frac{T_{avg}}{T_c}\right)^{1/2}, \quad (3.9)$$

where a and b are constants derived from a calibration curve and, in general, are equal to 35 l min^{-1} and 0.45, respectively, T_c is the temperature at calibration, and T_{avg} is the average temperature for the collection period.

The uncertainty in the flow rate is due to three factors: (1) the uncertainty in reading the Magnehelic, (2) the uncertainty in the calibration constants, and (3) the uncertainty in the temperature variations. The combined uncertainty is estimated as 3% and has been validated by third party audits [Eldred, 1988].

The filter cassettes, used to collect aerosol samples, can be contaminated at any time between their preparation for shipment at UC Davis until the exposed filters are analyzed at the respective analytical laboratory. To estimate the extent of contamination of sample filter cassettes, field blanks are subjected to all the handling and storage that sample cassettes undergo except for actual operation in the IMPROVE sampler. A set of blank filter cassettes was done each week during SEAVS for each channel of the IMPROVE sampler.

3.4.1.1 Internal Quality Assurance Check of IMPROVE Sampler

The consistency of aerosol data is checked by comparing the concentration of sulfate ion obtained from Channel B and measured by ion chromatography (IC) with the concentration of elemental sulfur obtained from Channel A and measured by proton induced x-ray emission (PIXE). This analysis assumes all of the sulfur on both filters is in the form of sulfate ion. Figures 3.11 and 3.12 show a time line and scatter plot for molar concentrations of sulfur from PIXE and sulfate from IC. The time line shows the measured concentrations of sulfur and sulfate track each other very nicely throughout the study. The scatter plot shows that at lower concentrations (below about $0.1 \mu\text{mole m}^{-3}$) the concentration of sulfur from PIXE is slightly higher than the concentration of sulfate from IC, however, at higher concentrations sulfate from IC is slightly higher than sulfur. Regression analysis gives an R^2 of 0.989 for 81 data points. The regression line was $[\text{SO}_4^{2-}] = (1.10 \pm 0.01)[\text{S}] - (0.28 \pm 0.05)$, where the uncertainty term is the standard error from the regression analysis. The average percent difference between the two measurements was 9.57%. In general,

the agreement between these two measurements is good and shows the precision of the measurement is within about 10%.

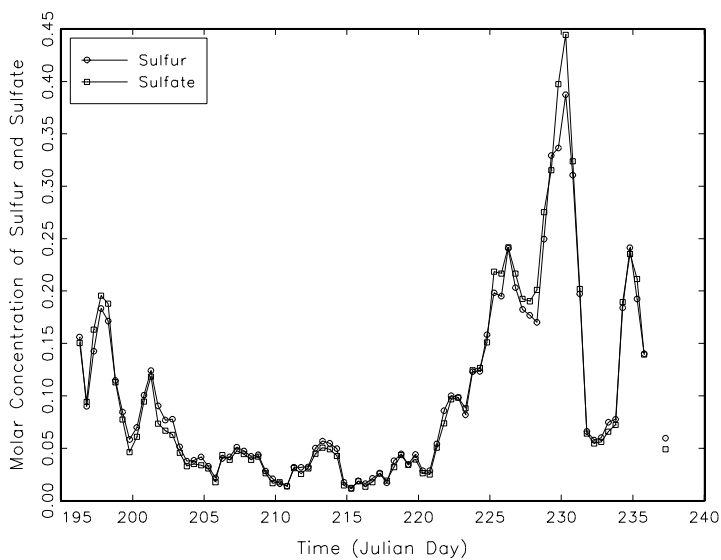


Figure 3.11 Time line showing the concentration of sulfur measured by PIXE and sulfate measured by IC.

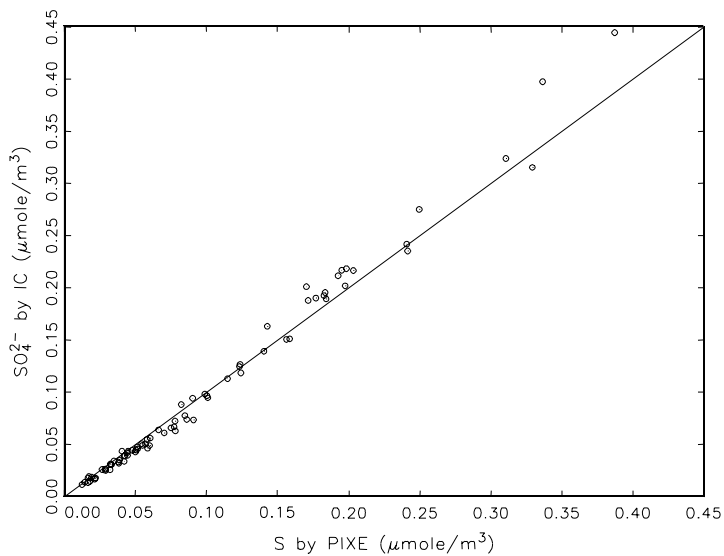


Figure 3.12 Scatter plot showing the generally good agreement between sulfur from PIXE and sulfate from IC.

3.4.1.2 Comparison of IMPROVE Sampler and Harvard HEADS Sampler

An important quality control/quality assurance aspect of SEAVS was redundant measurement of key aerosol parameters. During SEAVS the IMPROVE sampler collected two 12-hour samples beginning at 7:00 a.m. and 7:00 p.m. each day. The Harvard sampler collected one 12-hour sample beginning at 7:00 a.m. each day. We can directly compare the concentration of sulfate and ammonium ion, two key components of the ambient aerosol, obtained from the two different sampling systems for the 12-hour period starting at 7:00 a.m.

Figures 3.13 and 3.14 show a time line and scatter plot of sulfate (SO_4^{2-}) from the IMPROVE and HEADS samplers. In general, there is relatively good agreement between the two samplers, however, there are three data points (Julian day 198, 229, and 234) that show a significant disagreement between the samplers. A comparison of ammonium ion, NH_4^+ , concentration is shown in Figures 3.15 and 3.16. There is, in general, less agreement between the HEADS and IMPROVE samplers for ammonium ion than for sulfate. The HEADS sampler was about 7% higher on average. A comparison between the IMPROVE and HEADS samplers for the molar ratio of ammonium ion to sulfate, which gives an estimate of the aerosol acidity, is shown in Figure 3.17.

Table 3.7 shows summary statistics for both the Harvard HEADS (HAR.) and IMPROVE (IMP.) samplers for sampling periods in which both samplers were operated. The table shows that the two samplers agree well on average (<1% difference) for sulfate, however, the scatter plot (Figure 3.14) shows there are a few data points with a significant difference between the samplers. The two samplers also agree quite well in the concentration of ammonium ion ($\approx 7\%$ difference),

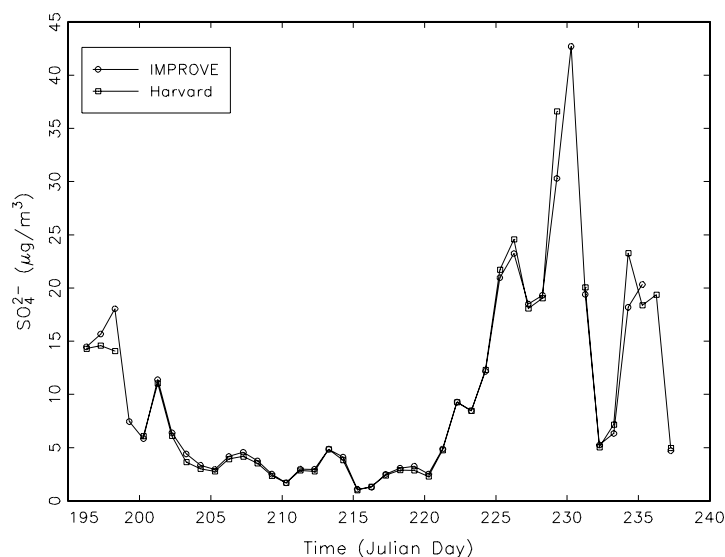


Figure 3.13 Time line showing sulfate concentration from both IMPROVE and HEADS samplers.

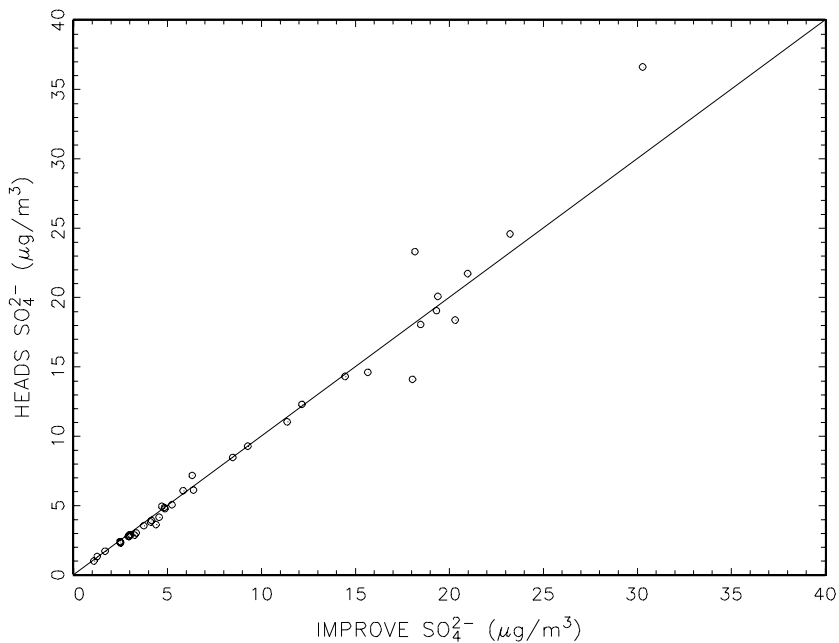


Figure 3.14 Scatter plot showing sulfate from both the IMPROVE and HEADS samplers.

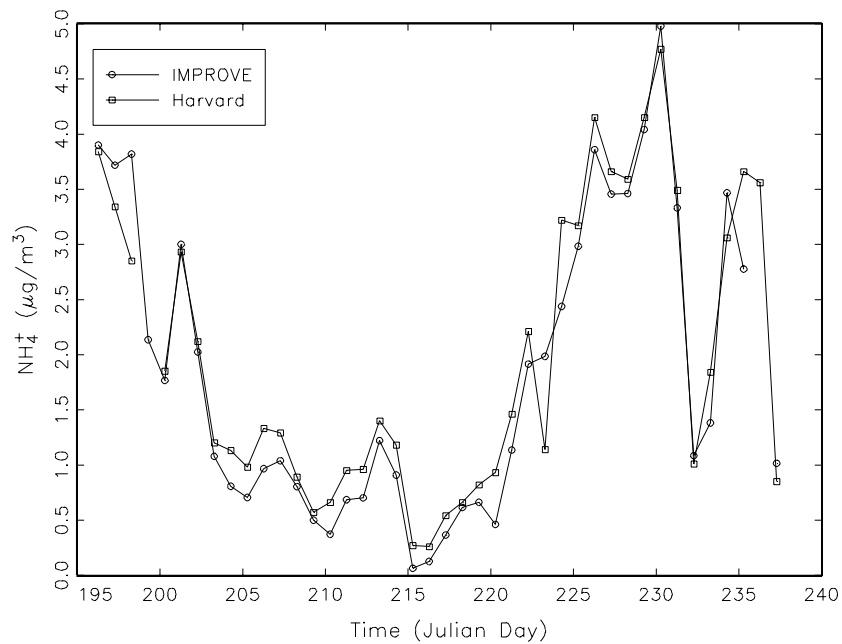


Figure 3.15 Time line showing the ammonium ion concentration measured by the IMPROVE and HEADS samplers.

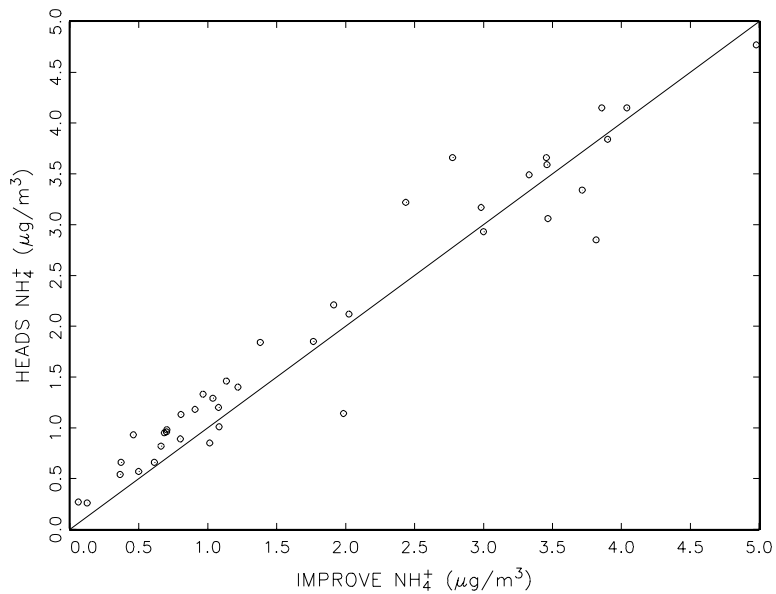


Figure 3.16 Scatter plot of ammonium ion showing comparison of concentration from IMPROVE and HEADS samplers.

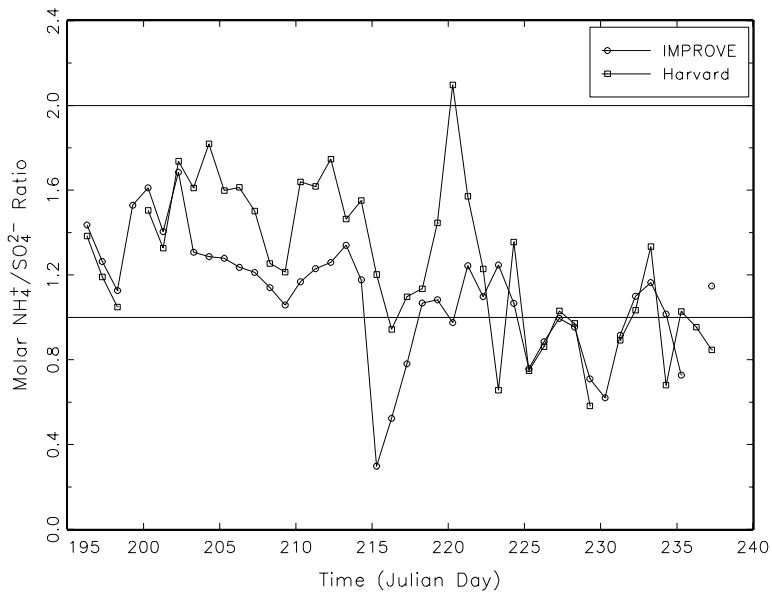


Figure 3.17 Time line showing a comparison of sulfate aerosol acidity from IMPROVE and HEADS samplers.

however, the scatter plot of data from the two samplers also shows that a few data points are quite different. Also shown in this table is the molar ammonium ion to sulfate ratio. Both samplers give an average ratio a bit higher than one that indicates the aerosol is, on average, ammonium bisulfate, which has a molar ammonium ion to sulfate ratio of one.

Table 3.7 Summary statistics for IMPROVE and HEADS samplers.

Variable	Mean	Std. Dev.	Minimum	Maximum	Number of Observations
IMP. SO ₄ ²⁻	8.94 µg m ⁻³	7.62	1.09	30.29	39
Har. SO ₄ ²⁻	9.02 µg m ⁻³	8.31	0.99	36.60	39
IMP. NH ₄ ⁺	1.76 µg m ⁻³	1.28	0.06	4.04	39
Har. NH ₄ ⁺	1.89 µg m ⁻³	1.23	0.26	4.15	39
IMP. Ratio	1.10	0.27	0.30	1.69	39
Har. Ratio	1.37	0.41	0.60	2.17	39

3.4.2 DRUM Sampler

There are no calibrations or flow checks for the DRUM sampler as a critical orifice controls sample flow and as long as a certain pressure range is maintained, sample flow will be appropriate. As a quality control aspect, however, we compare the total sulfur (sum of sulfur mass from all stages) accumulated over a given time increment with sulfur measured from the IMPROVE sampler's channel A Teflon filter. There is generally good agreement between the two samplers (a regression analysis shows an $R^2 = 0.88$). Table 3.8 shows the summary statistics for sulfur from both samplers.

Table 3.8 Statistics of sulfur mass from IMPROVE and DRUM samplers.

Variable	Mean	Std Dev	Minimum	Maximum	Number of Observations
IMPROVE [S]	4.11	3.00	0.54	12.42	45
DRUM [S]	3.87	3.00	0.37	13.08	45

3.5 REFERENCES

- Active Scattering Aerosol Spectrometer Probe PMS Model ASASP-X Operating Manual, Serial No. 805-0978-10, Particle Measuring Systems, 1977.
- Air Resource Specialists Inc., Standard Operating Procedure and Technical Instructions For Ambient Air Quality Systems, 1995.
- Ames, R. B., and S. M. Kreidenweis, Optical measurements of aerosol size distributions in Great Smoky Mountains National Park: Particle hygroscopicity and its impact on visibility. Report by Cooperative Institute for Research in the Atmosphere (CIRA), Colorado State University, Fort Collins, CO 80523, ISSN No. 0737-5352-33, 1996
- Eldred, R. A., IMPROVE Sampler Manual Version 2, Air Quality Group Crocker Nuclear Laboratory, University of California, Davis, CA., 1988.
- Eldred, R. A., T. A. Cahill, K. Wilkinson, P. J. Feeney, J. C. Chow, and W. C. Malm, Measurement of fine particles and their chemical components in the IMPROVE/NPS networks, in *Visibility and Fine Particles*, AWMA transactions series no 17, C.V. Mathai, Ed., 187-196, 1990.
- Garvey, D.M., and R.G. Pinnick, Response characteristics of the particle measuring systems active scattering aerosol spectrometer probe (ASASP-X), *Aerosol Science and Technology*, 2477:488, 1983.
- Hand, J.L., and S. M. Kreidenweis. Size corrections based on refractive index for particle measuring systems active scattering aerosol spectrometer probe. Report by Cooperative Institute for Research in the Atmosphere (CIRA), Colorado State University, Fort Collins, CO 80523, ISSN No. 0737-5352-31, 1996.
- Malm, W.C., K.A. Gebhart, J.V. Molenaar, R.A. Eldred, and H. Harrison, Pacific Northwest regional visibility experiment using natural tracers, Final Report, 1994a.
- Malm, W.C., J.F. Sisler, D. Huffman, R.A. Eldred, and T.A. Cahill, Spatial and seasonal trends in particle concentration and optical extinction in the United States, *Journal of Geophysical Research*, 99:1347-1370, 1994b.
- Molenaar, J.V., D.S. Cismoski, and R.M. Tree, Intercomparison of ambient optical monitoring techniques, presented at the 84th Annual Meeting of the Air and Waste Management Association Meeting and Exhibition, Kansas City, MO, 1992.

CHAPTER 4

AEROSOL HYGROSCOPICITY

The hygroscopic nature of fine aerosols (particles $<2.5 \mu\text{m}$) was examined by the NPS group of researchers during SEAVS. The aerosol size distribution and light scattering coefficient were measured at relative humidities ranging from $<15\%$ RH to $>90\%$ RH. The scattering coefficient was measured as a function of RH using a Radiance Research M903 nephelometer, while the aerosol size distribution was measured as a function of RH with a Particle Measuring Systems ASASP-X optical particle counter. The humidity of the sample aerosol for both instruments was controlled using Perma Pure Nafion drying tubes mounted in a “constant” temperature inlet. This system was operated such that alternating “dry” (RH $<15\%$) then “wet” (RH $>20\%$) measurements of aerosol size distributions and scattering coefficients were made.

Varying the RH of the purge air used in the Perma Pure drying tubes controlled the RH of the aerosol sample. Purge air RH was varied by increasing or decreasing the voltages to mass flow controllers that regulated the flow of dry and saturated purge air streams. By appropriately mixing the flow of dry and saturated purge air streams, any sample RH between $<15\%$ and $>90\%$ could readily be achieved. The voltages to the mass flow controllers were controlled either manually with a potentiometer or automatically with a programmed Campbell 21X data logger. Sample RH was controlled manually when both the optical particle counter (OPC) and the nephelometer were operated simultaneously. Manual control was used during OPC operation because this instrument required longer sampling periods at a single RH value. Automated RH control was used when the nephelometer alone was sampling. The sample RH and temperature were continuously monitored inside the sampling plenum (a schematic diagram is shown in Figure 2.9), at the outlet of the optical particle counter (immediately downstream of the optical cavity), and at the outlet of the nephelometer (a few inches downstream from the optical chamber). The instruments and inlet used in this experiment were described more thoroughly in Chapter 2.

4.1 AEROSOL SIZE DISTRIBUTION MEASUREMENTS AS A FUNCTION OF RH

Time lines of daily averaged “dry” (RH $<15\%$) aerosol size distribution parameters, including number concentration, volume, mass mean diameter, and geometric standard deviation derived from OPC data are shown. The time lines of “dry” aerosol data illustrate how the particle-size distribution varied during SEAVS. The “dry” data also serves as a check on the reasonableness of assumptions made for data inversions. The aerosol water uptake is reported, as D/D_o where D is the geometric mean diameter of particles at a given RH value and D_o is the geometric mean “dry” particle diameter. Finally, the measured water uptake of the ambient aerosol is compared to theoretical calculations of water uptake for a pure ammonium bisulfate aerosol.

4.1.1 Characterization of “Dry” Aerosol Size Distributions

The OPC data, obtained during measurement of “dry” aerosol, was inverted by correcting for the difference in refractive index of the polystyrene latex spheres, which were used for calibrations, and the refractive index of the “dry” aerosol. The refractive index of the “dry” aerosol was estimated using partial molar refractive indices [Stelson, 1990] and chemical composition data from the IMPROVE sampler. In these calculations, the accumulation mode aerosol (generally particles $<1.0 \mu\text{m}$) is assumed to be internally mixed and composed of sulfate, ammonium ion, and carbon (both elemental and organic). The mass of soil (i.e., elements: Si, Al, and Fe) was ignored in these calculations because only accumulation mode aerosols were considered when estimating the volume distribution parameters of the dry aerosol. This rationale is justified by the presence of a larger mode in the size distribution when the aerosol was composed of a significant fraction ($>20\%$) of soil elements. It is assumed these larger particles are composed primarily of soil elements. The refractive index of the “dry” aerosol, estimated on a daily basis, is shown in Figure 4.1. During SEAVS, the calculated refractive index ranged from 1.47 to 1.53; the mean value was 1.51. In processing the “dry” size distribution data, an index of refraction of 1.52-0i was used for Julian days (JD) 195 through 221 and 1.50-0i for JD 222 through 233.

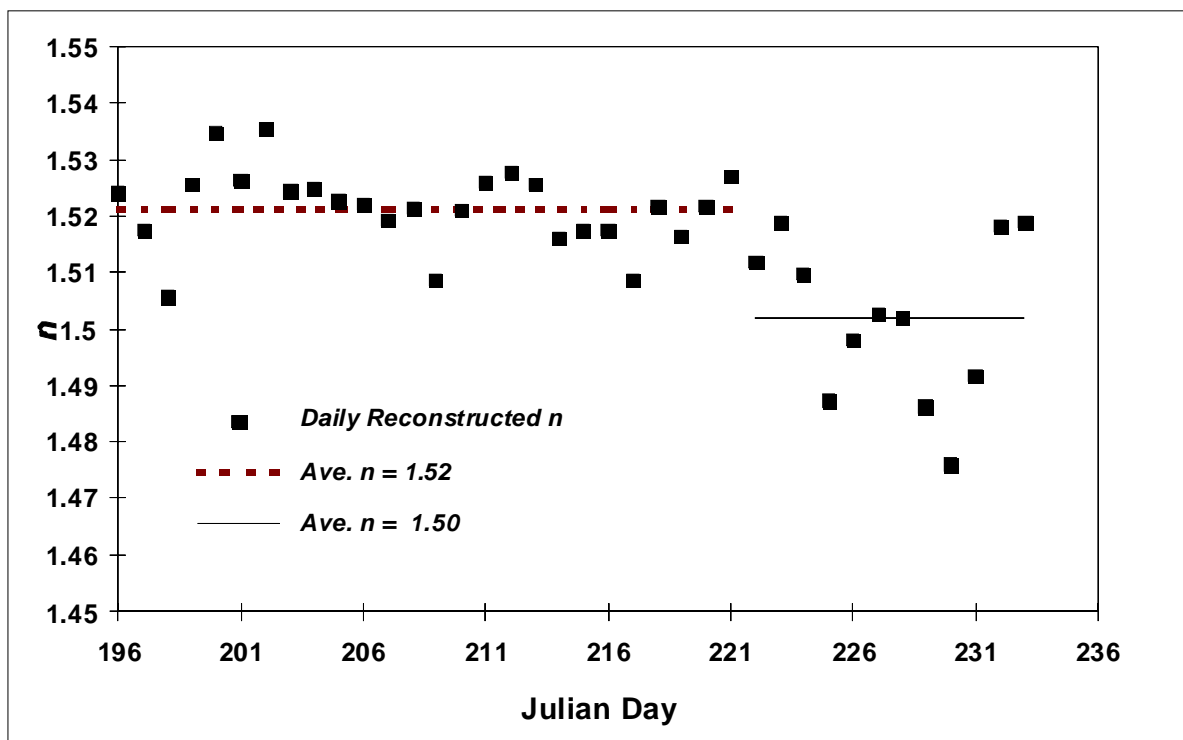


Figure 4.1 Dry aerosol refractive index, n , reconstructed using chemical data from the IMPROVE sampler. The two average refractive index values used to process OPC data are highlighted with solid and dashed lines.

A time line of daily averaged “dry” aerosol number concentration, obtained by integrating aerosol number concentration over the size range from $0.1 < \text{particle diameter } (D_p) < 2.5 \mu\text{m}$, is

presented in Figure 4.2. Daily averages of the volume distribution parameters, which include volume concentration ($\mu\text{m}^3 \text{cm}^{-3}$), mass mean diameter (MMD, μm), and geometric standard deviation (σ_g) are also displayed in Figure 4.2. The volume distribution parameters represent accumulation mode aerosol, typically in the $0.1 < D_p < 1.0 \mu\text{m}$ size range, however, the upper limit of the size range was adjusted with a floating cutoff point. The size distribution parameters were calculated using statistical formulas given in Knutson and Liou [1982]. Time periods characterized by similar meteorological conditions [Sherman *et al.*, 1996] are superimposed on this figure to illustrate how they bracket the temporal increase and decrease in the aerosol number concentration for the accumulation mode aerosol. The dry aerosol volume distribution parameter statistics calculated over the entire study period are given in Table 4.1.

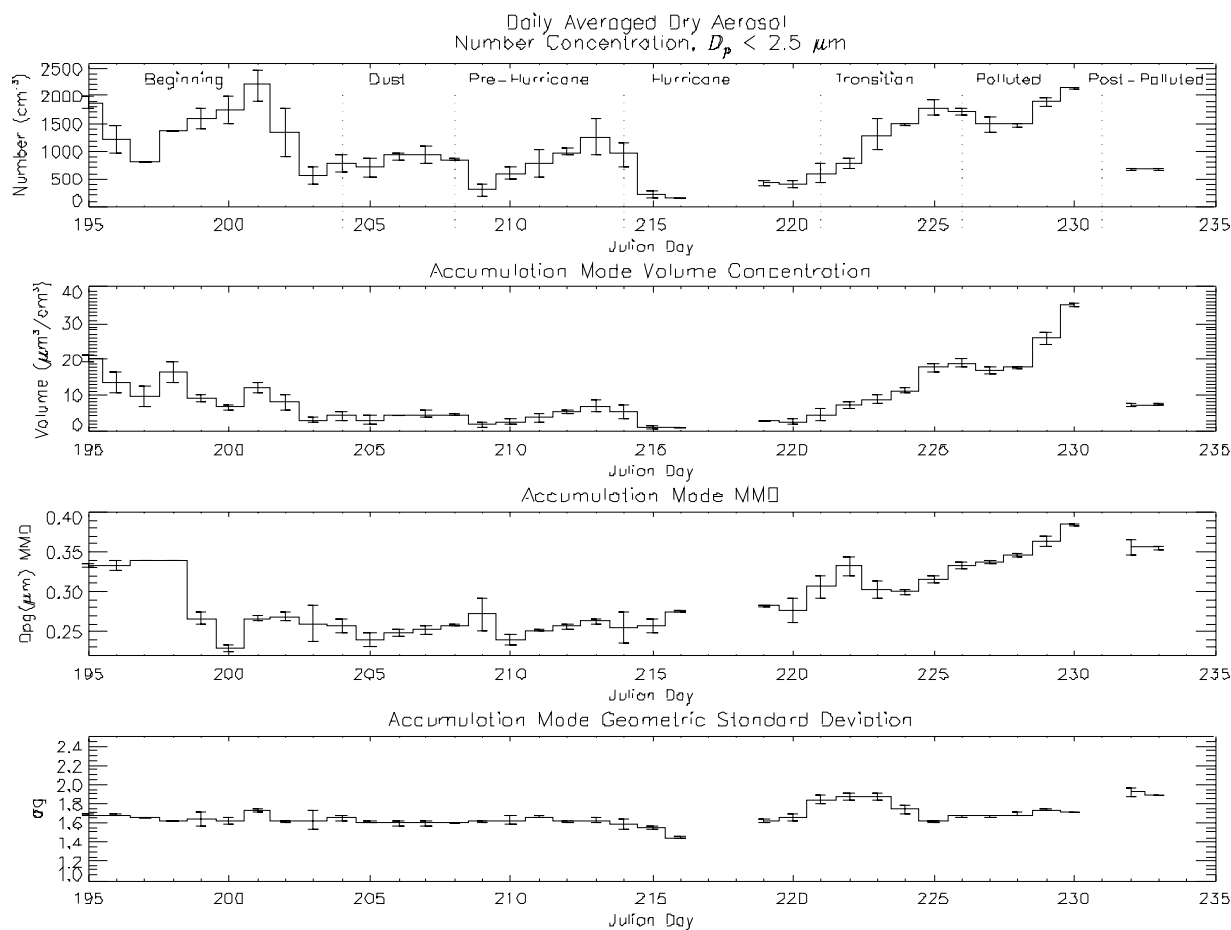


Figure 4.2 Dry aerosol size distribution parameter time lines. The first plot shows aerosol number concentration integrated over particle diameters from 0.1 to 2.5 μm . The lower three plots are volume distribution parameter time lines for accumulation mode aerosol. Time periods of similar meteorological conditions are superimposed on the number concentration time line to show the relationship between meteorological conditions and aerosol number concentration.

Table 4.1 Summary statistics of “dry” aerosol distribution parameters.

Median Volume ($\mu\text{m}^3 \text{cm}^{-1}$)	Max.	Min.	Median MMD μm	Max.	Min.	Median σ_g
6.1	34.9	1.14	0.279	0.383	0.239	1.640

4.1.2 Dry Aerosol Volume and Density

The daily averaged aerosol volume concentrations from the OPC are compared to the aerosol mass concentrations from the IMPROVE sampler to determine consistency between the two data sets. Figure 4.3 shows time lines of aerosol mass concentration from the IMPROVE sampler and aerosol volume concentration from the OPC. The fine mass (particles $<2.5 \mu\text{m}$ in diameter) shown in Figure 4.3 is the sum of sulfate, ammonium ion, total carbon (elemental plus organic), and soil elements. Figure 4.3 shows the aerosol volume concentration and aerosol mass concentration exhibit similar temporal trends throughout the study.

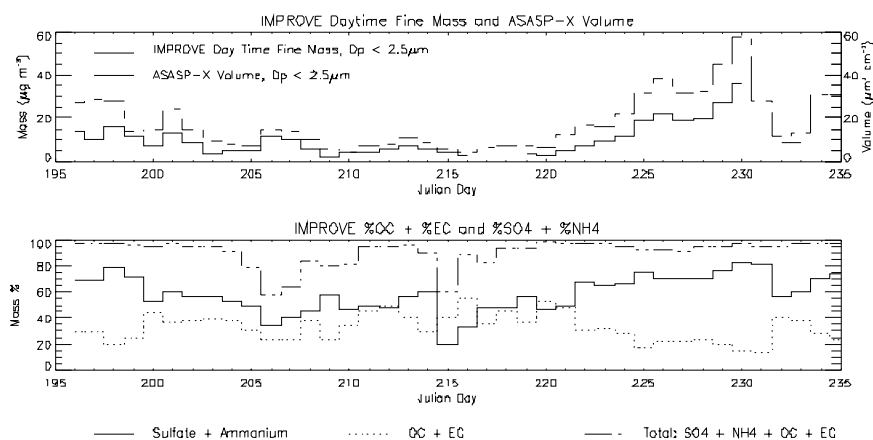


Figure 4.3 Time lines of aerosol volume concentration from the ASASP-X with aerosol fine mass from the IMPROVE sampler. Below is a time line for fine chemical mass expressed as a percent of sulfate plus ammonium, organic plus elemental carbon, and soil.

The lower plot in Figure 4.3 shows time lines of percent mass for: (1) (sulfate plus ammonium ion mass)/(total fine mass), (2) (carbon mass)/(total fine mass), and (3) (sulfate + ammonium ion + carbon)/(total fine mass). The total mass is defined as the sum of sulfate, ammonium ion, carbon, and soil elements. The predominance of sulfates and carbon is evident from Figure 4.3, with sulfate and its associated ammonium ion mass contributing to 50% or more of the fine aerosol mass on all but eight days.

The volume concentrations, shown in Figure 4.3, are not expected to include significant contributions from water, as the RH during sampling was less than 15%, however, some unknown quantity of water is almost certainly present on or within the sampled particles. Assuming water contributes little to the measured volume concentration under low (<15% RH) sampling conditions, the dry density of the aerosol can be estimated by taking the ratio of the mass and the volume concentrations. Figure 4.4 shows a scatter plot of 12-hour daytime mass concentrations obtained from the IMPROVE sampler versus volume concentration obtained from the OPC. The least squares regression line that was forced through zero gives an average density of 1.65 g cm^{-3} the median value was 1.67 g cm^{-3} . There is some scatter about the regression line, which is expected because of the chemical composition of the aerosol varied considerably during the study as shown in Figure 4.3. Some estimates of dry solute densities are listed in Table 4.2 for comparison to the experimentally derived aerosol densities. The internally mixed aerosol densities were computed assuming volume conservation of the respective pure phases. The densities calculated for mixtures of organic carbon and sulfate compounds represent the mass fraction range observed for these compounds during SEAVS. Since the OPC data used in this analysis is for $D_p < 2.5 \text{ }\mu\text{m}$, soil mass, with densities that may be greater than compounds used to calculate density in Table 4.2, may contribute to the aerosol density derived by experiment. However, the soil mass was generally small and therefore was expected to contribute little to aerosol dry density and has been neglected in these calculations.

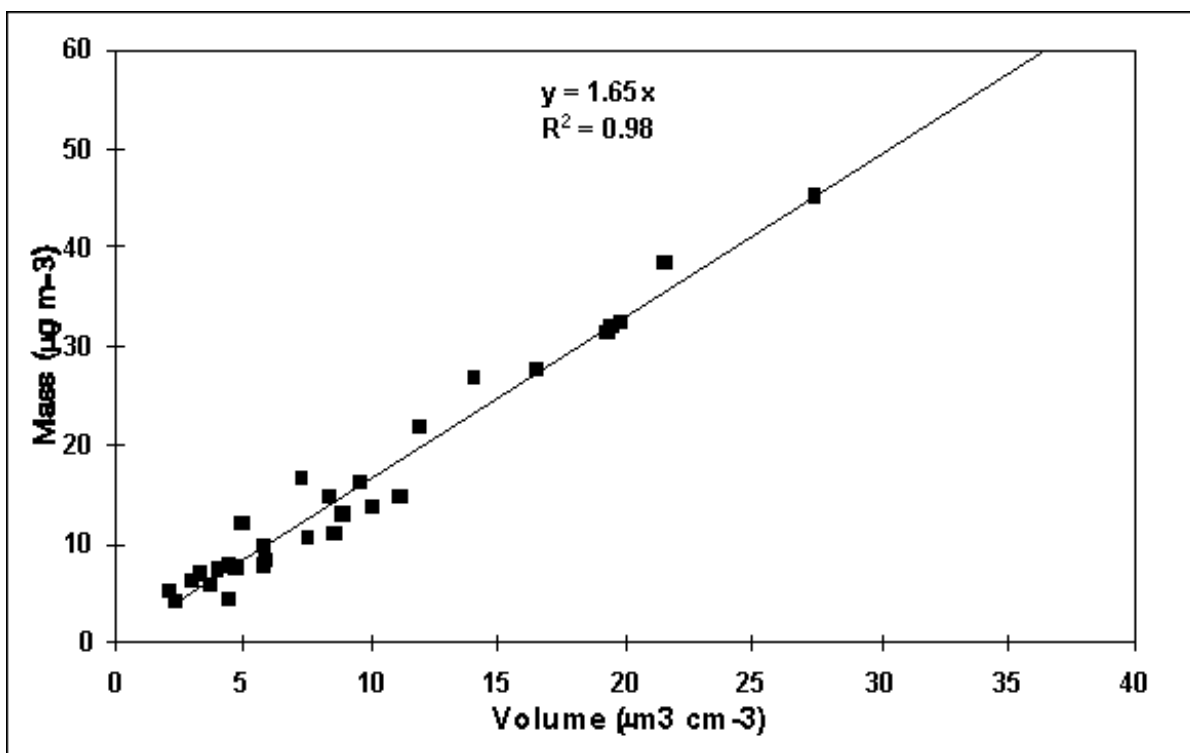


Figure 4.4 A scatter plot of dry aerosol fine mass concentration from the IMPROVE sampler and dry aerosol volume from the ASASP-X. A least squares regression of these data has a slope approximately equivalent to the median aerosol density, calculated as the mass to volume ratio for a given day.

Table 4.2 Comparison of dry density.

Compound	Density (g cm ⁻³)	Reference
Measured “Dry” Aerosol	1.67	$n = 1.520, 1.501$
Ammonium Sulfate	1.769	a
Ammonium Bisulfate	1.780	a
Sulfuric Acid (98%)	1.841	a
Organic Carbon	1.40	b
85% Ammonium Bisulfate, 15% Organic (by mass)	1.67	c
60% Ammonium Sulfate, 40% Organic (by mass)	1.63	c

n = Refractive indices to process dry aerosol distributions

^aCRC, 46th edition

^bStelson [1990]

^cCalculated by volume conservation

The quantities derived from OPC data, such as the “dry” density, depend upon the refractive index used to invert the data. The reconstructed “dry” refractive indices, shown in Figure 4.1, suggest appropriate values for inverting dry distribution data, however, to simplify data processing only two refractive index values were applied when the dry OPC data was inverted. A value of 1.52-0i was used from JD196 through JD 221 and a value of 1.501 was used from JD 222 through 232. Table 4.3 illustrates the “dry” density’s dependence on the refractive index used during data inversion. Median values and the standard deviations of calculated aerosol density are shown for: (1) the entire study period, (2) a time period of low aerosol concentration, and (3) a time period of high aerosol concentration using various indices of refraction to invert the OPC data. The median density for the entire study period calculated using an inversion refractive index of 1.53 was 1.87 g cm⁻³. This value of density is 14% greater than the value of density calculated using an inversion refractive index of 1.50. Since the aerosol parameters calculated from OPC data show a significant dependence on the refractive index used for inverting the OPC data, using a refractive index that reflects the changing aerosol composition should give more accurate results. However, the two indices of refraction used for inverting these data give reasonable results and will suffice as a first approximation.

4.1.3 Aerosol Water Uptake

In processing OPC data taken under humidified conditions, the dependence of the refractive index on water associated with the aerosol must be accounted for. Refractive index values were taken from published values [Shettle and Fenn, 1979] for a rural aerosol with similar composition to that of the aerosol measured in this study. The RH dependent refractive indices range from 1.53-

σ_i for dry conditions to 1.42- σ_i for RH >85%. These values are considered first approximations to actual values, and water uptake results herein can be revised with more accurate refractive index values if they become available.

Table 4.3 Comparison of density from different refractive indices.

Refractive Index	Median ρ_T g cm ⁻³	σ	Median ρ_L g cm ⁻³	σ	Median ρ_H g cm ⁻³	σ
1.520, 1.501	1.67	0.337	1.65	0.420	1.65	0.215
1.53	1.87	0.385	1.69	0.441	2.00	0.264
1.520	1.81	0.363	1.65	0.420	1.91	0.251
1.501	1.61	0.303	1.53	0.356	1.65	0.215

Figure 4.5 is an example of sequential dry and humidified aerosol size distributions measured by the OPC on JD 207. The first column of plots in this figure is the aerosol number distributions and the second column in the same row is the volume distributions. Moving from top to bottom in this figure portrays a series of sequential dry-humidified-dry distributions. The initial dry distribution is superimposed on the subsequent plots as a dotted line to indicate size shifts due to associated water. An obvious large aerosol mode is present in the volume distribution plots. This large mode is probably composed primarily of soil elements as data from the IMPROVE sampler indicates soil elements compose approximately 40% of the fine aerosol mass for this time period.

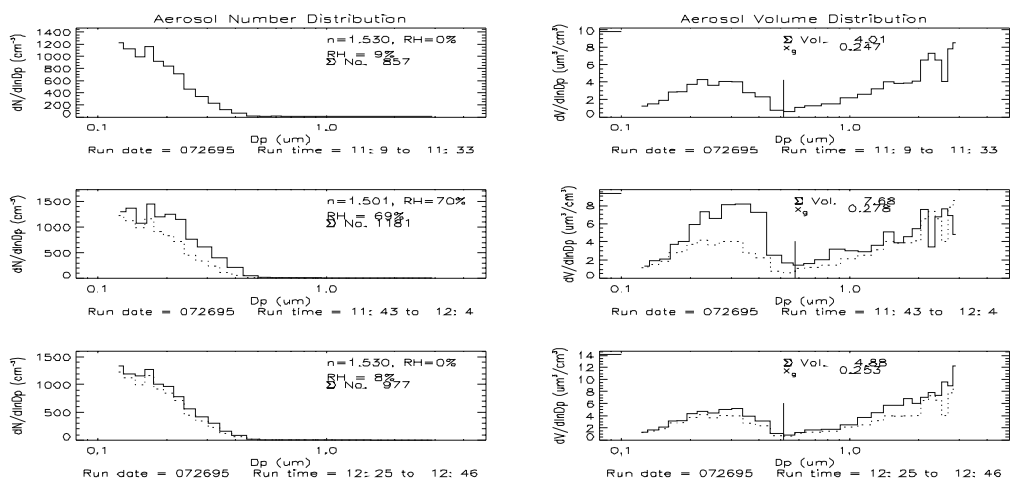


Figure 4.5 Sequential dry-humidified-dry aerosol distributions obtained on Julian day 207. The presence of a large aerosol mode corresponds to a high concentration of crustal elements observed in data from the IMPROVE sampler. The number distribution plots show the OPC data inversion refractive index (n), the RH that the inversion n applies

to, the experimental RH and total number concentration. Volume distribution plots show total volume concentration and MMD for the accumulation mode; the accumulation mode is demarcated by particle sizes less than the vertical solid line.

4.1.4 Derived Wet-to-Dry Aerosol Diameter Ratios

Particle size change as a function of RH can be expressed as a ratio of wet-to-dry particle diameter,

$$\frac{D}{D_o} = \left(\frac{V}{V_o} \right)^{\frac{1}{3}} \quad (4.1)$$

where D is the particle diameter at a given RH, D_o is the dry particle diameter, V is the wet integrated volume, and V_o is the dry integrated volume. The values of V and V_o are calculated from sequential dry then wet OPC measurements, which require approximately twenty minutes each to complete. Hereinafter the ratio D/D_o is referred to simply as R . Alternatively, R can be expressed as the volume geometric mean diameter, $D_{p,g}$ (MMD), ratio of humidified and dry aerosol volume distributions, provided the water uptake across the aerosol size distribution is homogeneous

$$\frac{D}{D_o} = \frac{D_{p,g}(Wet)}{D_{p,g}(Dry)} \quad (4.2)$$

McMurry [1996] reported size classified particles measured during SEAVS exhibited similar hygroscopic growth characteristics for particles with diameters between 0.1 and 0.4 μm , suggesting particle hygroscopicity across the aerosol accumulation mode is homogeneous.

Generally, R calculated by Equation (4.1) for the accumulation mode aerosol, and R calculated by Equation (4.2) for the entire OPC size range is consistent. However, during time periods when a significantly large aerosol mode is present, R calculated for the accumulation mode aerosol typically exceeded R calculated by including the large mode aerosol into the integrated volumes used in Equation (4.1). This apparent preferential water uptake by the accumulation mode aerosol may reflect preferential aerosol hygroscopicity, and therefore differences in aerosol chemical composition between the accumulation and large mode aerosol particles. Figure 4.6 shows value of R , calculated by the MMD ratio method (Equation 4.2). The dotted line is a polynomial best fit to the data.

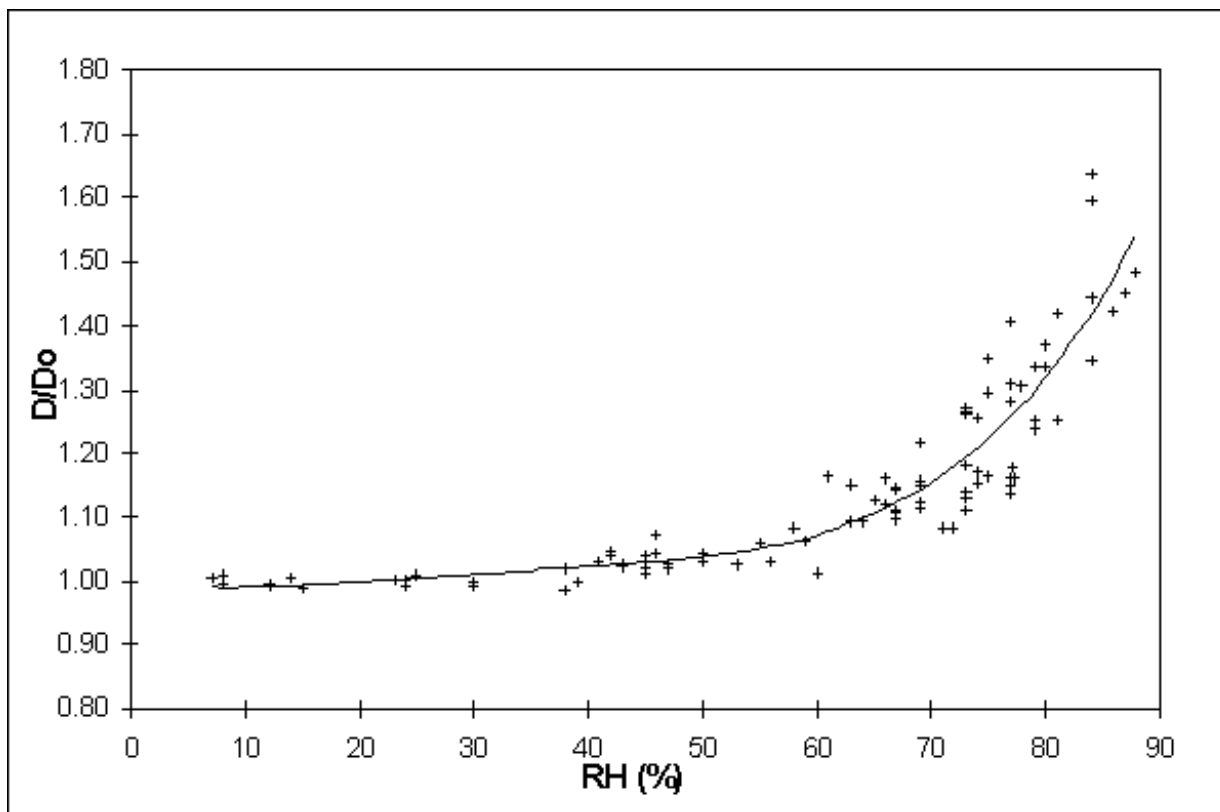


Figure 4.6 *RH dependent aerosol size change observed during SEAVS. D/D_0 values were calculated as the wet-to-dry aerosol distribution MMD ratio. The line is a polynomial best fit to the data.*

4.1.5 Comparison of Measured Water Uptake to Theoretical Water Uptake

Aerosol water uptake derived from experimental measurements is compared to estimated aerosol water uptake based on chemical mass fractions determined from IMPROVE sampler data. Aerosol hygroscopicity is estimated by adding water to the ionic mass according to empirical formulas that express pure solute water uptake. The mixing rule of Malm and Kreidenweis [1996] is used to estimate aerosol hygroscopicity from the chemical mass fractions. Sulfate, ammonium, organics, and elemental carbon are assumed the only species in the accumulation mode and are assumed to be internally mixed. In the mixing equation, sulfate and ammonium ion mass are treated as the only hygroscopic fraction and are characterized as ammonium bisulfate with RH dependent water content, expressed as R , adopted from Tang and Munkelwitz, [1994]. The crystallization branch of the ammonium bisulfate growth curve was used to estimate water uptake. Representing water uptake with ammonium bisulfate is justified by the fact that the average ammonium to sulfate molar ratio during SEAVS was close to that of ammonium bisulfate.

Figure 4.7 suggests the estimated water uptake by ionic species overpredicts actual measured aerosol water uptake. For all values of R above 36% RH, the estimated water uptake is greater than the measured water uptake by an average of 11%. Since the theoretical estimates of R correspond to the crystallization branch of the growth curve, the assumption that all soluble aerosols have

deliquesced is inherent. This theoretical estimate of aerosol hygroscopicity for the ionic fraction represents an upper limit in R provided particle acidity does not exceed that of ammonium bisulfate. If only some fraction of the particles in the size distribution have deliquesced at a given RH, for example, estimates of R would overpredict water uptake at a given RH.

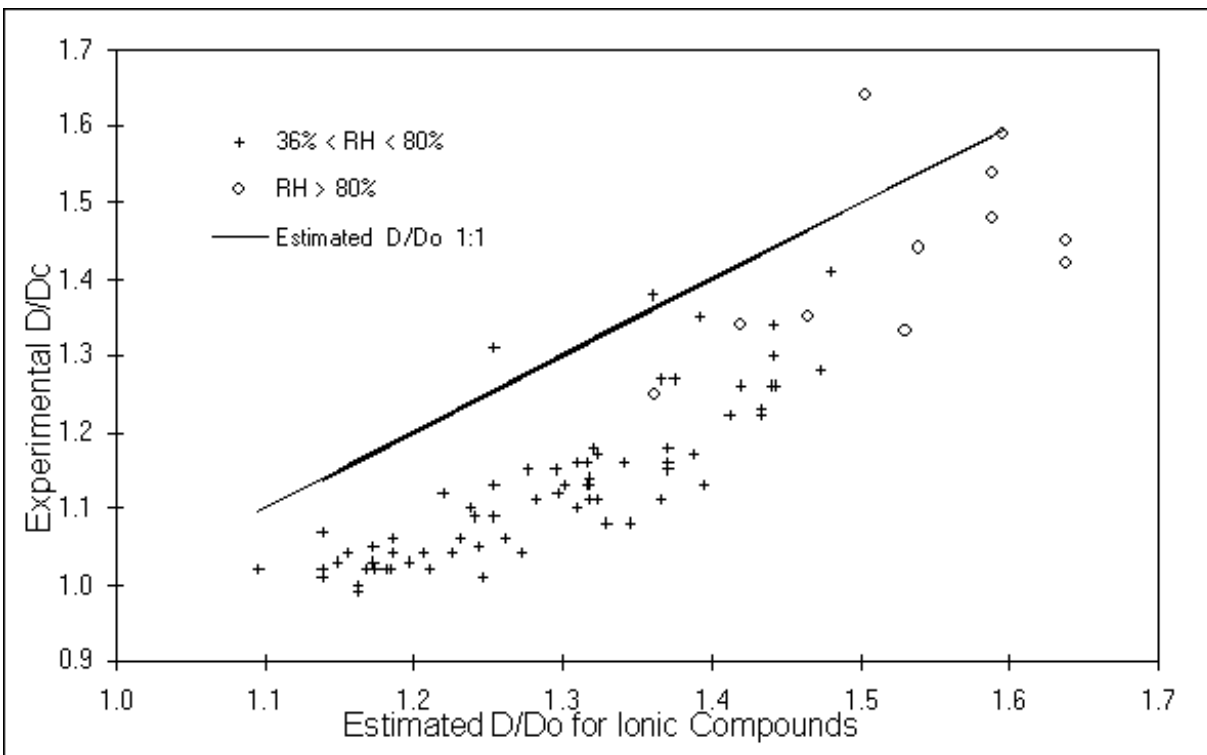


Figure 4.7 A scatter plot of experimentally determined D/D_o measured during SEAVS and theoretical estimates of D/D_o for daily averages of the ionic aerosol species. Experimental D/D_o is calculated as the wet-to-dry aerosol volume MMD ratio.

A more reliable comparison is to see if the experimental R values above 80% RH are significantly different than the estimated water uptake. Above 80% RH, all sulfate and most organics that exhibit deliquescence should have associated water and estimated water uptake should be comparable to experimental values. With this criterion applied, estimated water uptake over predicts experimental water uptake by 6%. The uncertainty in the experimentally derived data is at least 6%; therefore, these experimental data cannot be concluded to be significantly different than the estimates of water uptake for ionic species alone.

A shortcoming of the experimentally derived R estimates is the lack of detailed chemical information for accumulation mode aerosol. If some fraction of this aerosol mass is soil, or other insoluble species, then the estimated water uptake would decrease in an amount proportional to the mass of the insoluble material.

4.2 AEROSOL LIGHT SCATTERING MEASUREMENTS AS A FUNCTION OF RH

In this section, sample temperature and RH measurements and corrections to sample RH are discussed to establish the uncertainty in the RH measurement. Time lines of measurements are shown and the protocol for data reduction is given; this establishes the uncertainty in the scattering coefficient as a function of RH data set. Results of the measurements are presented and compared to various aerosol chemical compositions. Finally, the scattering coefficient measured as a function of RH is compared to that predicted from a simple model calculation.

4.2.1 Aerosol RH and Temperature Measurements

The aerosol sample's relative humidity was of fundamental importance to this experiment. The aerosol sample's RH and temperature were measured at the plenum, before entering the nephelometer, (see Figure 2.9) and at the outlet of the nephelometer. Because humidity is strongly affected by relatively small changes in temperature, an attempt was made to keep the entire sampling train at the same temperature. Keeping the temperature constant as the aerosol sample passes from the plenum and through the nephelometer will thereby keep the sample RH constant. To achieve this goal, an inlet was constructed that maintained the sample aerosol at a nearly constant temperature; the aerosol temperature, measured at the plenum, generally varied by less than 4°C per day and the average temperature throughout the study was 26.5°C .

The sample inlet, used during the study, consisted of 23 Perma Pure drying tubes mounted in parallel and housed in an insulated aluminum cylinder that was filled with water. The water bath temperature and subsequently the aerosol sample's temperature varied much less than the ambient temperature and the changes in aerosol sample temperature occurred much more slowly than the ambient temperature changes. During the study, the temperature of the aerosol sample inside the plenum was monitored and the temperature of the instrument enclosure, which housed the nephelometer and the optical particle counters, was maintained very close to the temperature of the plenum. Since the aerosol sample's temperature changed little throughout the day and because the temperature changes occurred slowly, the instrument enclosure could be maintained close to the temperature of the inlet with little effort. The temperature of the instrument enclosure was regulated manually by observing the plenum and instrument enclosure temperatures, which were displayed in real time on a computer screen, and then adjusting the temperature in the instrument enclosure using a reostated incandescent light to warm the enclosure or by porting cool air from inside the air conditioned NPS trailer into the instrument enclosure to lower its temperature. Air inside the instrument enclosure was continuously circulated using two small fans.

In general, the instrument enclosure temperature differed from the plenum temperature by less than 1°C. Figure 4.8 shows a typical time line of ambient, plenum, and instrument enclosure temperatures. The maximum temperature difference between the plenum and the instrument enclosure for Julian day 219, shown in Figure 4.8, was 0.74°C. For most of the day, the temperatures were less than 0.5°C different. The time periods when the temperatures drifted apart usually occurred during calibration of the OPC when the doors to the instrument enclosure were open. Temperature differences also occurred after prolonged OPC operation because the OPC's

power supply generated considerable heat. Since “dry” scattering measurements were often being made during the OPC calibrations, the temperature differences that occurred during OPC calibrations seldom had a significant impact on the relative humidity of the sample aerosol in the nephelometer.

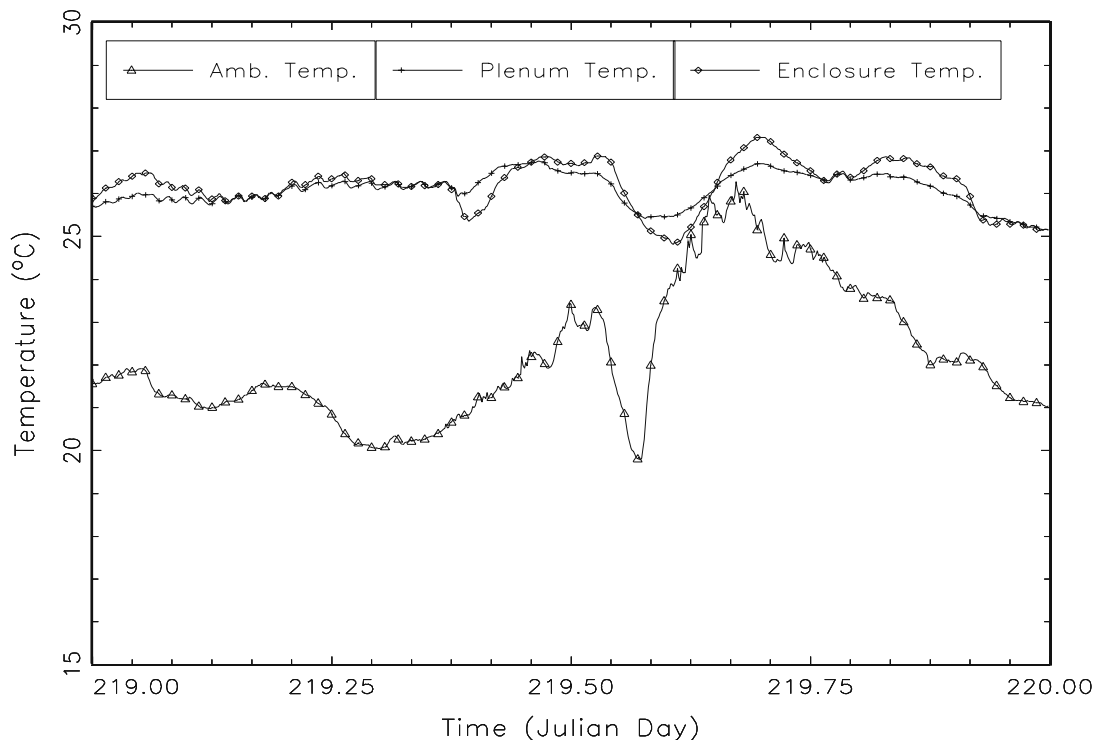


Figure 4.8 Comparison of ambient, plenum, and instrument enclosure temperatures. Showing the small temperature changes of the plenum, relative to ambient temperature changes, and the small difference in temperature between the plenum and the instrument enclosure.

There were time periods, however, when the temperature measured in the plenum (water bath temperature) was significantly different ($>2^{\circ}\text{C}$) from the temperature of the instrument enclosure. During these time periods there was often a correspondingly large difference between the RH measured at the plenum and the RH measured at the outlet of the nephelometer. The large difference between the RH measured at the plenum, before entering the nephelometer, and the RH measured at the outlet of the nephelometer leads to unacceptable uncertainty in the RH of the sample inside the nephelometer. Therefore, data collected during time periods when the plenum and instrument enclosure temperatures differed by more than 2°C and the RH differences exceeded 5% are not reported. Data, collected when the temperature difference between the plenum and outlet of the nephelometer was less than 2°C , were corrected for the expected change in RH that would occur for the measured change in temperature.

The temperature of the instrument enclosure, plenum temperature, plenum RH, and the analog b_{sp} signal from the nephelometer were recorded by a Campbell 21X data logger on two-minute averages. The temperature and RH of the sampled aerosol at the outlet of the nephelometer as well as the serial b_{sp} signal were logged by the nephelometer on five-minute averages. A comparison of

10-minute averaged data showed the instrument enclosure and outlet of the nephelometer were essentially in thermal equilibrium (nearly always $<0.5^{\circ}\text{C}$ difference). Since the temperature inside the instrument enclosure and the temperature at the outlet of the nephelometer agreed, and since it was advantageous to use the 2-minute averaged data set as opposed to the 5-minute averaged data set, the RH of the sample was corrected using the RH and temperature measured in the plenum and the temperature measured in the instrument enclosure. Figure 4.9 shows a typical comparison of the RH measured in the plenum and the RH calculated from the change in temperature between the plenum and nephelometer.

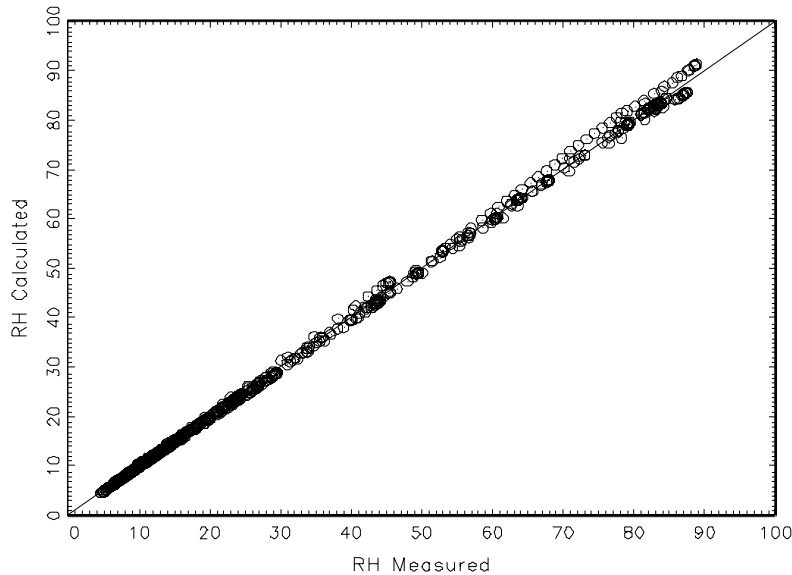


Figure 4.9 Scatter plot showing the typical difference between RH measured in the plenum and the RH corrected for the change in temperature between the plenum and the nephelometer.

The temperature inside the nephelometer's scattering chamber is unknown, however, it is assumed to be somewhere between the temperature measured at the plenum and the temperature measured at the outlet of the nephelometer. At higher RH values, the largest part of the uncertainty in the RH measurement is caused by the uncertainty in sample temperature. Since the instrument enclosure temperature and the outlet of the nephelometer were always within 0.5°C , an uncertainty in temperature of 0.5°C is assumed. The corrected RH values are reported graphically with error bars, which bound the possible RH values. The RH error bars are calculated using the temperature uncertainty of $\pm 0.5^{\circ}\text{C}$.

4.2.2 Aerosol Light Scattering Measurements

The scattering coefficient was measured while the RH of the aerosol sample was cycled from "dry" (RH $<15\%$) to humid (RH $>20\%$) and back to "dry" again. During automated RH control, each cycle required one hour to complete, however, during manual RH control the time between humid and dry measurements varied. Figure 4.10 shows a typical time line of the aerosol sample's

RH, represented as a fraction, and the scattering coefficient measured during automated RH control. Note that: (1) the RH of the sample is increased in increments of $\approx 20\%$ for each successive cycle, (2) there are at least three data points when the sample's RH is nearly constant ($<0.5\%$ RH difference between the data points) at the top of each cycle, and (3) there are, in general, several data points for $\text{RH} < 15\%$ at the beginning and at the end of each cycle. The three data points, obtained under humidified conditions when the sample's RH was nearly constant, were averaged to give one data point per cycle for sample RH and one data point per cycle for the scattering coefficient. The data points at the beginning of each cycle were averaged and the data points at the end of each cycle were averaged to give two "dry" scattering coefficient measurements for each cycle. Using this sampling procedure and this data acquisition criterion, one value of sample RH measured at an $\text{RH} \geq 20\%$, one value of the scattering coefficient corresponding to the RH value, and two "dry" scattering coefficient values are obtained for each RH cycle.

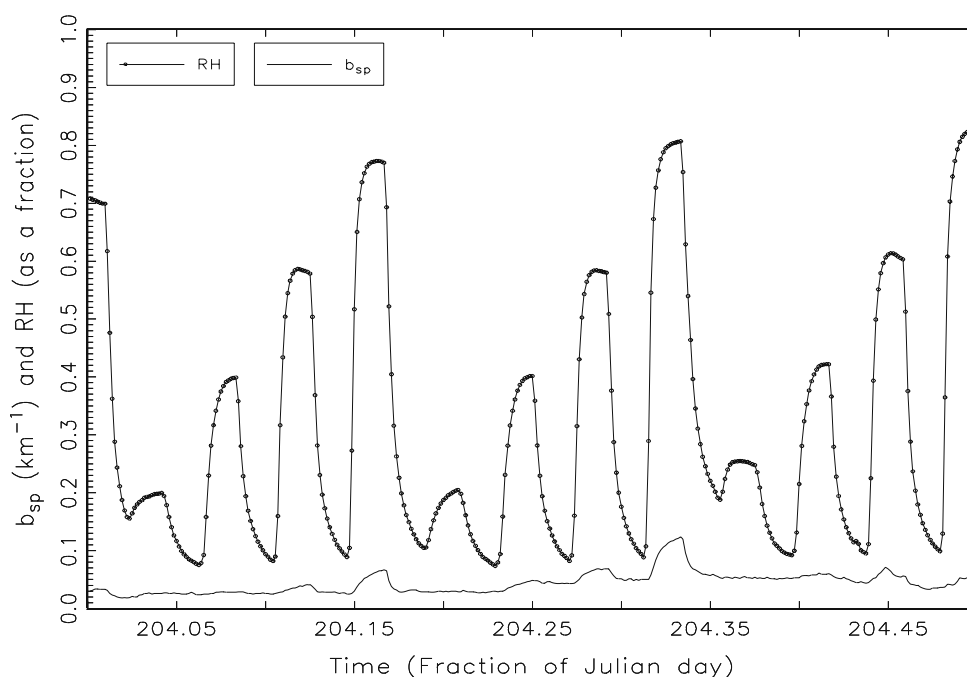


Figure 4.10 Time line showing the hourly RH cycle and subsequent change in scattering coefficient response to RH.

The ratio of b_{spw}/b_{spd} , where b_{spw} represents the scattering coefficient for some RH value $\geq 20\%$ and b_{spd} represents the "dry" scattering coefficient, is used to report the light scattering coefficient as a function of RH. The magnitude of the "dry" scattering coefficient, b_{spd} , measured at the beginning of a cycle, however, was sometimes considerably different than b_{spd} measured at the end of the same cycle. An example is shown in Figure 4.11. Note the dry scattering coefficient, emphasized by the first dashed line, is approximately 0.030 km^{-1} at 5:30 a.m. (204.25 as fraction of Julian day = 6:00 a.m.), however, one hour later the "dry" scattering coefficient, emphasized by the second dashed line, is approximately 0.044 km^{-1} . This represents about a 47% increase in the dry scattering coefficient over the duration of the RH cycle and leads to considerable uncertainty in the ratio b_{spw}/b_{spd} . However, if the increase in the scattering coefficient is relatively smooth and linear

over the time interval of the RH cycle, which was verified using b_{scat} values obtained from the ambient Optec nephelometers, then the mean of the “dry” measurements will be a reasonable estimation of the dry scattering coefficient at the time b_{spw} was measured. Therefore, the mean “dry” scattering coefficients, measured at the start and end of each cycle, were used to calculate the ratio. Furthermore, if the increase in the “dry” scattering for each RH cycle is relatively smooth and linear, the maximum value of the “dry” scattering coefficient will establish the minimum value for the ratio, while the minimum value of b_{spd} will establish the maximum value for the ratio. The data reported here uses the average value of b_{spd} to report the ratio and minimum and maximum values of b_{spd} to bound the ratio.

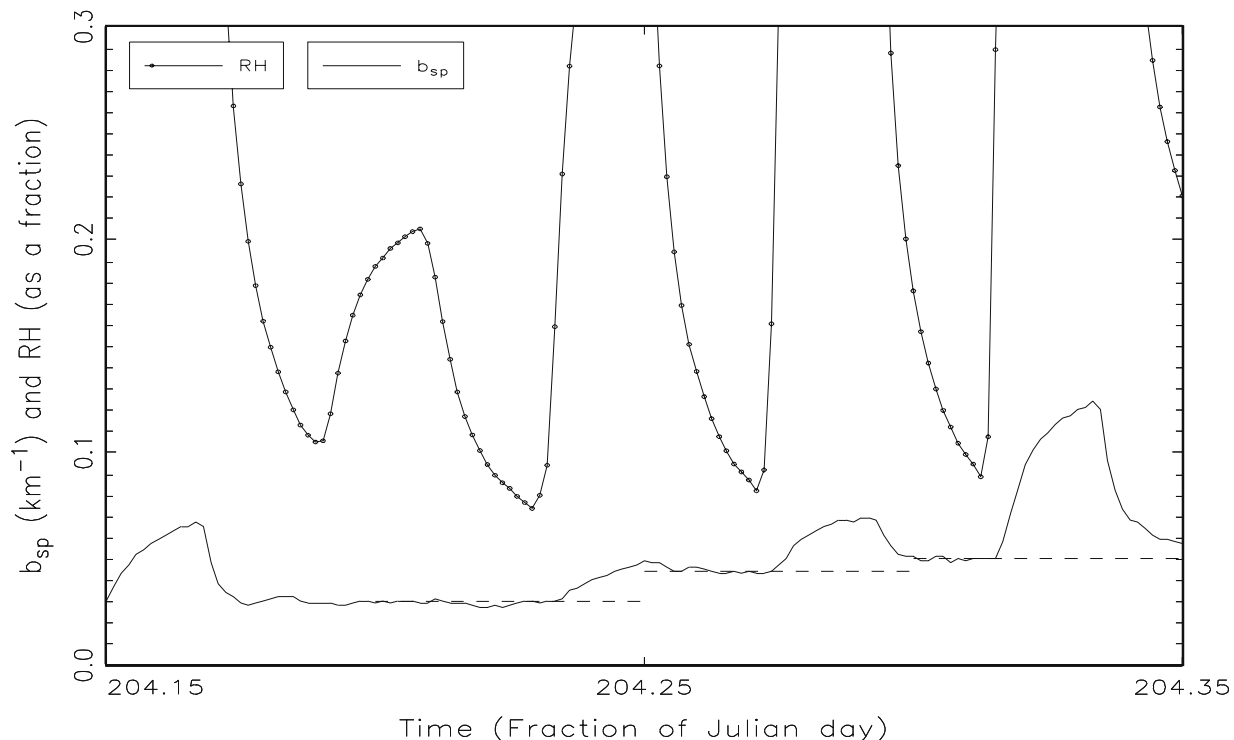


Figure 4.11 High resolution time line showing the change in “dry” scattering coefficient, which was often observed during an RH cycle. Large changes led to considerable uncertainty in the ratio used to report the change in scattering as a function of RH because the dry scattering was not known precisely when the humidified scattering was being measured.

4.2.3 Aerosol Light Scattering Data

The light scattering coefficient, measured as a function of RH and reported as the ratio of b_{spw}/b_{spd} , is shown in Figure 4.12. Note the scattering ratio, b_{spw}/b_{spd} , exhibits a smooth and continuous increase as the sample RH increases. No light scattering coefficient data, obtained during this study, exhibited an abrupt change as the aerosol’s humidity was either increased or decreased as would be expected if a large fraction of the aerosol particles were undergoing deliquescence or crystallization. This infers that at least a large fraction of ambient aerosol particles that were sampled during this study absorb water when the RH is increased and release water when RH is decreased in a smooth and continuous manner. Furthermore, since the scattering coefficient

did not decrease abruptly under low RH conditions, which would be expected if a large fraction of the aerosol particles abruptly crystallized, it is possible the aerosol particles were never completely dried to the point of crystallization.

Figure 4.12 also shows there are large variations in the magnitude of the ratio over small ranges of RH and the error bars, which bound the ratio, often times do not overlap. This suggests the observed differences are probably real. The larger differences in the ratio primarily occurred over longer time periods (i.e., days) and the data suggests the larger differences in the ratio are related to aerosol chemical composition. Figure 4.13 shows the scattering ratio as a function of RH and the chemical composition of the bulk aerosol for three different time periods during SEAVS. Note that the soluble inorganic fraction, which is composed primarily of sulfate, SO_4^{2-} , and ammonium ion, NH_4^+ , with smaller contributions to the soluble inorganic mass fraction from NO_3^- , Na^+ , and Cl^- , dominates the aerosol fine mass on Julian day 224 and the scattering ratio is considerably higher than either day 207 or day 211, which are dominated by soil and organic compounds, respectively.

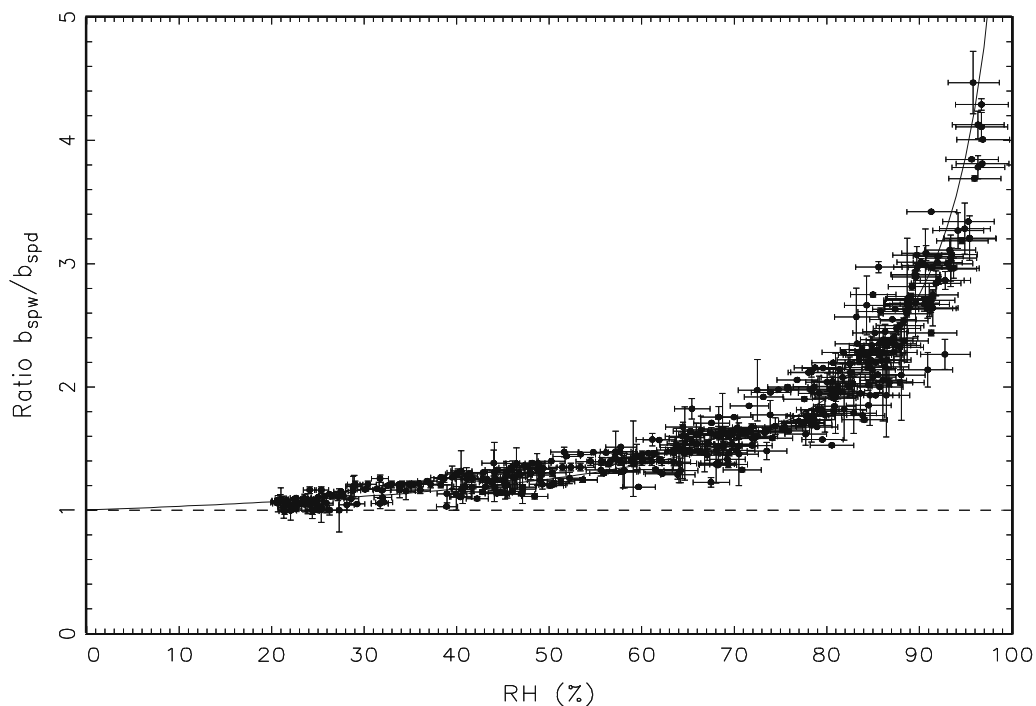


Figure 4.12 Plot showing the ratio of humidified scattering coefficient over “dry” scattering coefficient versus sample RH for all valid data obtained during SEAVS.

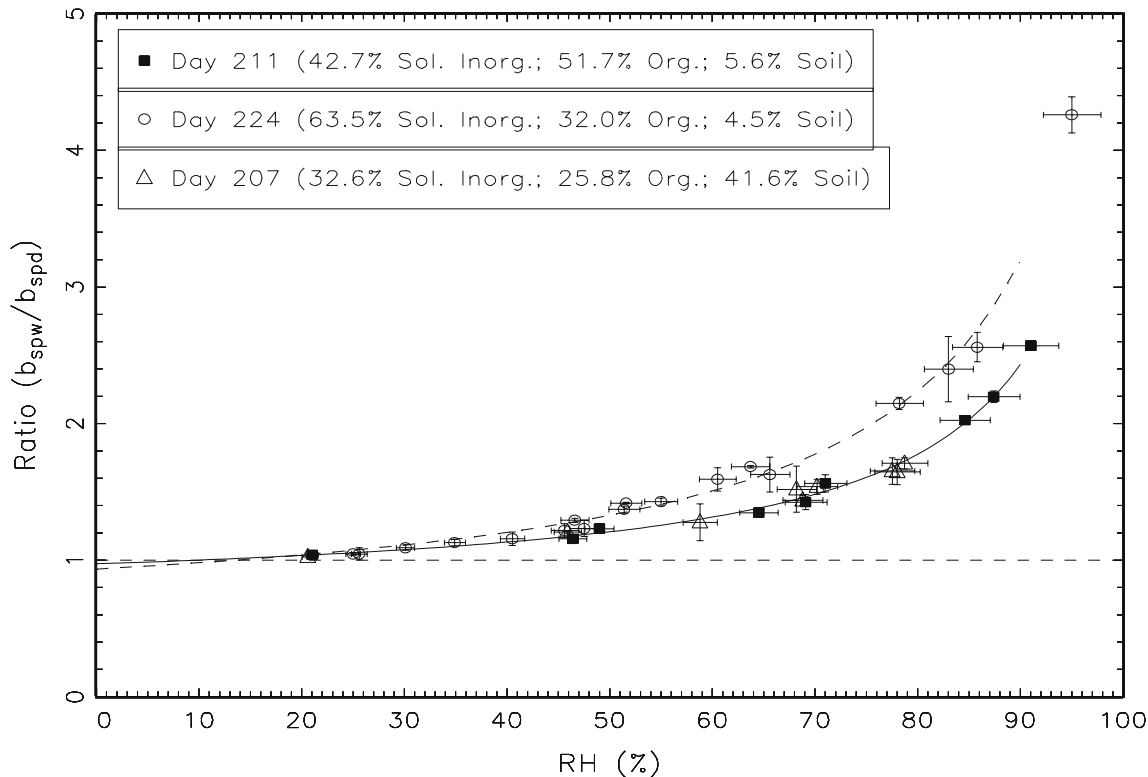


Figure 4.13 Plot showing the significantly different light scattering coefficient ratios that were observed for different aerosol compositions during SEAVS.

4.2.4 Comparison of Measured Scattering Ratio to Model Calculations

The scattering ratio, b_{spw}/b_{spd} , is compared here to a simple aerosol scattering model that utilizes aerosol mass, size distribution data for sulfate, and empirical aerosol growth curves to estimate the scattering coefficient. The equation used for estimating the scattering coefficient was:

$$b_{sp} = (eff_{sul})[sulfate](f(RH)) + 3[nitrate](f(RH)) + 4[organic] + 1[soil] \quad (4.3)$$

where (eff_{sul}) is the mass scattering efficiency for sulfate, which was calculated from the sulfate size distribution and Mie theory; the values 3, 4, and 1 are the assumed mass scattering efficiencies, which have units of $m^2 g^{-1}$, for nitrate, organic carbon, and soil, respectively; the term inside the brackets is the mass of the species measured by the IMPROVE sampler; and $f(RH)$ is an empirical growth function. The development of this model is fully discussed in sections 5.4.1 and 5.4.2.

To compare the measured scattering ratio to the scattering ratio obtained from the model calculations, Equation (4.3) is first computed without the growth term, $f(RH)$, which is associated with sulfate and nitrate only, to calculate the dry scattering coefficient. This produces an average dry scattering coefficient for the 12-hour IMPROVE sampler measurement period. Then Equation

(4.3) is recalculated using the $f(RH)$ term, which produces the scattering coefficient as a function of RH. Dividing the scattering coefficient values by the dry scattering coefficient value gives the model's scattering ratio as a function of RH, which can be compared directly to the scattering ratio measured as a function of RH.

Figures 4.14, 4.15, and 4.16 show the measured scattering ratio, indicated by the data points, and the modeled scattering ratio, indicated by the solid lines. Note that, in general, the modeled scattering ratio is slightly higher than the measured scattering ratio. This suggests the ambient aerosol may absorb slightly less water than is predicted from this model using empirical growth curves.

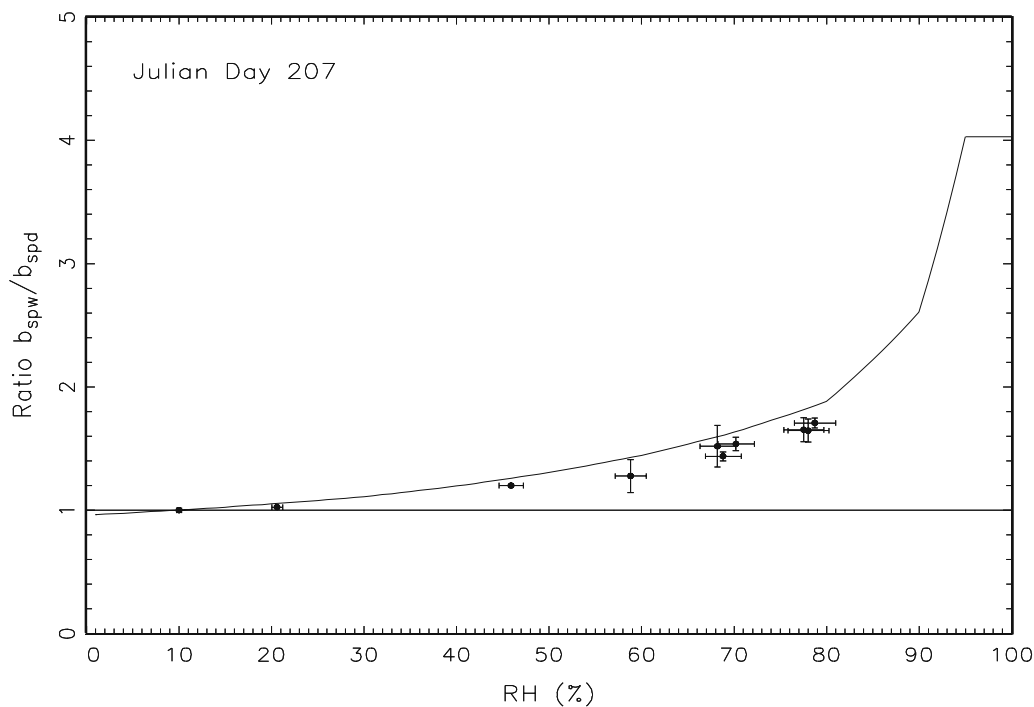


Figure 4.14 Comparison of measured scattering ratio and modeled scattering ratio versus RH.

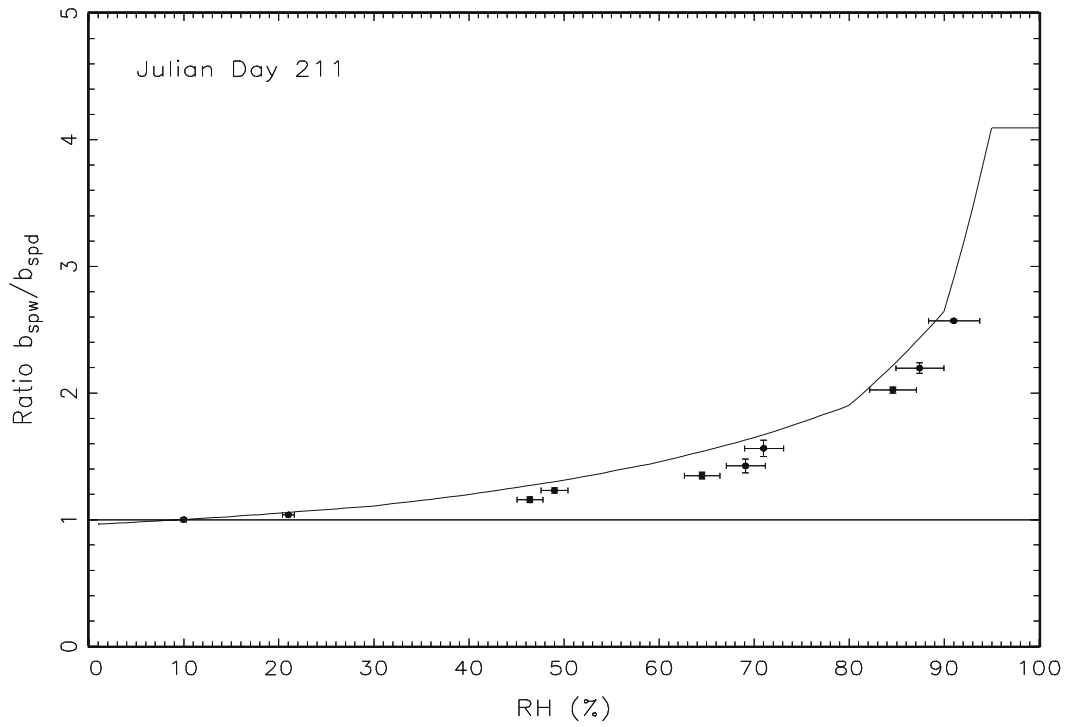


Figure 4.15 Comparison of measured scattering ratio and modeled scattering ratio versus RH.

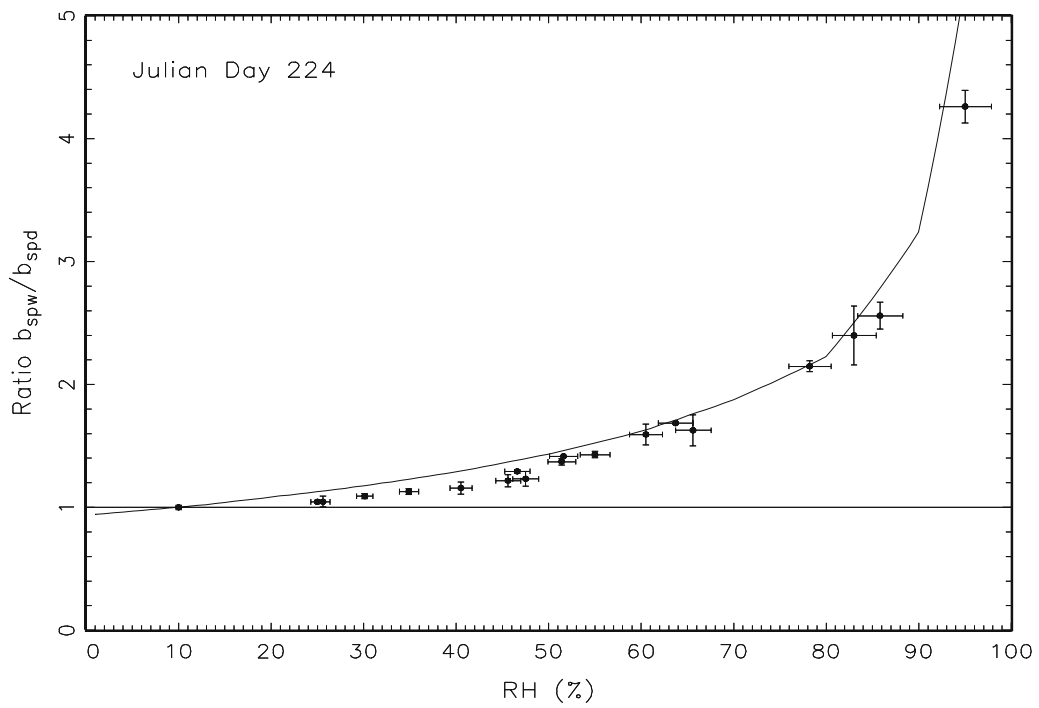


Figure 4.16 Comparison of measured scattering ratio and modeled scattering ratio versus RH.

4.3 REFERENCES

- Knutson, E.O. and P.J. Liroy, Measurement and presentation of aerosol size distributions, In air sampling instruments for evaluation of atmospheric contaminants, 7th edition, American Conference of Governmental and Industrial Hygienists, Cincinnati, Ohio, 1982.
- Malm, W.C. and S.M. Kreidenweis, The effects of aerosol hygroscopicity on the apportionment of extinction, submitted for publication in *Atmospheric Environment*, 1996.
- McMurry, P.H., Measurements of haze and visual effects, TDMA data report for the Southeastern Aerosol and Visibility Study, Electric Power Research Institute (EPRI), 1996.
- Sherman, D.E., R.B. Ames, and S.M. Kreidenweis, Influence of synoptic and local meteorological conditions on ambient total particle concentration during SEAVS, Paper No. 188, presented at the 13th ACS Rocky Mountain Regional Meeting, Denver Colorado, June 9-12, 1996.
- Shettle, E.P., and R.W. Fenn, Models for the Aerosols of the lower atmosphere and the effects of humidity variations on the optical properties, Environmental Research Paper, No. 676, AFGL-TR-79-0214, 1979.
- Stelson, A.W., Urban aerosol refractive index prediction by partial molar approach, *Environmental Science and Technology*, 24(11): 1676-1679, 1990.
- Tang, I.N., and H.R. Munkelwitz, Water activities, densities, and refractive indices of aqueous sulfates and sodium nitrate droplets of atmospheric importance, *Journal of Geophysical Research*, 99(D9): 18801-18808, 1994.

CHAPTER 5

DATA ANALYSIS

5.1 DETERMINATION OF AEROSOL TYPES

The fine aerosol species at most continental sites are classified into five major types: sulfates, nitrates, organics, light-absorbing carbon, and soil. Other fine species such as nonsoil potassium, sea spray, and other trace elements, are less important from a visibility standpoint. Methods for apportionment of measured mass to the various aerosol species are detailed in Malm *et al.* [1994] and only a summary will be presented here.

Most fine sulfates are the result of oxidation of SO₂ gas to sulfate particles. In humid atmospheres, the oxidation typically occurs in clouds where sulfuric acid is formed within water droplets. If there is inadequate ammonia in the atmosphere to fully neutralize the sulfuric acid, as is sometimes the case, then the resulting aerosols are acidic. Under these circumstances solutions of continuously varying acidity are formed. The extremes of this continuum are ammonium sulfate (neutral) and sulfuric acid.

Because it is the ambient aerosol cross section that is important from a visibility perspective, assumptions need to be made about the molecular form of sulfur. The multiplicative factor (mcf) for elemental sulfur or sulfate ion depends on the degree of neutralization of the sulfuric acid produced by conversion of SO₂. The mcf is determined by interpolating between the mass of fully neutralized, half neutralized, and sulfuric acid based on the measured ammonium to sulfate ion ratio. The mcf for fully, half neutralized, and sulfuric acid are:

SULFATE FORM	EQUATION	NEUTRALIZATION
(NH ₄) ₂ SO ₄ :	[SULFATE]=4.125[S]	100%
(NH ₄)HSO ₄ :	[SULFATE]=3.594[S]	50%
H ₂ SO ₄ :	[SULFATE]=3.063[S]	0%

The brackets indicate the mass of the aerosol species or element.

Many authors have noted the acidity of aerosols during the summer months in the eastern United States [Pierson *et al.*, 1980, Ferman *et al.*, 1981; Ferek *et al.*, 1983; Malm *et al.*, 1991; Day *et al.* 1997]. On the average sulfates were reported to be only half neutralized (NH₄)HSO₄ at many eastern monitoring sites.

An average ambient organic particle is assumed to contain constant fractions of carbon (f_{OC}) and hydrogen (f_{OH}) by weight. Organic mass concentration from channel C (OMC) is simply the sum of OCLT and OCHT adjusted by the molar correction factor $1/f_{OC}$:

$$[OMC] = (1/f_{OC})([OCLT] + [OCHT]). \quad (5.1)$$

For this report, a value for f_{OC} of 0.71 is used, which gives a reciprocal factor of 1.4 [Watson *et al.*, 1988].

Organic mass can also be estimated from the concentrations of H and S measured on the channel A Teflon filter if certain assumptions are made. It is assumed that during exposure to the vacuum of the channel A PIXE (particle-induced x-ray emission) and PESA (proton elastic scattering analysis) analyses, all nitrates and water volatilize and do not contribute to the mass of H. It is further assumed that the remaining hydrogen can be apportioned between sulfates and organic carbon. This is denoted as OMH. Assuming full neutralization of the sulfate ion, OMH is calculated by:

$$[OMH] = (1/f_{OH})([H] - f_S[S]). \quad (5.2)$$

The sulfur factor, f_S , is derived from the H/S ratio for the estimated sulfate species. $1/f_{OH}$ is operationally defined by forcing OMC to equal OMH. Comparison of OMH to OMC is used in data validation procedures and OMH is used to estimate organic mass when carbon is not explicitly measured.

Assuming that the collected nitrate ion is associated with fully neutralized nitrate aerosol (NH₄NO₃), the nitrate mass is estimated by using a multiplication factor of 1.29.

Elemental carbon is defined as the sum of E1+E2+E3 or more conventionally as:

$$[LAC] = [ECLT + ECHT] \quad (5.3)$$

where ECLT and ECHT are the low and high temperature elemental carbons, respectively.

Soil mass concentration is estimated by summing the elements predominantly associated with soil, plus oxygen for the normal oxides (Al₂O₃, SiO₂, CaO, K₂O, FeO, Fe₂O₃, TiO₂), plus a correction for other compounds such as MgO, Na₂O, water, and carbonate. The final equation for fine soil is:

$$[SOIL] = 2.20[Al] + 2.49[Si] + 1.63[Ca] + 2.42[Fe] + 1.94[Ti]. \quad (5.4)$$

Components of these factors were confirmed in comparisons of local resuspended soils and ambient aerosols in the western United States [Cahill *et al.*, 1981; Pitchford *et al.*, 1981].

Coarse mass (CM) is estimated gravimetrically by subtracting fine mass (PM_{2.5}) from total aerosol mass (PM₁₀):

$$[CM] = [PM_{10}] - [PM_{2.5}]. \quad (5.5)$$

In the IMPROVE program, additional chemical analysis is not carried out on the coarse fraction. However, it is known that in rural or remote areas of the country the primary constituent of

coarse mass is naturally occurring wind-blown dust along with some vegetative material [Noll *et al.*, 1985; Noll, 1991].

The sum of the above five composites should provide a reasonable estimate of the fine mass measured on the Teflon filter. However, a significant fraction of the nitrate particles can volatilize from the Teflon filter during collection and is not measured by gravimetric analysis. Therefore, nitrate is not included in reconstructed fine mass (RCFM) when comparing RCFM to the gravimetric mass derived from the Teflon filter. The equation for RCFM is therefore:

$$[RCFM] = [SULFATE] + [LAC] + [OMC] + [SOIL]. \quad (5.6)$$

The self-consistency and overall quality of the aerosol measurements are assured by redundancy and intercomparisons between independently measured species. A detailed description of validation and quality assurance procedures is available in Malm *et al.* [1994], Sisler *et al.* [1993], and Eldred *et al.* [1988]. In the most general sense, validation is a matter of comparing chemically related species that have been measured in different channels.

5.2 SUMMARY OF AEROSOL MEASUREMENTS

Table 5.1 contains statistical summaries of the aerosol mass concentrations along with the fraction that each aerosol species contributes to reconstructed fine mass, while Figure 5.1 is a scatter plot of reconstructed and measured fine mass. Although water associated with hygroscopic aerosols was not explicitly measured, it is expected that a significant amount of water was retained on the filter when the filters were weighed. The filters were equilibrated in the laboratory at approximately 43% relative humidity, a value that is well above the relative humidity at which ammonium sulfate or other hygroscopic particles dry out [Tang *et al.* 1981]. Therefore, retained water will cause scatter in the data points below, but not above, the 1:1 line because measured gravimetric mass includes some water, while reconstructed mass does not. Figure 5.1 clearly shows this trend.

The amount of water mass associated with the sulfate species can be estimated from the Tang *et al.* [1981] published results for sulfate species growth as a function of relative humidity. Because the acidity of the sulfate aerosol was variable over the study period a D/D_o growth curve, for each sampling period based on the measured NH_4/SO_4 ratio, was estimated following an interpolation scheme outlined in Section 5.4.1. The amount of water mass associated with each sample was calculated using:

$$[water] = [sulfate\ species] \frac{(D/D_o)^3 - 1}{\rho_x / \rho_w} \quad (5.7)$$

where water and sulfate species refer to the respective masses, D/D_o is the sulfate species growth at laboratory relative humidity, and ρ_s and ρ_w are the sulfate species and water densities. The average water retained on the filters that is associated with sulfate is estimated to be about $6 \mu\text{g m}^{-3}$, which is more mass than any other species except sulfates. The combined mass of sulfates and its associated water is about $17 \mu\text{g m}^{-3}$. The next closest mass concentrations are organics at $4.6 \mu\text{g m}^{-3}$.

Table 5.1 Statistical summary of aerosol species concentrations and the fraction of reconstructed fine mass attributed to certain species. Units are in $\mu\text{g m}^{-3}$. Measured fine mass (FM) is 1.38 times greater than reconstructed fine mass.

Variable	Mean	Std. Dev.	Minimum	Maximum	Fraction	Valid
OFM	25.1270	17.5495	0.0000	87.9412	1.38	80
RECON	18.0936	12.3359	3.6565	59.4061	---	80
SO ₄	9.5507	9.0158	1.0862	42.7037	---	80
SULMASS	11.4183	10.3234	1.1654	48.2328	0.63	80
Water	5.8920	6.9990	10.860	42.7040	---	80
NITRATE	0.2007	0.1071	0.0690	0.7005	0.01	80
O1	0.3083	0.3263	-0.1390	1.4458	---	80
O2	0.2748	0.3201	-0.4576	1.2546	---	80
O3	0.4157	0.2404	0.0000	1.3255	---	80
O4	0.4816	0.3880	0.0000	1.7144	---	80
OP	0.7754	0.4731	0.0000	2.2676	---	80
OCLT	0.3083	0.3263	-0.1390	1.4458	---	80
OCHT	1.9475	1.0741	0.0000	4.4530	---	80
OMC	4.5581	1.7968	1.4000	8.6050	0.25	80
E1	0.1610	0.1564	0.0000	0.6242	---	80
E2	0.2363	0.1528	0.0000	0.7884	---	80
E3	0.0448	0.0397	-0.0211	0.1578	---	80
LAC	0.4421	0.2493	0.0000	1.1722	0.02	80
SOIL	1.4743	1.5582	0.0174	8.3334	0.08	80
CM	6.1551	5.8480	0.0000	24.6874	---	80
NH ₄	1.7905	1.2968	0.0607	4.9780	---	80
NH ₄ ⁺ /SO ₄	1.1000	0.3030	0.2980	1.8470	---	80

Figure 5.2, like Figure 5.1, is a scatter plot of reconstructed and measure fine mass, only in this case reconstructed mass includes an estimate of the amount of water retained on the filters at the time of the gravimetric analysis. The average humidity during the analysis was about 45%. Also plotted for reference in Figure 5.2 is the 1:1 line. When the estimate of the amount of water retained by sulfate particles is included in the reconstructed mass estimates it can be seen that within the uncertainty of the estimate and measurements in most cases all the mass is accounted for.

Figure 5.3 shows temporal plots of measured fine mass and the five major aerosol species. The lowest concentrations of fine mass occurred on JD 216 when values of 3-4 $\mu\text{g m}^{-3}$ were recorded. Conversely, on JD 230 measured fine mass was 88 $\mu\text{g m}^{-3}$. The temporal history of the fraction that each species contributes to reconstructed fine mass without water added is presented in Figure 5.4. From Figure 5.4, it can be seen that the major constituent during the JD 230 episode was sulfates. Additionally, the first graph in Figure 5.4 shows the ratio of measured to reconstructed fine mass. It can be seen that for much of the time the sulfate contribution to reconstructed fine mass was over 70% and on the days with the lowest fine mass concentrations the sulfate fraction of fine mass was the lowest.

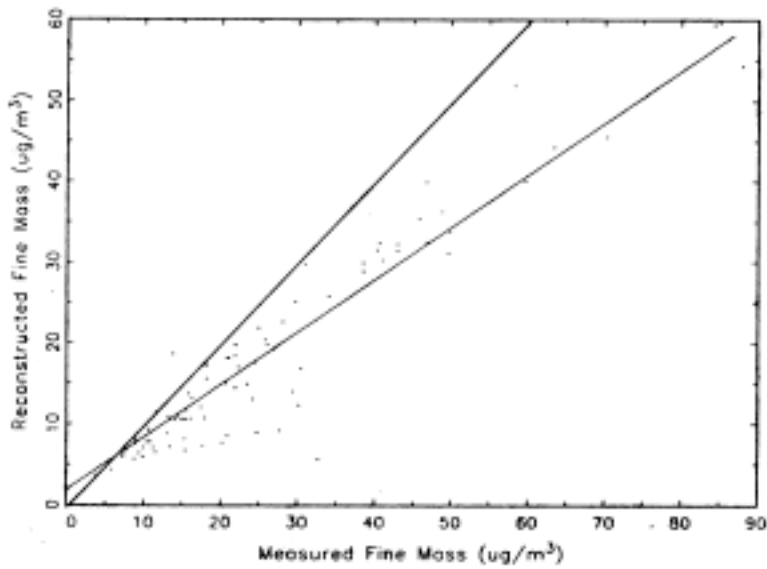


Figure 5.1 Scatter plot of reconstructed and measured fine mass. Also plotted are the 1:1 line and the ordinary least square regression line.

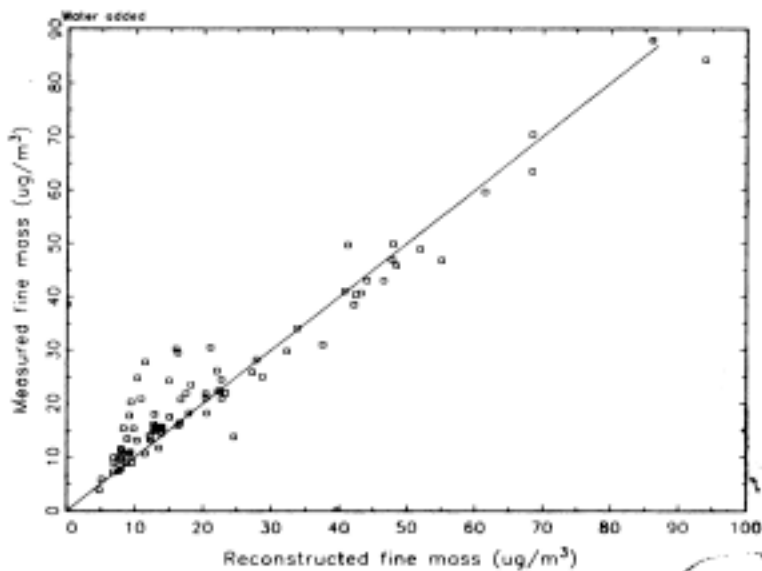


Figure 5.2 Scatter plot of reconstructed and measured fine mass when the amount of water retained on the filter during gravimetric analysis is included in the reconstructed estimate. Also plotted is the 1:1 line.

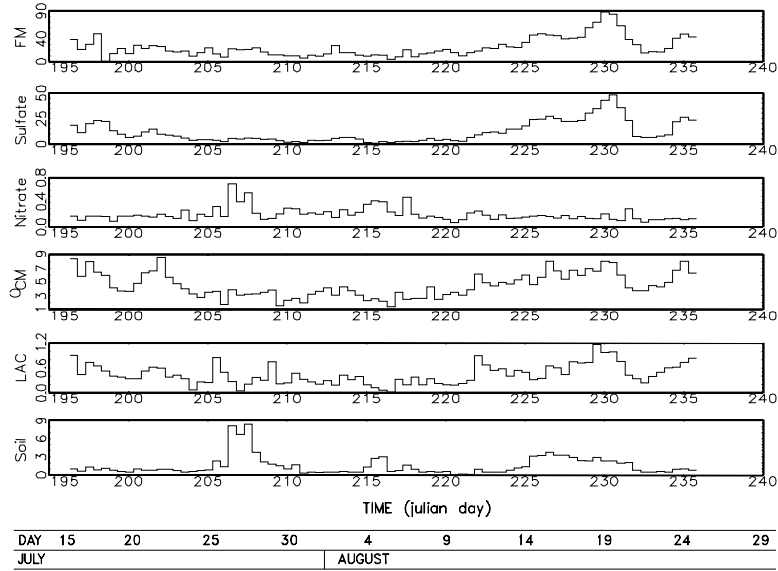


Figure 5.3 Time lines of fine mass (FM), sulfate species (SULFATE), ammonium nitrate (NITRATE), organic mass (OCM), elemental carbon (LAC), and soil (SOIL). The time line is presented in Julian day, while concentrations are in $\mu\text{g m}^{-3}$.

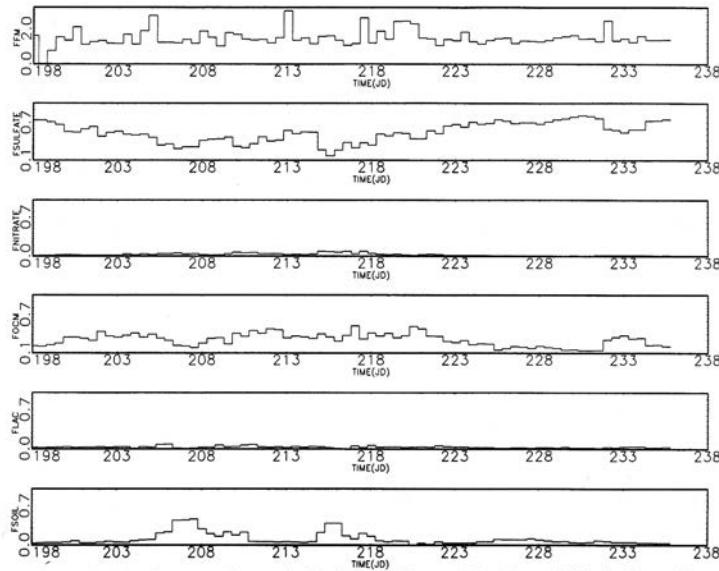


Figure 5.4 Time lines of reconstructed fine mass fraction of measured fine mass (FFM), sulfate species fraction of measured mass (FSULFATE), ammonium nitrate fraction of reconstructed mass (FNITRATE), organic mass fraction of reconstructed mass (FOCM), elemental carbon fraction of reconstructed mass (FLAC), and soil fraction of reconstructed mass (FSOIL). The time lines are presented in Julian day.

Interestingly, the fraction of fine mass attributed to organics is fairly constant at about 20-30% over the whole sampling period except for the high sulfate episode where it is near 10%. Three relatively high soil episodes were recorded on JD 206-207, JD 215-216, and JD 225-232.

On JD 207 soil was about 40-50% of the fine mass. Elemental carbon (LAC) and nitrate contribution to fine mass was small during the entire study period.

On the average, measured fine mass accounts for about 80% measured PM10 mass. Sulfates are the largest fraction of reconstructed fine mass at 63%. Organic carbon accounts for 25% of the fine mass, while soil contributes another 8%. Nitrates and LAC are virtually tied for the lowest contribution to fine mass at 1% and 2%. It is worth noting that the mass fractions reported here are consistent with those found at other eastern monitoring sites [Sisler, 1996].

The average molar ratio of ammonium to sulfate ion is 1.1 suggesting the sulfate is on average ammonium bisulfate.

5.3 COMPARISON OF OPTICAL VARIABLES

The total extinction coefficient, $b_{ext,t}$, is the sum:

$$\begin{aligned} b_{ext,t} &= b_{ext} + b_{ext,g}, \text{ where} \\ b_{ext} &= b_{scat} + b_{abs}, \text{ and} \\ b_{ext,g} &= b_{scat,g} + b_{abs,g}. \end{aligned} \tag{5.8}$$

b_{ext} and $b_{ext,g}$ are the extinctions due to particles and gases, respectively. b_{ext} is the sum of scattering, b_{scat} , and absorption, b_{abs} , by particles, while $b_{ext,g}$ is the sum of scattering, $b_{scat,g}$, and absorption, $b_{abs,g}$, by gases. All terms are wavelength dependent. Light scattering by gases in the atmosphere is described by the Rayleigh scattering theory [vandeHulst, 1981] and will be referred to as Rayleigh scattering. The only gas that is normally found in the atmosphere and absorbs light is nitrogen dioxide. In most instances, particle scattering and absorption are primarily responsible for visibility reduction [Trijonis and Pitchford, 1987].

In many early visibility studies, comparisons were made between scattering as measured by nephelometry and the various aerosol species to derive or validate scattering budgets, while extinction was estimated by summing absorption and scattering [Appel *et al.*, 1985; Ouimette *et al.*, 1981; Groblicki *et al.*, 1981; Macias *et al.*, 1981]. In many of these early studies, the nephelometer sampling chamber was warmer than ambient temperatures and therefore underestimated scattering due to absorbed water at higher relative humidities. At 90% relative humidity (RH), a 1°C difference between ambient and sampling chamber temperature will cause the sampling chamber relative humidity to reduce to about 84% RH, while a 4°C temperature difference translates into a chamber RH of 70%.

More recent studies, carried out in urban environments, included estimates of extinction from teleradiometer techniques but utilized nephelometers, which heated the aerosol by about 4°C [Dzubay and Clubb, 1981; Dzubay *et al.*, 1982; Lewis and Dzubay, 1986].

The most recent urban studies at Denver, Phoenix/Tucson, and Tucson [Watson *et al.* 1988, 1989; Heisler *et al.*, 1980a,b; Watson *et al.* 1990a,b; Heisler *et al.* 1994] employed transmissometers to measure extinction [Dietrich *et al.*, 1989], ambient nephelometers to

measure scattering [Malm *et al.*, 1994], and integrating plate transmission measurements for absorption [Watson *et al.*, 1988, 1989]. These studies also included a full suite of aerosol measurements. For the most part, the sum of absorption and scattering equaled measured extinction within measurement uncertainty and measured absorption and scattering could be predicted from aerosol measurements.

Only two studies have explored the relationship between ambient measurements of extinction, scattering, and absorption in nonurban settings [White *et al.*, 1994 and Malm *et al.*, 1996]. They were able to show that the scattering and absorption, as measured by optical techniques, and the fraction of coarse mass scattering not captured by the nephelometer summed to equal measured extinction and were consistent with measurements of fine and coarse mass. White *et al.* [1994] did not explore the relationship between measured absorption and estimates of absorption from aerosol concentrations, while Malm *et al.* [1996] compared absorption estimates made by LIPM and measured EC. They concluded that b_{abs} as estimated using the LIPM was a more accurate estimate of absorption than estimates from EC.

In SEAVS, absorption was measured or estimated four different ways. One aspect of this study focused on determining which of the four estimates of absorption best represent ambient absorbing characteristics of the atmosphere. Independent measurements of extinction, scattering, and absorption allow for internal consistency checks on the optical measurements in that absorption and scattering should sum to extinction. Furthermore, the sum of aerosol scattering should equal measured scattering, and absorption estimated from measured aerosol species should equal measured absorption.

5.3.1 Estimating Aerosol Absorption

On channel A, b_{abs} is quantified directly by the LIPM analysis and it can also be estimated from the aethalometer measurements. The aethalometer is an absorption measurement calibrated to read out in black carbon (BC) concentrations. The calibration constant assumed in this report is $20 \text{ m}^2 \text{ g}^{-1}$. Therefore, $b_{abs,a}$ is estimated from the aethalometer measurements using:

$$b_{abs,a} = 20(BC) \quad (5.9)$$

where $b_{abs,a}$ is the estimated aethalometer absorption and BC is the black carbon number reported by the aethalometer instrument.

It can also be estimated using:

$$b_{lac} = \alpha_{abs}[EC] \quad (5.10)$$

where α_{abs} is the absorption efficiency of elemental carbon. b_{lac} is used to represent particle absorption estimates derived from EC mass concentrations. Horvath [1993] reviewed a number of studies where α_{abs} for soot and black carbon were measured. He also reviewed a number of theoretical calculations of α_{abs} where a variety of refractive indices and densities were assumed. Measured values of α_{abs} range from a low of 3.8 to a high of $17 \text{ m}^2 \text{ g}^{-1}$, while theoretical

calculations of α_{abs} suggest a value of 8-12 m² g⁻¹. The relationship between b_{abs} , $b_{abs,a}$, and b_{lac} will be further explored in the following comparisons.

5.3.2 Comparison of Absorption Estimates

Figure 5.5 shows a temporal plot of b_{scat} (<2.5 μm), and b_{ext} with the inset showing a temporal plot of the same variables but for only a subset of the data. The dotted and solid lines correspond to the extinction and scattering data, respectively. The data gaps correspond to time periods when the transmissometer was being calibrated. The inset shows, in some detail, the typical differences between the two variables. During the evening hours, extinction and scattering were nearly the same but with extinction being slightly greater than scattering. However, during daylight hours, the difference between the two variables was the greatest. In the inset, extinction is about 20% greater than scattering. The differences between the transmissometer measured extinction and nephelometer measured scattering could be due to differences in aerosol mix in that the transmissometer measurement was over a slant path, while the nephelometer was made at one point, differences in RH, and contributions to extinction by coarse particle scattering and absorption. The RH differences could be significant, however, the nephelometers were held at near ambient conditions. On the other hand, given the elevation differences between the transmissometer transmitter and receiver, it is quite possible that the RH varied over the measurement path.

Table 5.2 is a statistical summary of b_{ext} , b_{scat} , b_{abs} , $b_{abs,a}$ and b_{lac} . The difference between average b_{ext} and b_{scat} is approximately 0.04 km⁻¹. Figure 5.6 is a scatter plot of b_{ext} and b_{scat} along with the 1:1 and the ordinary least squares (OLS) regression line. Table 5.3 is a summary of the regressions carried out between various variables. The regression coefficient suggests that b_{ext} is about 10% greater than scattering suggesting b_{ext} is about, on the average 0.02 km⁻¹ greater than scattering. On the other hand, average extinction is about 20% greater than average scattering (see Table 5.2). These numbers set an upper limit on the amount of fine particle absorption in the atmosphere. Absorption plus coarse mass scattering and absorption plus differences in relative humidity effects should not exceed, on the average, 0.02-0.04 km⁻¹.

Table 5.2 *Statistical summary of measured extinction, scattering, and absorption. Absorption was estimated from LIPM (b_{abs}), aethalometer ($b_{abs,a}$), and elemental carbon (b_{lac}).*

Variable	Mean	Std. Dev.	Minimum	Maximum	Valid
b_{ext}	0.246	0.139	0.059	0.737	38
b_{scat}	0.200	0.135	0.029	0.611	41
b_{abs}	0.014	0.010	0.000	0.041	41
$b_{abs,a}$	0.007	0.004	0.001	0.014	41
b_{lac}	0.005	0.003	0.000	0.012	41

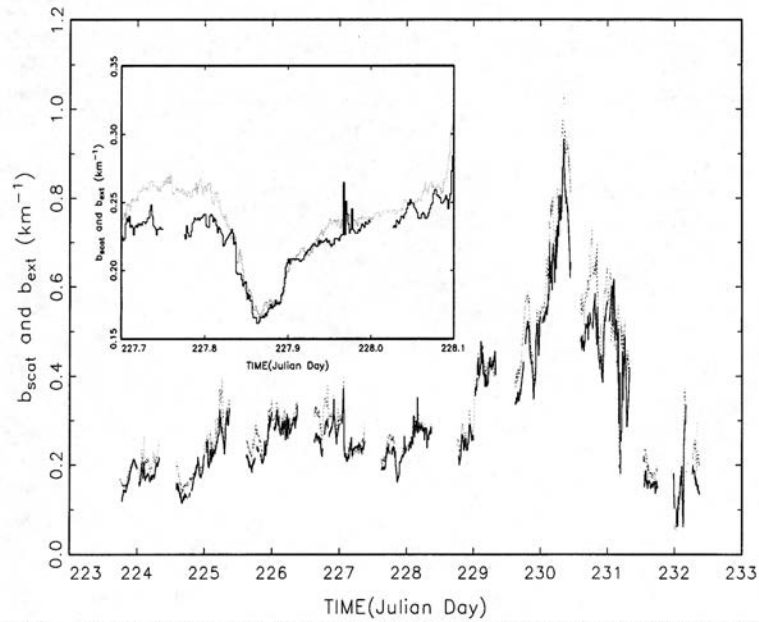


Figure 5.5 Time lines of measured scattering and extinction. The inset shows in "exploded" view the time lines for the time period JD 227.7-228.1. Time is in Julian day, while units on scattering and extinction are in km^{-1} .

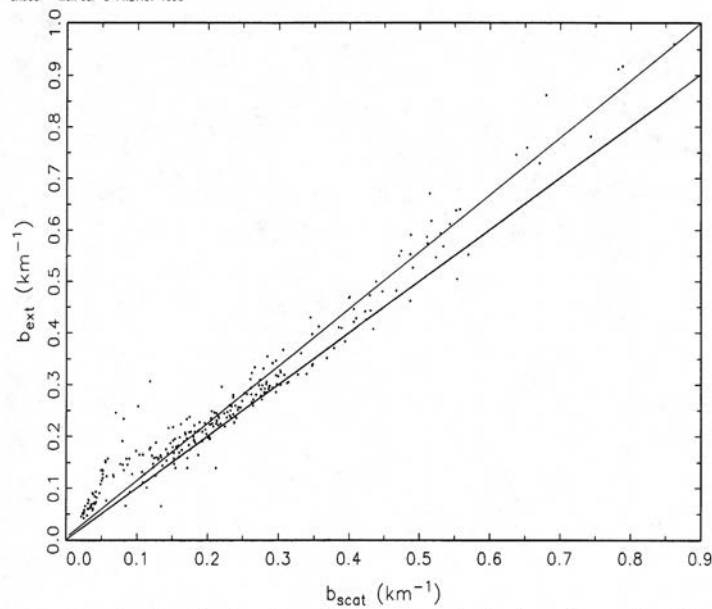


Figure 5.6 Scatter plot of b_{ext} and b_{scat} along with a 1:1 line and a line representing a best fit between the two variables. Units are in km^{-1} .

Table 5.3 Ordinary least square regressions with an intercept between variables presented in Figures 5.3, 5.5, 5.6, and 5.7.

Dep. Variable	Ind. Variable	Estimate	Std. Error	Prob>t	N	R ²
b_{ext}	Constant	0.000	int set = 0	---	274	0.94
	b_{scat}	1.104	0.009	0.000		
EC b_{lac}	Constant	0.002	0.000	0.000	78	0.57
	Filter b_{abs}	0.220	0.212	0.000		
EC b_{lac}	Constant	0.001	0.000	0.005	77	0.60
	Aeth b_{abs}	0.508	0.048	0.000		
Aeth b_{abs}	Constant	0.002	0.000	0.000	79	0.75
	Filter b_{abs}	0.382	0.025	0.000		
Recon b_{ext}	Constant	-0.022	0.017	0.202	36	0.89
	Meas b_{ext}	0.995	0.059	0.000		

Figure 5.7 shows a temporal plot of b_{abs} , $b_{abs,a}$, and b_{lac} , while Table 5.2 is a statistical summary of these variables. Referring to Table 5.2, of the three absorption estimates, b_{abs} (LIPM) is the largest at 0.014 km^{-1} , $b_{abs,a}$ (aethalometer) is the second highest at 0.007 km^{-1} , and b_{lac} (elemental carbon) at 0.005 km^{-1} is the lowest. b_{abs} is about a factor of 2 greater than $b_{abs,a}$ and a factor of 2.8 greater than b_{lac} . Figure 5.7 shows that all estimations of absorption capture the major temporal trends, with the aethalometer and LIPM absorption being more highly correlated with each other than with EC absorption.

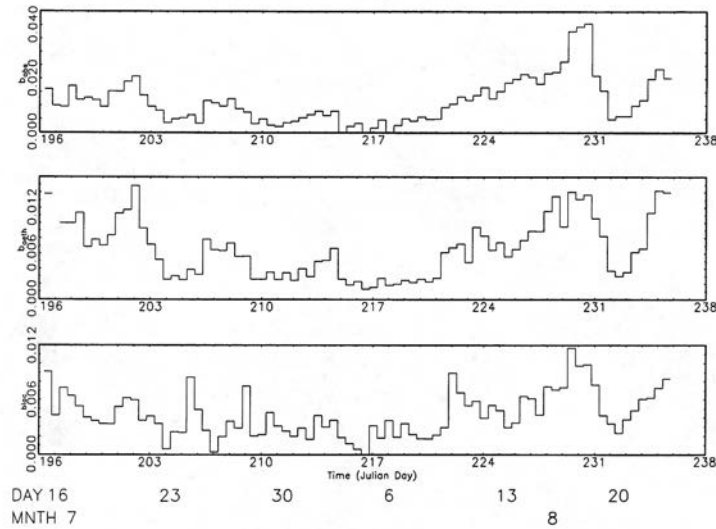


Figure 5.7 Time lines of three measurement techniques for estimating absorption. The first time line is absorption estimated by the laser integrated plate technique, b_{abs} , the second is from an aethalometer measurement, b_{aeth} , and the third is an estimate from measured elemental carbon, b_{lac} . Units are in km^{-1} .

The intercomparison of these variables is further examined in a series of scatter plots that compare these variables to each other. Figure 5.8 is a scatter plot of b_{lac} versus b_{abs} along with the 1:1 and OLS regression lines, while Figure 5.9 shows the comparison of b_{lac} and $b_{abs,a}$. Results of the scatter plot regressions are presented in Table 5.3. The R^2 for each of these plots are 0.57 and 0.60, respectively. The R^2 for the scatter plot between $b_{abs,a}$ and b_{abs} , which is shown in Figure 5.10, is 0.75. It is interesting to note that as absorption increased the difference between the two variables substantially increased.

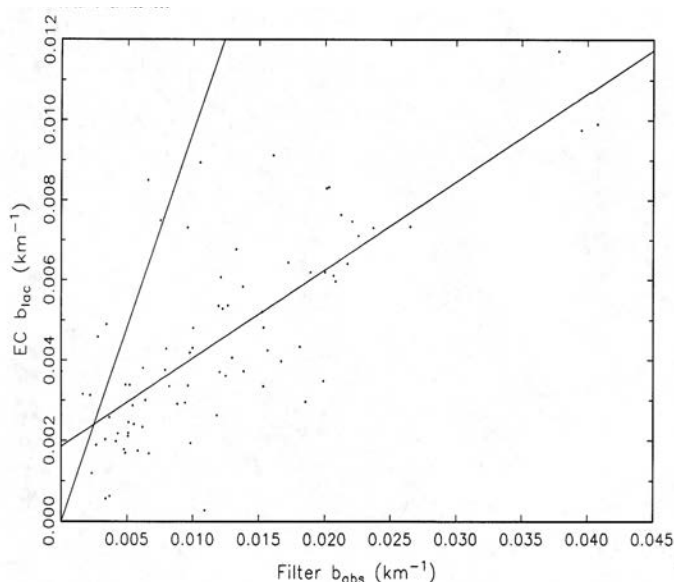


Figure 5.8 Scatter plot of elemental carbon, EC, (elemental carbon, LAC, and elemental carbon, EC, have been used interchangeably) and b_{abs} by LIPM. The 1:1 and ordinary least square lines are shown for reference.

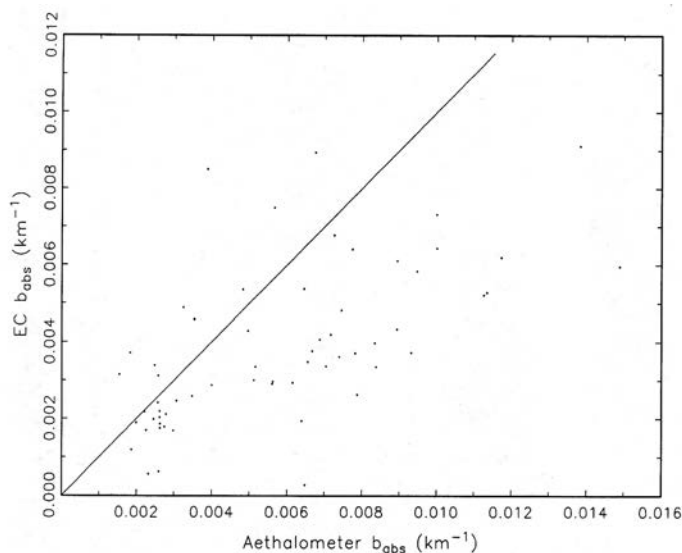


Figure 5.9 Scatter plot of elemental carbon, EC, (elemental carbon, LAC, and elemental carbon, EC, have been used interchangeably) and b_{aeth} from the aethalometer. The 1:1 and ordinary least square lines are shown for reference.

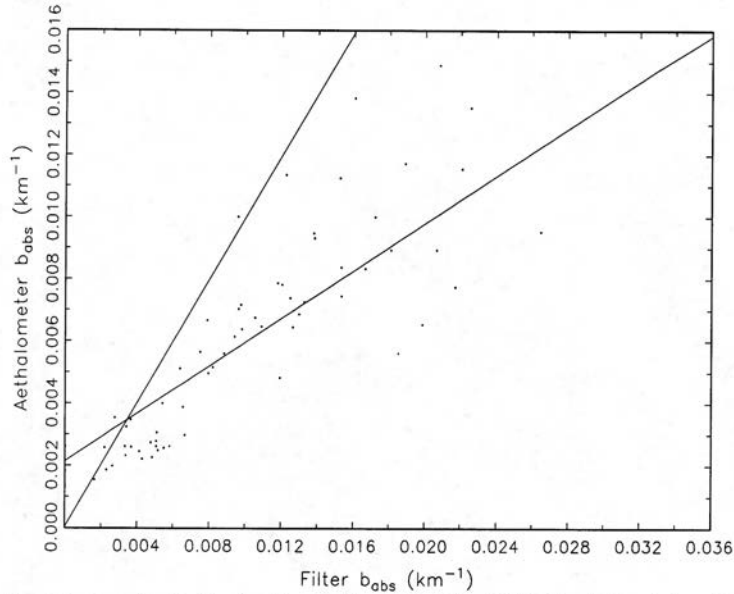


Figure 5.10 Scatter plot of b_{aeth} from the aethalometer and b_{abs} as estimated from LIPM. The 1:1 and ordinary least square lines are shown for reference. Units are in km^{-1} .

5.3.3 Comparison of Reconstructed Extinction From Scattering and Absorption

The SEAVS data set offers a unique opportunity to examine the relationship between extinction, scattering, and absorption directly without having to unduly rely on estimates of aerosol scattering from various species. Extinction, scattering, and absorption are all measured optically and thus allow for an independent assessment of the accuracy of these measurements. If the validity of these measurements can be established then scattering and absorption, as estimated from aerosol measurements, can be independently compared to each of these measures.

Extinction and scattering measurements are directly compared by using the following equation:

$$b_{ext} = b_{scat} + b_{abs} + CMS \quad (5.11)$$

where b_{scat} is the scattering measured by the nephelometer with the 2.5 μm inlet and CMS is the estimated total coarse mass scattering. b_{abs} is the absorption as estimated by LIPM, aethalometer, or from EC.

Equation (5.11) consists of all measured optical variables except for CMS. Figure 5.11 is a scatter plot of the left and right side of Equation (5.11). The upper, middle, and lower tick marks on the scatter plot data points correspond to using b_{abs} , $b_{abs,a}$, and b_{lac} , respectively. The R^2 of the OLS regression line is 0.89, while the regression coefficient is 0.995 indicating that measured

extinction is well represented by the sum of scattering and absorption. Because absorption is on the order of 5% or less of total extinction the comparison between reconstructed to measured extinction does not conclusively point to one measure or the other as being the best measure of absorption. However, from Figure 5.11 it can be seen that during the highest extinction periods the comparison between reconstructed and measured extinction is better when using b_{abs} (LIPM) than the other absorption estimates. In a special study in the Southwest during the summer months when relative humidity was low and the absorption contribution to extinction was greater, the use of b_{abs} (LIPM) in Equation (5.11) yielded a reconstructed extinction that was within 1% of measured extinction, while the use of b_{lac} yielded a reconstructed extinction that was about 25% less than measured extinction [Malm *et al.* 1996]. It was concluded in that analysis that using b_{abs} without any adjustments for reconstituting extinction gives a reasonable fit to measured extinction suggesting that b_{ext} , b_{scat} , and b_{abs} are accurate representations of ambient extinction, scattering, and absorption, while b_{lac} is not. In this study, the average b_{lac} and $b_{abs,a}$ values are similar and, as in other studies, b_{lac} is significantly less than b_{abs} suggesting that $b_{abs,a}$ may also be an underestimate of absorption.

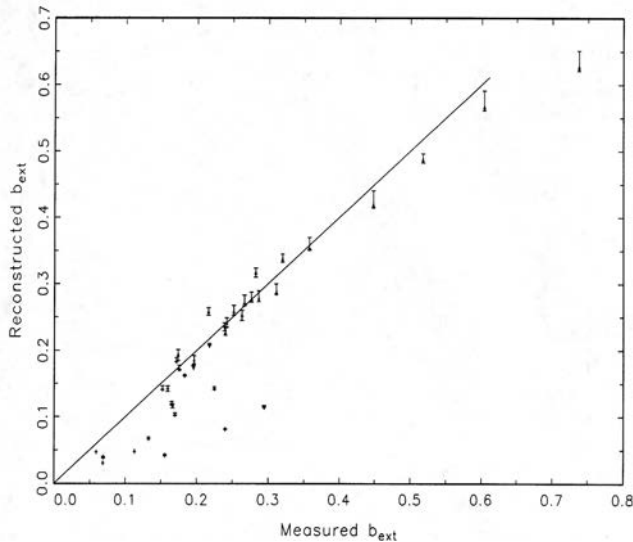


Figure 5.11 Scatter plot of measured and reconstructed extinction where reconstructed extinction is the sum of b_{scat} and a measure of absorption. Each data point corresponds to the range of reconstructed extinction corresponding to b_{lac} , b_{aeth} , and b_{abs} . b_{lac} corresponds to the lowest reconstruction, b_{aeth} the middle, and b_{abs} the highest. Units are in km^{-1} .

5.3.4 Absorption Characteristics of Carbon Species

Table 5.1 presents simple statistical summaries of the various carbon categories. OMC is typically assumed to scatter but not absorb light, while EC is assumed to absorb but not scatter. Figure 5.12 shows scatter plots of b_{abs} and four carbon variables. (OCLT=O1, OCHT=O2+O3+O4+OP, ECLT=E1+E2, and ECHT=E3). Because b_{abs} is an independent optical measurement it is expected that it can be estimated from elemental carbon species as follows:

$$b_{abs} = \sum_i \alpha_i m_i \quad (5.12)$$

where α_i is the extinction mixture. One would expect a high degree of correlation between b_{abs} and the two high temperature carbon species, and possibly very little correlation between b_{abs} and the OCHT and OCLT fractions. However, a cursory look at Figure 5.12 shows that this is not the case. b_{abs} is correlated with OCHT as well as with ECLT and better than with ECHT. Similar relationships are found at all IMPROVE monitoring sites, in a southwestern special study [Malm *et al.* 1996] and also in a special study in the Pacific Northwest [Malm *et al.* 1994].

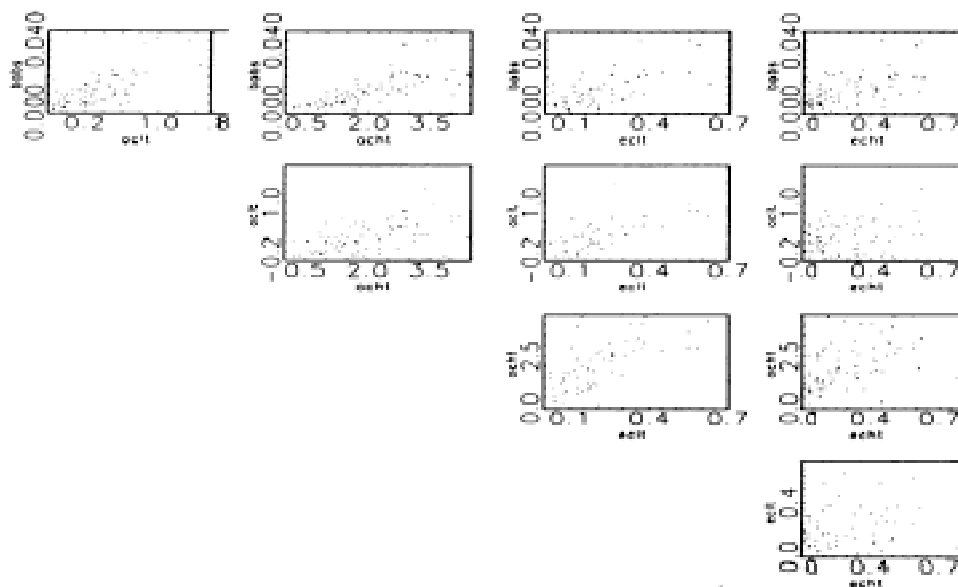


Figure 5.12 Multiple scatter plot of b_{abs} , OCLT, OCHT, ECLT, and ECHT. Units are in km^{-1} .

The relationship between these variables suggests that elemental carbon is not only associated just with EC, but also with OCHT or that EC and OCHT originate from the same source. These hypotheses can be further explored by examining the quantitative relationships between b_{abs} , EC, and OMC. If EC was the only variable associated with light absorption, then the ratio b_{abs}/EC , the absorption efficiency of EC, should be between 8 and $12 \text{ m}^2 \text{ g}^{-1}$ [Sloane, 1984; Horvath, 1993]. For this study $b_{abs}/\text{EC} = 30 \text{ m}^2 \text{ g}^{-1}$ and $b_{abs,a}/\text{EC} = 14 \text{ m}^2 \text{ g}^{-1}$ for the LIPM and aethalometer measurement, respectively.

The general inflation of b_{abs}/EC ratios suggests that there is also some light absorption associated with the low temperature carbon species. The amount of absorption that potentially can be attributed to OCHT can be estimated by assuming an 8 - $12 \text{ m}^2 \text{ g}^{-1}$ absorption efficiency for EC and assigning the difference between measured b_{abs} and EC absorption to organic carbon. The fraction of absorption attributed to OCHT or other absorbing material such as soil is approximately 65% using b_{abs} and 30% using $b_{abs,a}$.

The traditional assumption is that the division of carbon into OMC and EC coincides with the division between elemental and nonlight-absorbing carbon [Chow *et al.*, 1993]. However, if b_{abs} by LIPM or aethalometer are the more accurate measures of absorption, then the present analysis suggests that the assignment of elemental carbon to only EC is inappropriate. Apparently, some OMC may also absorb light. Huffman [1996a,b] and Malm *et al.* [1996] have explored this

question by looking at relationships between b_{abs} and the various carbon "peaks": O1, O2, O3, O4, OP, E1, E2, and E3. A similar analysis will be presented here. Ordinary least square (OLS) regressions were carried out with b_{abs} and $b_{abs,a}$ as the dependent variable and soil and the carbon "species" as independent variables. The initial exploration involved using each of the carbon species separately as independent variables and then adding combinations in an effort to increase the overall model fit and reduce colinearity effects. The best model, as judged by R^2 values and significant levels of regression coefficients, was with E1+E2, O4+OP, and soil. Also, statistically significant relationships with O1 through O3 were not found. A summary of the variables used in the regression are presented in Table 5.4, while the results of the regression analysis are presented in Table 5.5.

Table 5.4 Statistical summary of b_{abs} , $b_{abs,a}$, elemental carbon (E1+E2+E3), O4+OP, and soil.

Variable	Mean	Std. Dev.	Minimum	Maximum	Valid
b_{abs} (km^{-1})	0.018	0.009	0.000	0.041	80
$b_{abs,a}$ (km^{-1})	0.007	0.004	0.001	0.015	79
E1+E2+E3 (ng m^{-3})	0.442	0.249	0.000	3.134	80
O4+OP (ng m^{-3})	1.257	0.711	0.000	3.134	80
Soil (ng m^{-3})	1.474	1.558	0.017	8.333	80

The implied absorption efficiencies for E1+E2+E3, O4+OP, and soil are 15.1, 5.1, and 1.3 $\text{m}^2 \text{g}^{-1}$, respectively, with an intercept term of -3.3 Mm^{-1} . Forcing the regression through zero resulted in coefficients of 12.4, 4.3, and 0.9 $\text{m}^2 \text{g}^{-1}$. A scatter plot of measured and reconstructed b_{abs} is shown in Figure 5.13 for the model with the intercept term. A negative intercept does not have a physical interpretation; therefore, the apportionment of absorption was made only between the independent variables. E1+E2+E3 accounted for 44%, O4+OP for 43%, and, soil accounted for 13%.

Table 5.5 Summary of ordinary least square (OLS) regressions using b_{abs} and $b_{abs,a}$ as dependent variables and O4+OP, E1+E2+E3, and soil as independent variables.

Dep. Variable	Ind. Variable	Estimate	Std. Error	Prob>t	N	R^2	Fraction
b_{abs}	Constant	-0.003	0.001	0.007	77	0.72	
	O4+OP	0.005	0.001	0.000			0.43
	E1+E2+E3	0.015	0.003	0.000			0.44
	Soil	0.001	0.000	0.000			0.13
b_{abs}	O4+OP	0.004	0.001	0.000	77	0.69	
	E1+E2+E3	0.012	0.003	0.000			
	Soil	0.001	0.000	0.004			
$b_{abs,a}$	Constant	-0.000	0.001	0.732	79	0.80	
	O4+OP	0.003	0.001	0.000			0.62
	E1+E2+E3	0.005	0.001	0.000			0.31
	Soil	0.000	0.000	0.000			0.07
$b_{abs,a}$	O4+OP	0.003	0.000	0.000	79	0.80	
	E1+E2+E3	0.005	0.001	0.000			
	Soil	0.000	0.000	0.004			

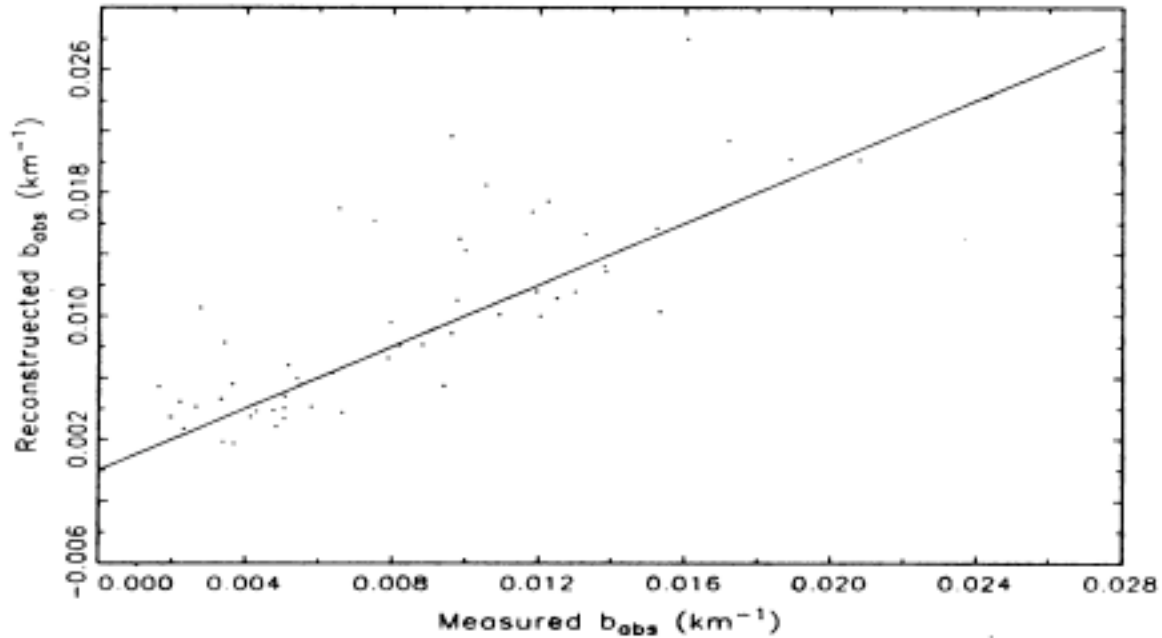


Figure 5.13 Scatter plot of reconstructed and LIPM measured b_{abs} along with the 1:1 line.

The same analysis was carried out using $b_{abs,a}$ (aethalometer) and is also shown in Table 5.5. The R^2 's are higher, however, because $b_{abs,a}$ is about a factor of two smaller than b_{abs} the regression coefficients and therefore the implied absorption efficiencies are about a factor of two smaller. The absorption efficiencies for the intercept regression are 4.6, 3.3, and 0.4 $\text{m}^2 \text{g}^{-1}$ for E1+E2+E3, O4+OP, and soil, respectively and 4.6, 3.3, and 0.34 $\text{m}^2 \text{g}^{-1}$ for the intercept equal to zero regression. Apportioning absorption between the regression variables yields 62%, 31%, 7% for E1+E2+E3, O4+OP, and soil, respectively. Whether the apportionment is carried out with b_{abs} or $b_{abs,a}$ a significant fraction of the absorption is attributed to O4+OP.

Because OLS regressions do not account for the inherent uncertainty in both dependent and independent variables, some caution should be used when interpreting the regression coefficients as having physical significance. Orthogonal departure type regressions could be carried out, however, when the uncertainties of the variables are not well established, as is the case for carbon measurements especially in the area of positive or negative artifacts, these types of regressions can give spurious results. Therefore, orthogonal departure regressions were not implemented. There are, however, some general trends that emerge from the regressions:

- 1) Soil contributes a significant amount to absorption.
- 2) For the b_{abs} regressions, the range of coefficients corresponding to elemental carbon (E1+E2+E3) is between 12 and 15 $\text{m}^2 \text{g}^{-1}$, which is within the range of absorption efficiencies assigned to elemental carbon, however, the efficiencies for the $b_{abs,a}$ model is 4.6 $\text{m}^2 \text{g}^{-1}$, which is lower than efficiencies typically assigned to elemental carbon.
- 3) O4+OP is clearly linked to absorption and the implied efficiencies are in the range of 4-5 $\text{m}^2 \text{g}^{-1}$ and 3.3 $\text{m}^2 \text{g}^{-1}$ for the b_{abs} and $b_{abs,a}$ models.

A number of interpretations, regarding the composition of the carbon aerosols, have been made by Malm *et al.* [1996]. The results for the b_{abs} data set are consistent with those interpretations. Because E1+E2+E3 has high absorption efficiency it is likely to be mostly elemental carbon. However, the O4 and pyrolyzed carbon, OP, have a lower efficiency. As such a number of hypotheses emerge as to its composition:

- 1) A fraction of O4 and OP could be elemental with a $10+ \text{ m}^2 \text{ g}^{-1}$ efficiency and the remaining fraction nonabsorbing organic carbon.
- 2) All O4 and OP is elemental carbon with about a $6 \text{ m}^2 \text{ g}^{-1}$ absorption efficiency and a commensurate scattering efficiency. This would imply that carbon particles are in the 0.2-0.6 μm size range.
- 3) O4 and OP are complex organic aerosols such as wood smoke that both scatters and absorbs light.

Huffman [1996a,b] essentially adopted hypothesis 1, which requires that a fraction of O4 and OP to absorb at approximately $10 \text{ m}^2 \text{ g}^{-1}$. If carbon is to absorb at $10 \text{ m}^2 \text{ g}^{-1}$ or greater it must be less than about 0.1 μm and will thus have a negligible scattering efficiency. However, to reconstruct scattering it was necessary to assume a scattering efficiency of $4 \text{ m}^2 \text{ g}^{-1}$ for O4 and OP. An O4+OP scattering efficiency of $4 \text{ m}^2 \text{ g}^{-1}$ is inconsistent with hypothesis 1.

It was expected that additional insight into the composition of the carbon species could be achieved by examining the relationships between nonsulfate hydrogen and the carbon species. OLS regressions were carried out using nonsulfate hydrogen, OH, as the dependent variable and the carbon species as independent variables. However, regressions for the data set reported on here did not yield significant regression coefficients.

This type of analysis did yield interesting insights when carried out on the IMPROVE data set. Special attention was given to determining the amount of hydrogen in the O4+OP regime. Neither E2 nor E3 loaded into the regression with significant coefficients supporting the notion that they are elemental carbon. Interestingly, the regression coefficient associated with O4+OP is the most significant variable and has the highest coefficient, which means that on a per mass basis it is the most hydrogen rich species. Using the regression coefficients to apportion hydrogen to the various species gave 46%, 47%, and 7% of the hydrogen to O1+O2+O3, O4+OP, and E1, respectively. The above analysis suggests that the O4+OP carbon model is a complex hydrogen rich organic aerosol that both scatters and absorbs light with a scattering efficiency of about $3\text{-}4 \text{ m}^2 \text{ g}^{-1}$ and an absorption efficiency of $4\text{-}5 \text{ m}^2 \text{ g}^{-1}$.

The interpretation of the composition of carbon would be slightly different if the $b_{abs,a}$ model is used. The conclusion that O4+OP model is a complex hydrogen rich organic absorbing aerosol is still true, however, the implied absorption efficiency is somewhat lower. On the other hand, the absorption efficiency associated with E1+E2+E3 is $3.3 \text{ m}^2 \text{ g}^{-1}$ and is a factor of almost 5 lower than with the b_{abs} model. Absorption efficiency this low is not consistent with efficiencies that are typically assigned to elemental carbon.

5.4 RECONSTRUCTED LIGHT SCATTERING

Any particle in the atmosphere, whether it is externally or internally mixed, scatters and/or absorbs a specific amount of radiant energy and as such has quantifiable mass extinction efficiency. Summing the extinction associated with each particle along some path must equal the total atmospheric extinction in that path. Therefore, a fraction of total extinction can be assigned to each particle type, and an extinction or scattering "budget" can be calculated.

Historically, researchers have invoked a number of assumptions concerning measured aerosol distributions. They have calculated or estimated specific mass scattering and absorption efficiencies, and used these to form estimates of extinction budgets. Because specific bulk aerosol species' concentrations are measured, the implicit assumption is one of externally mixed particles. However, under realistic assumptions concerning the microphysical properties of the particles the postulation of an external or internal mixture is not of over-riding importance to the estimation of specific mass extinction efficiencies. Ouimette and Flagan [1982] have shown that if an aerosol is mixed externally or if in an internally mixed aerosol the index of refraction is not a function of composition or size, and the aerosol density is independent of volume, then:

$$b_{ext} = \sum_i \alpha_i m_i \quad (5.13)$$

where α_i is the specific mass scattering or absorption efficiency and m_i is the mass of the individual species. It should be pointed out, however, that as water is absorbed by hygroscopic particles the index of refraction will change and that change will be dependent on the growth and mixture models that are assumed.

All routine aerosol monitoring programs and most special study visibility characterization programs were designed to measure aerosol species such as sulfates, nitrates, elements, and carbonaceous material [Heisler *et al.*, 1980a; Malm *et al.*, 1994; Tombach and Thurston, 1994; Watson *et al.*, 1990a; Macias *et al.*, 1981]. They were not designed to determine whether these species were internally or externally mixed. Therefore, b_{ext} is usually apportioned by assigning specific mass extinction efficiencies to each species and calculating the total extinction using Equation (5.13).

A number of investigators have taken advantage of the form of Equation (5.13) to construct a multilinear regression model with b_{ext} as the dependent variable and the measured aerosol mass concentrations of species i as the independent variables. The regression coefficients are then interpreted as specific extinction to mass efficiencies [White and Roberts, 1977; Cass 1979; Groblicki *et al.*, 1981]. The use of multivariate regression models to apportion mass concentrations to scattering and absorption requires that the model meet a number of limiting assumptions, and should be used with caution. White [1986] discusses some of the issues associated with this problem.

When computing total extinction, the microscopic structure of the aerosol (that is, the extent of internal or external mixing) is found to be relatively unimportant, so that the assumption of internally vs. externally mixed particles does not have much impact on the predicted results.

This insensitivity to total scattering/extinction has been demonstrated by a number of authors, including Hasan and Dzubay [1983], Sloane [1983], and, more recently, Pilinis *et al.* [1995] and McMurry *et al.* [1996].

The contribution of a particle composed of a single chemical species to the total light extinction for a particular aerosol is discussed in terms of its mass extinction efficiency, while the contribution of a mixed aerosol to extinction is presented in terms of specific mass extinction efficiency. The extinction efficiencies are defined as the total extinction for the aerosol type, divided by the total mass concentration. A fraction of total extinction can be assigned to each particle type (in the case of internally mixed aerosols) or each chemical species (in the case of externally mixed aerosols) and a scattering "budget" can be calculated.

Estimating the change in b_{ext} resulting from the removal (or addition) of a single species, on the other hand, is uniquely different than assigning a fraction of measured extinction to a chemical species or a mixture of species. The change in extinction resulting from a change in aerosol species concentration will be referred to as the species partial mass extinction (or scattering) efficiency, e_p :

$$e_p = (\partial b_{ext} / \partial C_i)_{c_{j,etc}} \quad (5.14)$$

where $c_{j,etc}$ refers to those variables that are held constant when the partial derivative is evaluated. The partial derivative, $\partial b_{ext} / \partial C_i$, is dependent on change in composition as well as on change in aerosol size as species are added or removed from an aerosol mix. For instance, McMurry *et al.* [1996] examined e_p as a function of whether sulfates could be reasonably expected to be formed by gas (low relative humidity leading to smaller sizes) or liquid phase (high relative humidity leading to larger sizes) transformation mechanisms.

A simple example illustrating some of these concepts is shown in Figure 5.14. The insensitivity of the total computed scattering to the mixing assumption is presented in Figure 5.14A. Two aerosol species, with the same size and with densities differing by a factor of 2, are assumed to be present as an external mixture, with each (g m^{-3} of mass concentration of species 1 and species 2 assumed to scatter 3 Mm^{-1} and 6 Mm^{-1} , respectively. This property may alternatively be expressed as mass scattering efficiencies of $3 \text{ m}^2 \text{ g}^{-1}$ and $6 \text{ m}^2 \text{ g}^{-1}$ for species 1 and 2. If the aerosol of interest contains $10 \mu\text{g m}^{-3}$ of species 1 and $5 \mu\text{g m}^{-3}$ of species 2, each species thus contributes 30 Mm^{-1} to the scattering, for a total aerosol scattering of 60 Mm^{-1} .

If the same amounts of species 1 and species 2 were present as an internal mixture (shown in the lower part of Figure 5.14A), the specific mass scattering efficiency for the mixed particle is now needed for calculation of the total aerosol scattering. This mixture mass scattering efficiency would be computed as the mass-weighted average of those for the individual species, or $4 \text{ m}^2 \text{ g}^{-1}$, if several conditions are met: the index of refraction of the mixture must be close to that for the individual species, which must also be similar (this condition is met, for example, by a mixture of ammonium sulfate and organics, with real refractive indices of 1.53 and 1.55, respectively); volume conservation must be invoked; and the total number of particles in a certain size range must remain similar to the case for the external mixture. Employing this mass

weighted average, specific mass scattering efficiency, the total aerosol scattering for the sample is again computed as 60 Mm^{-1} .





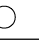
		Figure 1-A		Figure 1-B	
		species 1	species 2	species 1	species 2
mass	external case	$10 \mu\text{g m}^{-3}$	$5 \mu\text{g m}^{-3}$	$10 \mu\text{g m}^{-3}$	species 2 removed
aerosol type					
species density		2 g cm^{-3}	1 g cm^{-3}	2 g cm^{-3}	
mass scattering efficiency		$3 \text{ m}^2\text{g}^{-1}$	$6 \text{ m}^2\text{g}^{-1}$	$3 \text{ m}^2\text{g}^{-1}$	
particle scattering		30 Mm^{-1}	30 Mm^{-1}	30 Mm^{-1}	
total scattering		60 Mm^{-1}		30 Mm^{-1}	
mass	internal case	$15 \mu\text{g m}^{-3}$		$10 \mu\text{g m}^{-3}$	
aerosol type					
species density		1.66 g cm^{-3}		2 g cm^{-3}	
specific mass scattering efficiency		$4 \text{ m}^2\text{g}^{-1}$		$2 \text{ m}^2\text{g}^{-1}$	
total scattering		60 Mm^{-1}		20 Mm^{-1}	

Figure 5.14 Part A is a schematic diagram contrasting mass scattering efficiencies associated with external and internal mixing, while part B addresses partial scattering mass scattering efficiencies for the externally and internally mixed cases.

However, the apportionment of scattering to species 1 and 2 is different under these two schemes. Under the externally mixed scenario, species 1 and 2 each contribute 50% of the total scattering. In the internally mixed case, species 1 would be interpreted as contributing 66% of the scattering budget, since it makes up 66% of the total mass, while species *b* would be interpreted to contribute 33%. The discrepancy arises because once the species are internally mixed the same scattering efficiency is assigned to both species. This apparent discrepancy can only be resolved if the specific efficiency of the mixed aerosol is prorated to its chemical constituents, based on their relative densities. If this is done, the apportionment of scattering to specific species is independent of whether the species is externally or internally mixed.

This simple example demonstrates that the estimation of each species' contribution to the total light extinction is sensitive to the assumed microscopic structure of the aerosol; White [1986] distinguishes this as the apportionment problem, distinct from the problem of computing the total extinction from knowledge of the size-dependent chemical composition, which we have just shown to be similar for the two cases in Figure 5.14A. In the externally mixed case, the total extinction for the mixture was calculated by computing the contribution of each species separately, with knowledge of the size distribution of each type of particle, and thus the contribution of each species to the total is well defined. For the internally mixed case, it may be misleading to assign a percentage of the total to each species on a mass-weighted basis, as demonstrated in Figure 5.14A.

The previous discussion concerns itself with apportioning extinction to a species as it resides in the ambient atmosphere. The discussion becomes more convoluted when the change in

ambient scattering as a function of removal of a species is of concern. In this case, one can recompute the total scattering for the aerosol upon removal of one of the species from the mixture and deduce the species' contribution to the mixture from the difference between these extinctions. We demonstrate this in Figure 5.14B, which computes the partial scattering efficiency for species 2 under the assumptions of externally and internally mixed particles. For the external case, shown in the top portion of Figure 5.14B, this partial scattering efficiency is obtained by recomputing the total aerosol scattering assuming only species 1 is present, which is equal to 30 Mm^{-1} , and subtracting this value from that obtained for the mixture, 60 Mm^{-1} . Thus one deduces that the $5 \mu\text{g m}^{-3}$ of species 2 contributed 30 Mm^{-1} to the mixed aerosol scattering, leading to a partial scattering efficiency of $6 \text{ m}^2 \text{ g}^{-1}$, [$\Delta b_{scat}/\Delta C_b = (60-30)\text{Mm}^{-1}/5 \mu\text{g m}^{-3}$], which is the same as the individual species 2 specific mass scattering efficiency from Figure 5.14A.

Figure 5.14B demonstrates the effect of removal of one species when the species are internally mixed. In this case, we have assumed that the removal of one species from the internal mixture would conserve particle number concentrations but reduce particle size. This size reduction has altered the specific mass scattering efficiency of species 1, which is now assumed to be $2 \text{ m}^2 \text{ g}^{-1}$. The total aerosol scattering is thus 20 Mm^{-1} , which leads to the conclusion that the partial scattering efficiency of species 2 is $8 \text{ m}^2 \text{ g}^{-1}$ [$\Delta b_{scat}/\Delta C_b = (60-20)\text{Mm}^{-1}/5 \mu\text{g m}^{-3}$].

This same issue arises when apportioning scattering to species that have different affinities for water. Consider an external mixture of equal masses of a hygroscopic and nonhygroscopic aerosol at a high relative humidity. The specific mass scattering efficiencies of the dry nonhygroscopic and hygroscopic species are $3 \text{ m}^2 \text{ g}^{-1}$, while that of the wet hygroscopic species is, because of associated water, $8 \text{ m}^2 \text{ g}^{-1}$. When mixed together, the wet specific efficiencies of the internally mixed particle will be between 3 and $8 \text{ m}^2 \text{ g}^{-1}$, depending on the hygroscopic nature of the mixed aerosol. A number of papers discuss aerosol growth characteristics as a function of RH and have successfully predicted the scattering characteristics of the mixed particles [Anderson *et al.*, 1994; Sloane, 1983; 1986]. However, the apportionment of scattering to the species that make up the aerosol is still problematic. For example, Saxena *et al.* [1995] found that the presence of organics appeared to either increase or decrease the hygroscopicity of inorganic species, probably depending on the type of organic present. In visibility modeling, the scheme often used is to develop one growth curve for the mixed species and then apportion scattering associated with water uptake proportionally among all aerosol components, even though the water uptake may be primarily associated with only one of the species. An example would be a mixture of ammonium sulfate and a weakly hygroscopic organic species.

The appropriateness of any apportionment scheme can only be judged within the context of whether the model is physically "reasonable," and whether independent apportionment of mass to extinction is consistent with measurements of scattering and absorption.

The strategy used to examine extinction apportionment in this report is to:

- 1) Assume an externally mixed aerosol, constant dry mass scattering efficiencies, and a functional dependence of scattering as a function of RH that is based on measured aerosol growth curves.

- 2) Assume an externally mixed aerosol but explicitly calculate sulfate scattering based on measured sulfur size distributions and estimated size distributions for other species.
- 3) Assume an internally mixed aerosol with measured sulfur size distributions and estimated size distributions for other species.

5.4.1 Aerosol Growth as a Function of Relative Humidity

Tang *et al.* [1981] has published data on growth curves, D/D_0 , as a function of increasing and decreasing relative humidity for $(\text{NH}_4)_2\text{SO}_4$, NH_4HSO_4 , and H_2SO_4 . For increasing or decreasing RH, the $(\text{NH}_4)_2\text{SO}_4$ and NH_4HSO_4 have sharp discontinuities at the deliquescence and crystallization relative humidities. However, because vertical atmospheric mixing during summer months in the eastern United States should almost always bring the aerosol into an RH environment that is in excess of 80% one can make the argument that the sulfate aerosol will always be on the crystallization branch of the hysteresis curve. Furthermore, because mixtures of ammonium aerosols with other species have been shown to be hygroscopic below the deliquescent values [Sloane, 1984, 1986; Stelson and Seinfeld, 1982], and because the growth factor and light-scattering efficiency for ambient aerosols has previously been observed to be rather smooth [Wexler and Seinfeld, 1991; Sloane, 1984, 1986; Sloane and Wolff, 1985; Waggoner *et al.* 1981], it is not known whether the ascending or descending limb of the hysteresis curve applies for a particular aerosol sample. Therefore as our "best" estimate for the sulfate species growth the curves were smoothed between the deliquescence and crystallization points. Finally, because it is not known exactly how sulfate will uptake water an upper limit of the amount of water associated with sulfate is estimated by using the crystallization branches of the hysteresis curves.

At the Great Smoky Mountains National Park monitoring site, the acidity of the sulfate aerosols varied from sampling period to sampling period. As an estimation of sulfate growth for acid aerosols whose molar ratios of ammonium to sulfate were somewhere between 0, 1 or 2 a linear interpolation between growth curves was carried out based on NH_4 to SO_4 ratios.

When species with different hygroscopic characteristics, such as organics and sulfates are mixed, it would be desirable to have a form of the semi-empirical growth curve that adjusts the aerosol hygroscopicity in response to changes in chemical composition. We suggest the application of the Zdanovskii-Stokes-Robinson (ZSR) assumptions, which account for solute-solvent interactions but neglect solute-solute interactions. In other words, each hygroscopic component brings into the mixture, at a particular RH, that amount of water that it would have in a binary solution in equilibrium at the same RH. The use of the ZSR assumptions for determination of the water content has been utilized by Saxena and Peterson [1981]. They examined the applicability of the ZSR assumptions to mixtures of inorganics, while Meng *et al.* [1995] applied it to mixtures of organics and inorganics. In the present case, the goal is to use the ZSR assumptions to derive an equation for the hygroscopic growth of internally mixed particles when the growth characteristics of the externally mixed species are either known or can be approximated. Applying the ZSR assumptions to the case of two solute species yields:

$$\left(\frac{D}{D_o}\right)^3 = \frac{\rho_{dry}}{\rho_{wet}} \left[z_1 \frac{\rho_{wet_1}}{\rho_{dry_1}} \left(\frac{D_1}{D_{o,1}}\right)^3 + z_2 \frac{\rho_{wet_2}}{\rho_{wet_2}} \left(\frac{D_2}{D_{o,2}}\right)^3 \right] \quad (5.15)$$

where z_i is the mass fraction of solute i , counting solute species only; $\rho_{wet,i}$ and $\rho_{dry,i}$ refer to the wet and dry densities of the binary solutions of solute i and water; ρ_{wet} and ρ_{dry} are the densities of the aqueous ternary and dry binary (two solute) mixtures, respectively; and $D_i/D_{o,i}$ refers to the individual growth curve for species i .

We propose Equation (5.15) as a first approximation for estimating the hygroscopic growth of a two component, internally mixed aerosol when the growth curves of both components are known, and will refer to this as the ideal solution (IS) growth curve. Equation (5.15) has the correct asymptotic form as the solute composition of the mixture is changed, in that the mixture growth curve is seen to approach the growth curve of the remaining species as one of the species is removed ($z_i \rightarrow 0$).

It should be noted models that treat water uptake for nonideal, multicomponent solutions using theoretical and semi-theoretical thermodynamic relationships have been developed and have been applied to both visibility and climate forcing problems [Pilinis *et al.*, 1995; Saxena and Peterson, 1981; Saxena *et al.*, 1986; 1993]. The correct treatment of the hygroscopicity of species in multicomponent mixtures—especially organic species—remains problematic, not only because of the lack of suitable mixture thermodynamic data, but also because of the lack of information about other critical mixture properties, such as density and refractive index. In the absence of more rigorous models for estimating the water activity of inorganic/organic mixtures, we will apply Equation (5.15) as a first approximation of the hygroscopic growth of such mixtures, and compare predictions using this model with those using the semi-empirical model to examine sensitivity of predicted quantities to the model assumptions.

5.4.2 The Externally Mixed Constant Mass Scattering Model

The equation used for these calculations is:

$$\begin{aligned} b_{scat} = & (3)f(RH)[SULFATE] \\ & + (3)f(RH)[NITRATE] \\ & + (4)f_{org}(RH)[OMC] \\ & + (1)[SOIL] \end{aligned} \quad (5.16)$$

In general, the higher the RH, the greater the scattering of soluble aerosols. The relationship between RH and scattering efficiency, referred to as $f(RH)$, is:

$$f(RH) = b_{scat}(RH) / b_{scat}(0\%), \quad (5.17)$$

where $b_{scat}(0\%)$ and $b_{scat}(RH)$ are the dry and wet scattering, respectively. The brackets indicate the species concentration, $3 \text{ m}^2 \text{ g}^{-1}$ is the dry scattering efficiency of sulfates and nitrates, and $4 \text{ m}^2 \text{ g}^{-1}$ is the dry organic carbon scattering efficiency. The fine soil mass scattering efficiency is $1 \text{ m}^2 \text{ g}^{-1}$, and is taken from a literature review by Trijonis and Pitchford [1987]. b_{scat} is the scattering coefficient measured by the nephelometer with the $2.5 \mu\text{m}$ inlet.

A dry scattering efficiency of $3 \text{ m}^2 \text{ g}^{-1}$ is a nominal scattering efficiency based on a literature review by Trijonis *et al.*, [1988, 1990] and a review by White [1990]. Trijonis' best estimate for sulfates and nitrates is $2.5 \text{ m}^2 \text{ g}^{-1}$ with an error factor of 2, while for organics it is $3.75 \text{ m}^2 \text{ g}^{-1}$ again with an error factor of 2. White [1990] took a somewhat different approach in that he reviewed 30 studies in which particle scattering and mass were measured. He then estimated a high and low scattering efficiency by using mass measurements to prorate the measured extinction. For sulfate the low estimate was arrived at by assuming that sulfate, nitrates, and organics scatter twice as efficiently as all other species, and for the high estimate he assumed that only sulfate was twice as efficient. His low and high sulfate mass scattering efficiencies for the rural west were 3.0 and $3.7 \text{ m}^2 \text{ g}^{-1}$, respectively. For organics his low estimate assumes that organics and other nonsulfate species scatter half as efficiently as sulfates, and for the high estimate he assumes organics are three, and sulfates twice as efficient at scattering light as other species. His low and high estimates for organic mass scattering coefficients are 1.8 and $4.1 \text{ m}^2 \text{ g}^{-1}$. Malm *et al.* [1996] examined relationships between b_{ext} and aerosols at 14 monitoring sites in the western United States and concluded the dry organic mass scattering efficiency was on the average about $4 \text{ m}^2 \text{ g}^{-1}$.

5.4.3 The Externally Mixed Variable Mass Scattering Model

The equation used to reconstruct scattering when the sulfate size distribution is known as:

$$\begin{aligned}
 b_{scat} = & e_{wd} ([SULFATE] + [NITRATE]) \\
 & + (4)f_{org}(RH)[OMC] \\
 & + (1)[SOIL]
 \end{aligned} \tag{5.18}$$

where e_{wd} is the size and relative humidity dependent scattering efficiency of the wetted sulfate aerosol and the variables in the brackets are the dry mass concentrations of the various species. It is assumed that the nitrate and sulfate size distributions are the same. The other variables are the same as those defined above.

5.4.4 The Internally Mixed Variable Mass Scattering Model

The equation used to reconstruct scattering when the sulfate size distribution is known and a size distribution for organics and nitrates is assumed is given by:

$$b_{scat} = e_{wdm} ([SULFATE] + [NITRATE] + [OMC]) + (1)[SOIL] \tag{5.19}$$

where e_{wdm} is the size and relative humidity dependent mass scattering efficiency for a sulfate, nitrate, and organic aerosol that is uniformly mixed. It is assumed that soil is externally mixed.

5.4.5 Estimation of Size Dependent Mass Scattering

The analysis of DRUM measured sulfur size distributions is confined to the five stages that collect particles with a diameter below 2.5 μm . The size-resolution afforded by the five size cuts is quite limiting when estimating scattering efficiencies using Mie theory because each stage removes particles over a wide range of sizes with variable efficiencies between 0 and 100%. Therefore, the mass size distributions are usually "inverted" to yield a smoothed estimate of $dC/d\log(D)$ [John *et al.*, 1990]. DRUM measurements were inverted using the Twomey [1975] scheme, which is a nonlinear iterative algorithm that accounts for the sampling efficiency as a function of particle size for each stage. The output of the inversion is 72 data pairs of $dC/d\log(D)$ and D , where C is the concentration of sulfur and D is the aerodynamic diameter. Geometric mass mean diameter and geometric standard deviation are calculated for each of these sulfur size distributions using Stokes diameters.

Using Mie theory, three theoretical mass scattering efficiencies are calculated from $dC/d\log(D)$ distributions, where D is the Stokes diameter. First, the dry mass scattering efficiency (e_d) was calculated by estimating the scattering ($b_{scat,d}$), assuming water was not mixed with the particle (RH=0.0%), and dividing that scattering by dry SO_4 species mass. Because the DRUM sampler measures the "wet" size, the dry size was calculated using (D/D_o) versus RH curves derived as discussed above. Second, a wet mass scattering efficiency (e_w) was arrived at by calculating the scattering of SO_4 species plus water ($b_{scat,w}$) and dividing it by the SO_4 species plus water mass. Finally, the water enhanced efficiency (e_{wd}) was calculated by $(b_{scat,w})/(\text{SO}_4 \text{ species})$. The water associated with sulfate species mass was calculated assuming volume conservation between sulfate and water. The index of refraction of the "wet" aerosol was arrived at by volume weighting the index of refraction for SO_4 species and water.

For the mixed model, the calculations were carried out in much the same way; however, the growth was calculated using Equation (5.15). Again the water associated with the mixed aerosol mass was calculated assuming volume conservation between sulfate, organics, and water. The index of refraction of the "wet" aerosol was arrived at by volume weighting the index of refraction for SO_4 species, organics, and water.

5.5 RESULTS

5.5.1 Sulfate Mass Size Distributions

Figures 5.15 and 5.16 show typical sulfur size distribution data for two sampling periods. Included on each graph are the $\Delta(\text{sulfate mass})/\Delta(\log(D))$ values derived directly from the DRUM sampler and from the results from the Twomey inversion calculation. Also reported on each graph are the corresponding geometric mean and geometric standard deviation. On JD 229.79 the sulfate aerosol is quite "large" with a geometric mean mass diameter, D_g , of 0.59 μm and a geometric standard deviation, σ_g , of 1.51, while on JD237.29 the $D_g=0.47 \mu\text{m}$ with a $\sigma_g=1.76$.

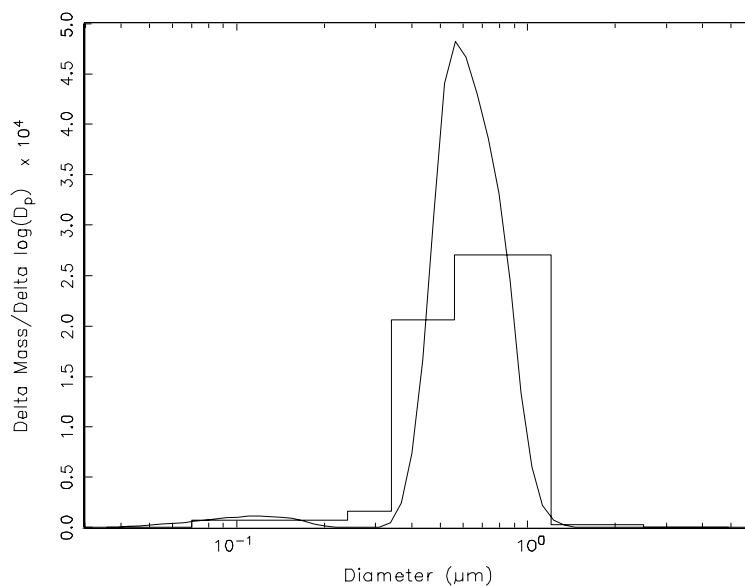


Figure 5.15 A sulfur mass size distribution for JD 229 that corresponds to a σ_g of 1.5 and a D_g equal to 0.60 μm . The smooth curve is the mass size distribution calculated using the Twomey [1975] inversion technique.

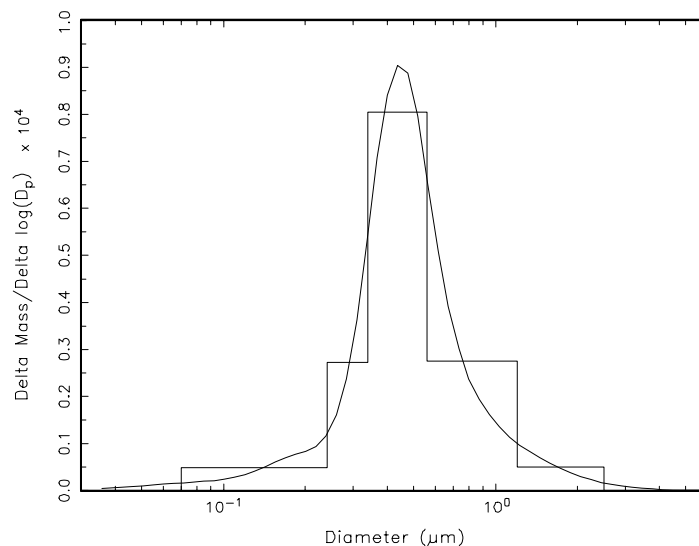


Figure 5.16 A sulfur mass size distribution for Julian day 237 that corresponds to a σ_g of 1.8 and a D_g equal to 0.47 μm . The smooth curve is the mass size distribution calculated using the Twomey (1975) inversion technique.

Table 5.6 is a statistical summary of sulfate species mass for the IMPROVE channel A sampler and the sum of the five DRUM stages below 2.5 μm , the mass mean diameter, and the geometric standard deviation. Various scattering parameters, which will be discussed in the next section, are also summarized. The average sulfate species concentrations are 14.95 and 14.01 μg

m^{-3} for the IMPROVE and DRUM samplers, respectively. The mass mean diameter is 0.38, while the σ_g is 1.92.

Table 5.6 Statistical summary of measured mass concentrations, relative humidity, size parameters, and mass scattering efficiencies.

Variable	Mean	Std. Dev.	Minimum	Maximum	N
IMPROVE sulfate species mass ($\mu\text{g m}^{-3}$)	14.95	11.37	2.09	48.23	45
DRUM sulfate species mass ($\mu\text{g m}^{-3}$)	14.01	10.26	1.29	44.49	45
Water mass ($\mu\text{g m}^{-3}$)	22.24	15.33	2.44	69.72	45
Relative humidity (%)	74.98	8.94	54.66	92.24	45
Geometric mass mean diameter (μm)	0.38	0.07	0.18	0.51	45
Geometric standard deviation	1.92	0.27	1.47	2.36	45
Dry mass scattering efficiency ($\text{m}^2 \text{g}^{-1}$)	2.77	0.66	1.32	3.95	45
Wet mass scattering efficiency ($\text{m}^2 \text{g}^{-1}$)	3.71	0.66	1.75	4.80	45
Enhanced mass scattering efficiency ($\text{m}^2 \text{g}^{-1}$)	10.51	3.52	3.25	19.90	45
Wet scattering (km^{-1})	0.15	0.12	0.01	0.55	45
Dry scattering (km^{-1})	0.04	0.04	0.00	0.18	45

Figure 5.17 shows a scatter plot of sulfate species concentration derived from summing the DRUM stages less than $2.5 \mu\text{m}$ and the IMPROVE sampler. The data points are scattered about the 1:1 line showing that there is little bias between the two samplers, and, more importantly, there wasn't an appreciable loss of particles by the DRUM sampler. The R^2 for an OLS regression between the two variables was 0.89 and on the average the DRUM and IMPROVE samplers compared to within about 6%.

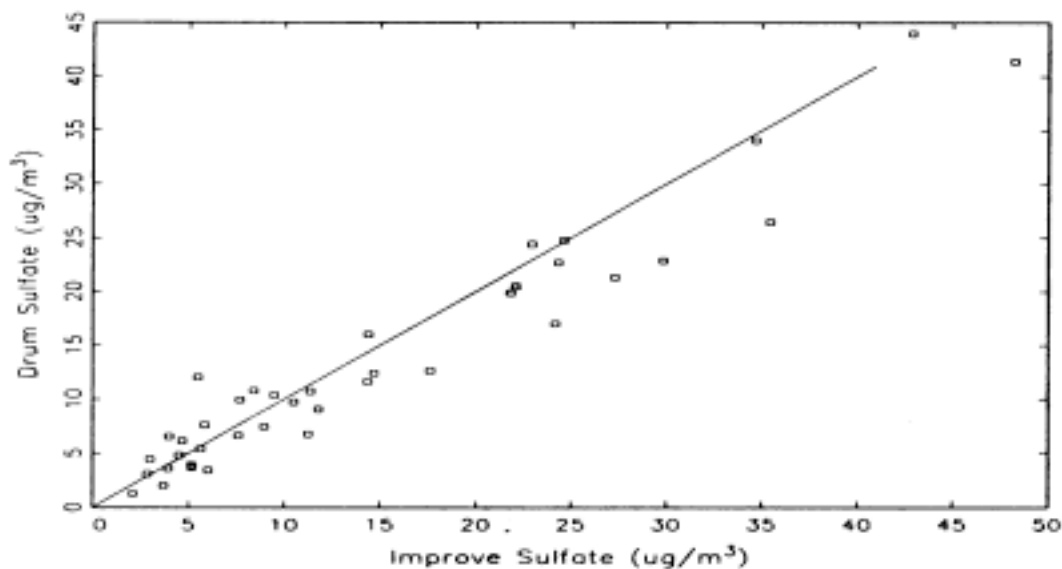


Figure 5.17 Scatter plot of the sum of the sulfate species (sulfate + ammonium + hydrogen) on the DRUM stages and sulfate species measured using a single stage cyclone sampler with a $2.6 \mu\text{m}$ cut point. The 1:1 line is included for reference.

Figure 5.18 is a three-dimensional time plot of the Twomey inverted DRUM data. The time scale is in integer numbers corresponding to 4-hr sampling periods, the z-axis is $dC/d\log(D)$, where C is the concentration of sulfate in an increment of $\log(D)$, and the y-axis is particle diameter in μm . The data set shows that the mass size distributions vary considerably over time, both in terms of D_g and σ_g .

5.5.2 Calculation of Sulfate Mass Scattering Efficiencies from DRUM Data

The dry mass scattering efficiency (e_d), wet mass scattering efficiency (e_w), and water-enhanced efficiency (e_{wd}) are summarized in Table 5.6. e_d and e_w are 2.77 and $3.71 \text{ m}^2 \text{ g}^{-1}$, respectively. A dry mass scattering efficiency of $2.77 \text{ m}^2 \text{ g}^{-1}$ is somewhat less than the $3.0 \text{ m}^2 \text{ g}^{-1}$ used by a number of authors to estimate sulfate scattering. The average enhanced mass scattering efficiency, e_{wd} , on the other hand, is $10.51 \text{ m}^2 \text{ g}^{-1}$ for an average relative humidity of 75%.

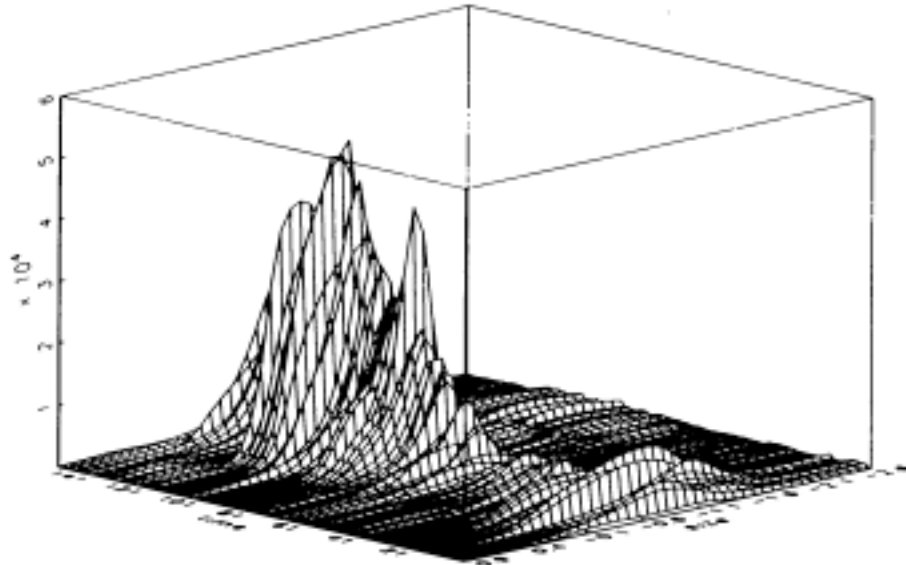


Figure 5.18 Three-dimensional time plot of Twomey's [1975] inverted mass size data. The x-axis is sample number, the y-axis is log of particle diameter, and the z-axis is mass concentration per increment of log diameter, $(dC/d\log(D)) \times 10^4$.

Interrelationships among the aerosol descriptive parameters, D_g , σ_g , e_d , and sulfate concentration, and ambient relative humidity can be more easily explored by using a scatter plot of each variable scattered against the others. Figure 5.19 presents these data. Sulfate mass is in $\mu\text{g m}^{-3}$, σ_g is the geometric standard deviation and is unitless, the mass scattering efficiency is in $\text{m}^2 \text{ g}^{-1}$, and relative humidity is expressed in percent. The lines drawn through the data points in the scatter plots are not quantitative but have been added to highlight some qualitative features.

The first row of scatter plots explores the relationship between sulfate mass and D_g , σ_g , e_w , and RH. There appears to be a weak relationship between sulfate mass and D_g with the largest sulfate sizes found on the days with the highest sulfate concentrations. The relationship between sulfate species mass concentration and e_w is quite interesting. At low mass concentrations

efficiencies can vary from about 2 to 4 $\text{m}^2 \text{g}^{-1}$, however, as sulfate mass increases the mass scattering efficiencies tend to increase and converge to a value of near 5 $\text{m}^2 \text{g}^{-1}$ for the highest sulfate concentrations. There is no apparent relationship between relative humidity and sulfate mass. Large σ_g s (>2.5) only occur when sulfate concentrations are quite low, while smaller σ_g s can occur under high and low sulfate concentrations.

The second row of the multiple scatter plots shows the relationships between D_g and (e_w , and RH). There is a weak inverse relationship between D_g and e_w in that larger mass mean diameters are associated with more peaked and narrow size distributions. This trend is reflected in the D_g versus e_w plots with higher mass scattering efficiencies observed at the larger diameters. Part of the strong relationship between D_g and e_w is also a result of the relationship between RH and particle diameter; particle diameter increases as relative humidity increases. Larger particles are associated with higher RH and therefore lower densities. The lower densities in turn tend to increase the mass scattering efficiencies.

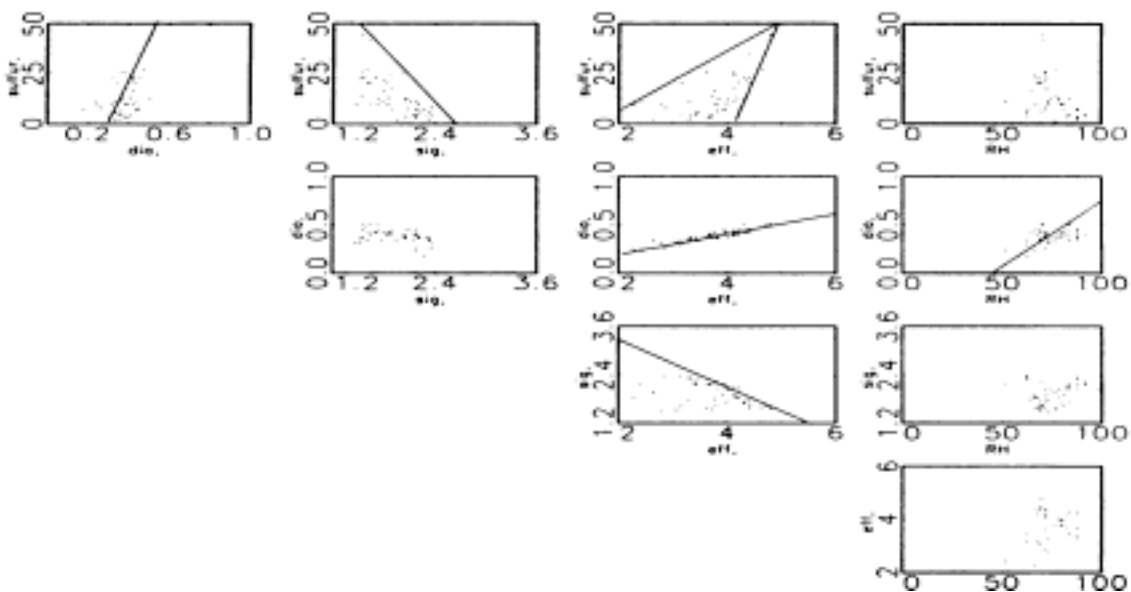


Figure 5.19 Multiple scatter plot of sulfate species (sulfate plus ammonium) concentration ($\mu\text{g m}^{-3}$), geometric mass mean diameter ($D_g(\mu\text{m})$), geometric standard deviation (σ_g), and relative humidity ($\text{RH}(\%)$).

There is a negative correlation between σ_g and e_w , which is caused, in part, because the narrow size distributions have more of the particles near the optimal size for light scattering compared to the broader distributions.

5.5.3 Results for the Externally Mixed Constant Mass Scattering Model

The function, $f(\text{RH})$, for sulfate aerosol species was calculated on a sampling-period-by-sampling-period basis using Tang's sulfate D/D_o curves that were smoothed between the crystallization and deliquescent points and interpolated between $(\text{NH}_4)_2\text{SO}_4$, NH_4HSO_4 , and H_2SO_4 , as described previously. A sulfate species geometric mass size distribution with a

geometric mass mean diameter of 0.3 μm and a geometric standard deviation of 1.5 was assumed. The $f(\text{RH})$ associated with nitrates was assumed to be the same as for sulfates, while $f(\text{RH})$ for organics was set equal to one. Results of these calculations are summarized in Table 5.7 and shown in Figure 5.20, where measured and reconstructed scattering, calculated using Equation (5.16), are scattered against each other. Also plotted in Figure 5.20 is the 1:1 line. The average $f(\text{RH})$ factor is 3.11 yielding an average sulfate scattering ($f(\text{RH})\text{SO}_{4,\text{scat}}$) value of 0.129 km^{-1} , which in turn yields an average reconstructed scattering (reconstructed $f(\text{RH})b_{\text{scat}}$), of 0.152 km^{-1} , which is about 20% less than measured scattering.

Table 5.7 Statistical summary of measured b_{scat} , reconstructions of b_{scat} , $f(\text{RH})$, and scattering associated with various aerosol species. Except for $f(\text{RH})$, which is unitless, all units are in km^{-1} . The parenthetical values in the mean column are the percent contribution of the respective species to the "average" or "best estimate" of reconstructed scattering.

Variable	Mean	Std. Dev.	Minimum	Maximum	Valid
Measured b_{scat}	0.185	0.133	0.045	0.611	45
Reconstructed $f(\text{RH})b_{\text{scat}}$	0.152	0.098	0.033	0.454	45
Reconstructed avg. b_{scat}	0.184	0.145	0.029	0.662	45
Reconstructed cryst. b_{scat}	0.187	0.147	0.029	0.673	45
Reconstructed del. b_{scat}	0.175	0.142	0.029	0.646	45
Reconstructed mix b_{scat}	0.192	0.142	0.043	0.667	45
Relative humidity ($\leq 95\%$)	74.990	8.94	51.660	92.240	45
$f(\text{RH})$	3.110	0.95	1.590	5.960	45
$f(\text{RH})\text{SO}_{4,\text{scat}}$	0.129	0.093	0.020	0.420	45
Average $\text{SO}_{4,\text{scat}}$	0.160 (0.870)	0.140	0.016	0.627	45
Cryst. $\text{SO}_{4,\text{scat}}$	0.163	0.143	0.016	0.640	45
Del. $\text{SO}_{4,\text{scat}}$	0.150	0.138	0.010	0.611	45
OC_{scat}	0.021 (0.110)	0.007	0.001	0.034	45
$f(\text{RH})\text{NO}_{3,\text{scat}}$	0.002 (0.010)	0.001	0.000	0.004	45
Soil $_{\text{scat}}$	0.002 (0.010)	0.002	0.000	0.008	45
CM_{scat}	0.005	0.004	0.000	0.015	45

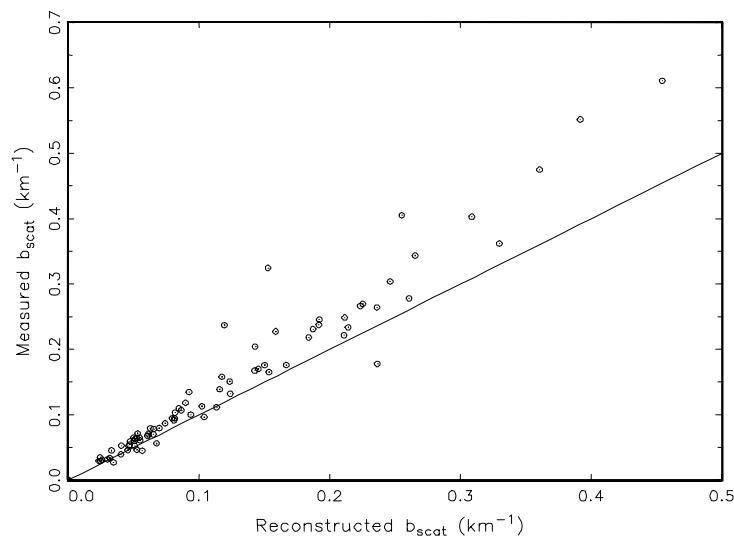


Figure 5.20 A scatter plot of reconstructed and measured PM_{2.5} scattering assuming external mixing and a constant ammonium bisulfate dry mass scattering efficiency of 3.0 m²/g and an $f(RH)$ curve corresponding to $D_g=0.3 \mu\text{m}$, $\sigma_g=1.5$. The 1:1 line is shown for reference, and units are in km⁻¹.

An OLS regression yielded a very high R^2 of 0.94, however, the OLS regression line is about 1.28 implying measured scattering is about 30% greater than reconstructed. Similar discrepancies between reconstructed and measured scattering were noted previously [Gebhart and Malm, 1990] using data gathered at Shenandoah National Park. For the most part the use of Equation (5.16) to reconstruct scattering works well for most western IMPROVE sites [Malm *et al.* 1996]. The inability to use Equation 5.16 and the associated assumptions to reconstruct scattering at nonurban eastern sites was part of the motivation for carrying out SEAVS.

5.5.4 Results for the Externally Mixed Model with Sulfate Mass Scattering Efficiencies Estimated from Mass Size Distributions

The same strategy described above for estimating D/D_o was used. However, to develop the range of possible sulfate scattering associated with the crystallization, deliquescent, and average branches of the growth curves, each was used in the reconstructed scattering calculation and the results are presented in Table 5.7 under Cryst SO_{4,scat}, Del SO_{4,scat}, and Average SO_{4,scat}, respectively. There are only small differences between the three estimations. The crystallization SO_{4,scat} is about 2% greater than the average SO_{4,scat}, while the deliquescent SO_{4,scat} is about 7% less than the average. Because other species also contribute to scattering the net effect of the three different assumptions on total PM_{2.5} scattering is even less.

Results of the calculation are further highlighted in a scatter plot shown in Figure 5.21, where the range of scattering associated with using the crystallization, average, and deliquescent branches of the growth curve are used. Also shown in the scatter plot is the 1:1 line. Visual

examinations of the scatter plot shows that the reconstructed and measured scattering compares quite favorably. An OLS regression between measured and reconstructed scattering using the "average" growth curves yields an R^2 of 0.94 and a slope of 0.89 and an offset of 0.02 km^{-1} . The parenthetical values in Table 5.7 are the percent contribution of each species to $\text{PM}_{2.5}$ scattering using the "average" growth model. Sulfates, organics, nitrates, and soil contribute 87%, 11%, 1%, and 1%, respectively.

As an example of the temporal variability Figure 5.22 shows the time lines of measured, sulfate species, nitrate, organics, and soil scattering for the "average" growth model, while Figure 5.23 shows a time line of the percent contribution to scattering associated with each species. The units in Figure 5.22 are in mm^{-1} , while the units of b_{scat} in Figure 5.23 are in units of km^{-1} and those of the species are in fractions. Sulfate scattering varies from about 0.05 km^{-1} to a high of over 0.6 km^{-1} : over an order of magnitude change in scattering! Nitrate scattering varies around 0.002 km^{-1} , while organics vary from about 0.004 to 0.04 km^{-1} also an order of magnitude change. However, organic scattering is about an order of magnitude less than sulfate scattering. There is one soil episode occurring on JD 206-208, where the soil scattering is almost 0.01 km^{-1} as compared to the more typical values of 0.002 - 0.003 km^{-1} . It should be pointed out, however, that the soil episode at 0.01 km^{-1} is still about five times less than the lowest sulfate scattering values.

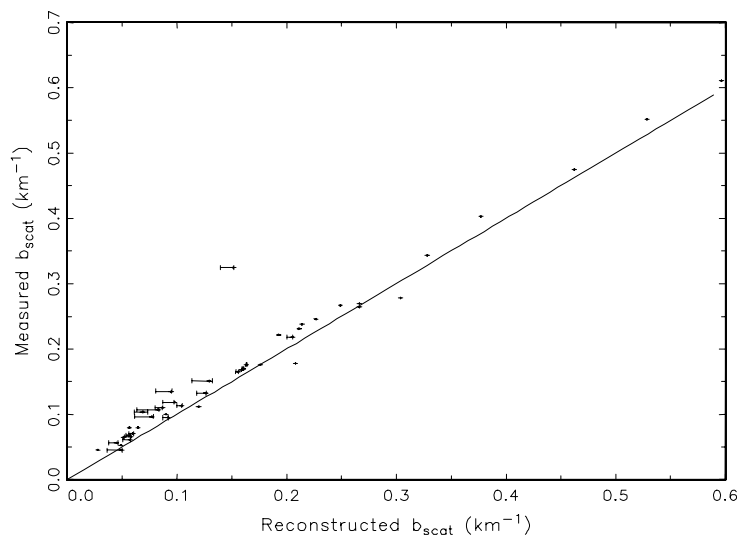


Figure 5.21 A scatter plot of reconstructed and measured $\text{PM}_{2.5}$ scattering assuming external mixing but with measured sulfur size distributions. The range of reconstructed scattering was arrived at by assuming three different forms of Tangs' D/D_0 curves for $(\text{NH}_4)_2\text{SO}_4$, NH_4HSO_4 , and H_2SO_4 . The highest reconstruction is arrived at by using the crystallization branches, the middle value from an average growth between the crystallization and deliquescence branches, while the lowest reconstruction was calculated using the deliquescent arm of the growth curves. Units are in km^{-1} .

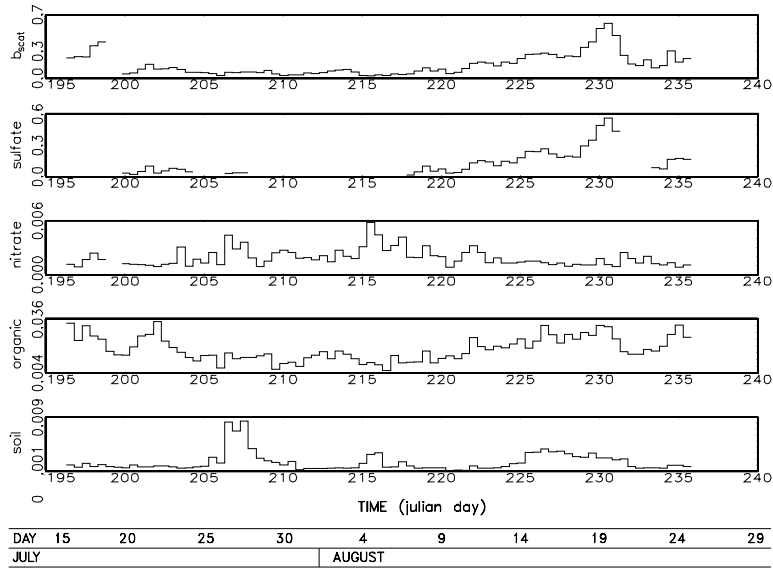


Figure 5.22 Time lines showing b_{scat} (b_{scat}), sulfate species scattering (sulfate), ammonium nitrate scattering (nitrate), organic mass scattering (organic), and soil scattering (soil). The best estimate D/D_o growth curve and measured sulfur mass size distributions were used. Units on scattering are in km^{-1} , while time is presented as Julian day.

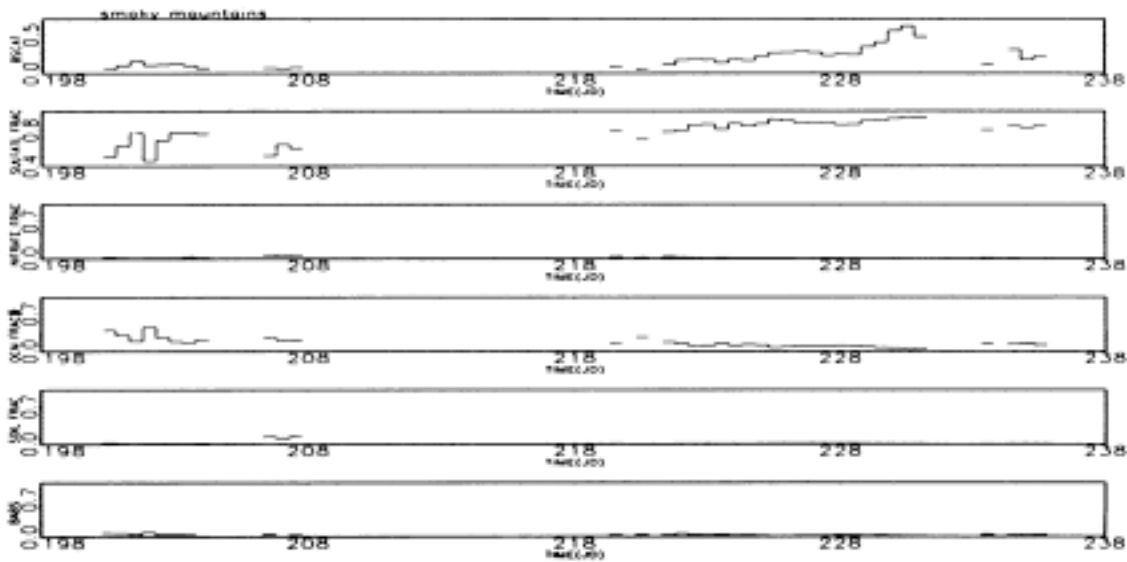


Figure 5.23 Time lines show reconstructed b_{scat} and the fraction each species contributes to scattering. The average D/D_o growth curve and measured sulfur mass size distributions were used. Time is in Julian day and scattering is in km^{-1} .

5.5.5 Results for the Internally Mixed Model with Measured Sulfur Size Distributions and Estimated Size Distributions for Other Species

For the internally mixed model, it was assumed that sulfates, nitrates, and organics were uniformly mixed with nitrates and sulfates having the measured sulfur mass size distribution, and that organics were lognormally distributed with a mass mean diameter of 0.4 μm and a geometric standard deviation of 2.0. The growth of the mixed particle was calculated using Equation (5.15) with D/D_o set equal to 1 for organics (organics considered to be nonhygroscopic), while nitrates were assumed to have the same growth as sulfates. D/D_o for sulfate species was calculated using the "average" growth curve as described above.

Results of the calculation are summarized in Table 5.7 and Table 5.8. Table 5.8 should be compared to Table 5.6, which shows the same parameters for externally mixed sulfate species. The water masses for the external and mixed cases are nearly the same as are the size parameters. However, the scattering efficiencies are quite different. For instance, the enhanced mass scattering efficiency, e_{wdm} , for the mixed particle is $8.63 \text{ m}^2 \text{ g}^{-1}$, while for the externally mixed sulfate aerosol it is $10.51 \text{ m}^2 \text{ g}^{-1}$. The lower efficiency of the mixed aerosol is a reflection of the increased mass (sulfate+organics+nitrates) being associated with the same amount of water.

Table 5.8 *Statistical summary of water mass, relative humidity, size parameters, mass scattering efficiencies, and wet and dry scattering for the mixed aerosol model.*

Variable	Mean	Std. Dev.	Minimum	Maximum	N
Water mass	22.31	13.05	4.59	66.43	45
Relative humidity	74.98	8.94	51.66	92.24	45
Geometric mass mean diameter	0.38	0.04	0.27	0.47	45
Geometric standard deviation	1.97	0.15	1.72	2.30	45
Dry mass scattering efficiency	2.84	0.41	2.18	3.83	45
Wet mass scattering efficiency	4.47	0.52	3.11	5.24	45
Enhanced mass scattering efficiency	8.63	2.29	.090	13.84	45
Wet scattering	0.22	0.13	0.08	0.66	45
Dry scattering	0.08	0.15	0.02	0.23	45

Figure 5.24 shows a scatter plot of the internally and externally mixed model scattered against measured scattering, while a simple statistical summary of the reconstructed scattering is presented in Table 5.7. The horizontal bars represent the results of the internal and external model, with the largest reconstruction corresponding to the internal model and the lowest reconstruction with the external calculation. In most cases, the difference, as expected, between the internal and external case is small. The average difference between the two calculations is only about 4%, with the mixed model yielding the higher reconstructed scattering estimates.

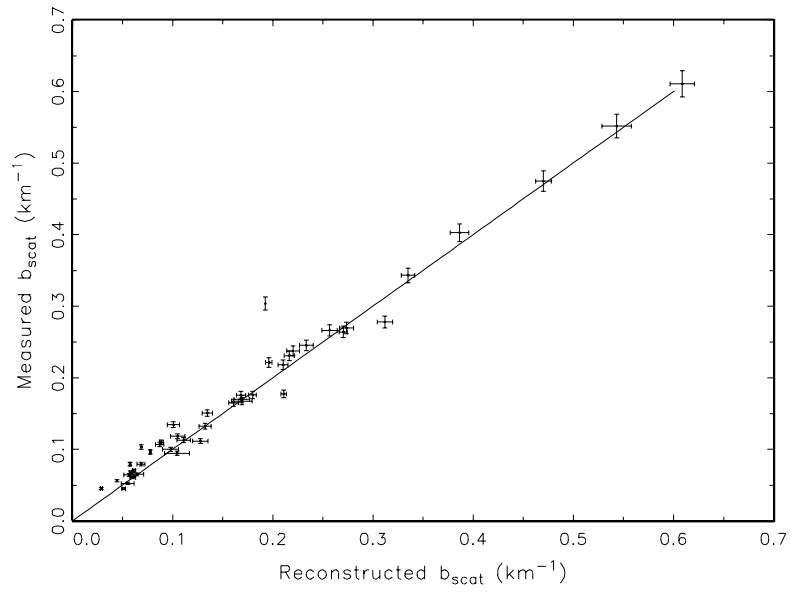


Figure 5.24 *Scatter plot of reconstructed and measured scattering along with the 1:1 line. The upper and lower bound of reconstructed scattering correspond to assuming an internally and externally mixed aerosol.*

5.6 REFERENCES

- Anderson, T.L., R.J. Charlson, W.H. White, and P.H. McMurry, Comment on: light scattering and cloud condensation nucleus activity of sulfate aerosol measured over the northeast Atlantic Ocean, *Journal of Geophysical Research*, **99**(D12): 25, 947-25, 949, 1994.
- Appel, B.R., Y. Tokiwa, J. Hsu, L.E. Kothny, E. Hahn, and J.J. Wesolowski, Visibility as related to atmospheric aerosol constituents, *Atmospheric Environment*, **19**:1525-1534, 1985.
- Cahill, T.A., L.L. Ashbaugh, R.A. Eldred, P.J. Feeney, B.H. Kusko, and R.G. Flocchini, Comparisons between size-segregated resuspended soil samples and ambient aerosols in the western United States, in *Atmospheric Aerosol: Source/Air Quality Relationships*, American Chemical Society Symp. Ser., 167, edited by E. Macias, Washington, D.C., 1981.
- Cass, G.R., On the relationship between sulfate air quality and visibility with examples in Los Angeles, *Atmospheric Environment*, **13**:1069-1084, 1979.
- Chow, J.C., J.G. Watson, L.C. Pritchett, W.R. Pierson, C.A. Frazier, and R.G. Purcell, The DRI thermal/optical reflectance carbon analysis system: description, evaluation, and applications in U.S. air quality studies, *Atmospheric Environment*, **27**(A), (8): 1185-1201, 1993.
- Dietrich, D.L., J.V. Molenar, and J.F Faust, Transmissometer extinction measurements in an urban environment, in *Visibility and Fine Particles*, edited by C.V. Mathai, pp. 374-383, 1989.
- Dzubay, T.G., and K.W. Clubb, Comparison of telephotometer measurements of extinction coefficients with scattering and absorption coefficients, *Atmospheric Environment*, **15**:2617-2624, 1981.
- Dzubay, T.G., R.K. Stevens, C.W. Lewis, D.H. Hern, W.J. Courtney, J.W. Tesch, and M.A. Mason, Visibility and aerosol composition in Houston, TX, *Environmental Science and Technology*, **16**:514-525, 1982.
- Eldred, R.A., T.A. Cahill, M. Pitchford, and W.C. Malm, IMPROVE--a new remote area particulate monitoring system for visibility studies, Proceedings of the Air Pollution Control Association 81st Annual Meeting, Dallas, TX, June 19-24, Paper No. 88-54.3, 1-16, 1988.
- Ferek, R.J., A.L. Lazrus, P.L. Haagenson, and J.W. Winchester, Strong and weak acidity of aerosols collected over the northeastern United States, *Environmental Science and Technology*, **17**:315-324, 1983.
- Ferman, M. A., G.T Wolff, and N.A. Kelly, The nature and sources of haze in the Shenandoah Valley/Blue Ridge mountains area, *Journal of the Air Pollution Control Association*, **31**: 1074-1082, 1981.

- Gebhart, K.A., and W.C. Malm, Source apportionment of particulate sulfate concentrations at three national parks in the eastern United States, In: Transactions of the AWMA/EPA International Specialty Conference on Visibility and Fine Particles, AWMA, Pittsburgh, PA, 1990.
- Groblicki, P.J., G.T. Wolff, and R.J. Countess, Visibility-reducing species in the Denver "brown cloud"- I. Relationships between extinction and chemical composition, *Atmospheric Environment*, **15**:2473-2484, 1981.
- Hasan H., and T.G. Dzubay, Apportioning light extinction coefficients to chemical species in atmospheric aerosols, *Atmospheric Environment*, **17**:1573-1581, 1983.
- Heisler, S.L., R.C. Henry, J.G. Watson, and G.M. Hidy, The 1978 Denver winter haze study volume II, ERT document #P-5417-1. Environmental Research and Technology, Inc., West Lake Village, CA, 1980a.
- Heisler, S.L., R.C. Henry, and J.G. Watson, The source of the Denver haze in November and December 1978, Paper 80-58.6, presented at the 73rd Annual Meeting of the Air Pollution Control Association, Pittsburgh, PA, 1980b.
- Heisler, S.L., I. Tombach, D. Fitz, J. Watson, and J. Chow, Tucson urban haze study, Final Report, Arizona Dept. of Environmental Quality, Phoenix, AZ, Doc #0493-005-804, 1994.
- Horvath, H., Atmospheric light absorption - A review, *Atmospheric Environment*, **27**(A)(3):293-317, 1993.
- Huffman, H.D., Comparison of the light absorption coefficient and carbon measures for remote aerosols: an independent analysis of data from the IMPROVE network - I, *Atmospheric Environment*, **30**:73-83, 1996a.
- Huffman, H.D., The reconstruction of aerosol light absorption by particle measurements at remote sites: an independent analysis of data from the IMPROVE network - II, *Atmospheric Environment*, **30**:85-99, 1996b.
- John, W., S.M. Wall, J.F. Ondo, and J.L. Winklmayr, Modes in the size distributions of atmospheric inorganic aerosol, *Atmospheric Environment*, **24**:2349-2359, 1990.
- Lewis, C.W., and T.G. Dzubay, Measurement of light absorption extinction in Denver, *Aerosol Science Technology*, **5**:325-336, 1986.
- Macias, E.S., J.O. Zwicker, and W.H. White, Regional haze case studies in the southwestern United States II: source contributions, *Atmospheric Environment*, **15**:1987-1997, 1981.
- Malm, W.C., J.V. Molenaar, R.A. Eldred, and J.F. Sisler, Examining the relationship between atmospheric aerosols and light scattering and extinction in the Grand Canyon, *Journal of Geophysical Research*, **101**(D14):19251-19265, 1996.

- Malm, W.C., Y. Golestani, K.A. Gebhart, T.A. Cahill, R.A. Eldred, and R. Poirot, Estimation of aerosol acidity in the eastern United States, Proceedings of the 84th Annual Meeting of the Air & Waste Management Association, Vancouver, B.C., 1991.
- Malm, W.C., J.F. Sisler, D. Huffman, R.A. Eldred, and T.A. Cahill, Spatial and seasonal trends in particle concentration and optical extinction in the United States, *Journal of Geophysical Research*, **99**(D1):1347-1370, 1994.
- McMurry, P.H., X. Zhang, and C.-T. Lee, Issues in aerosol measurement for optics assessments, *Journal of Geophysical Research*, **101**(D14):19189-19197, 1996.
- Meng Z., J.H. Seinfeld, and P. Saxena, Gas/aerosol distribution of formic and acetic acids. *Aerosol Sci. & Technol.* **23**(4):561-578, 1995
- Noll, K.E., Collection and characteristics of atmospheric coarse particles, Final Report, Dept. of Environmental Engineering, Illinois Institute of Technology, Chicago, 1991.
- Noll, K.E., A. Pontius, R. Frey, and M. Gould, Comparison of atmospheric coarse particles at an urban and non-urban site, *Atmospheric Environment*, **19**(11):1931-1943, 1985.
- Ouimette, J.R., and R.C. Flagan, The extinction coefficient of multicomponent aerosols, *Atmospheric Environment*, **16**:2405-2419, 1982.
- Ouimette, J.R., R.C. Flagan, and A.R. Kelso, Chemical species contributions to light scattering by aerosols at a remote arid site: Comparison of statistical and theoretical results, in: E.S. Macias and P.K. Hopke, eds. American Chemical Society Symposium, Series 167: Atmospheric Aerosol, 1981.
- Pierson, W.R., W.W. Brachaczek, T.J. Truex, et al., Ambient sulfate measurements on Allegheny Mountain and the question of atmospheric sulfate in the northeastern United States, reprinted from *Annals of the New York Academy of Sciences*, 338:145-173, 1980.
- Pilinis, C., S.N. Pandis, and J.H. Seinfeld, Sensitivity of direct climate forcing by atmospheric aerosols to aerosol size and composition, *Journal of Geophysical Research*, **100**(D9):18739-18754, 1995.
- Pitchford, M., R.G. Flocchini, R.G. Draftz, T.A. Cahill, L.L. Ashbaugh, and R.A. Eldred, Silicon in submicron particles in the southwest, *Atmospheric Environment*, **15**:321-333, 1981.
- Saxena P., and T.W. Peterson, Thermodynamics of multicomponent electrolytic aerosols, *Journal Colloid Interface Science*, **79**:496-510, 1981.
- Saxena P., L.M. Hildemann, P.H. McMurry, and J.H. Seinfeld, Organics alter hygroscopic behavior of atmospheric particles. *Journal of Geophysical Research*, **100**:18755-18770, 1995.

- Saxena P., A.B. Hudischewskyj, C. Seigneur, and J.H. Seinfeld, A comparative study of equilibrium approaches to the chemical characterization of secondary aerosols, *Atmospheric Environment*, **20**:1471-1483, 1986.
- Saxena P., P.K. Mueller, Y.P. Kim, J.H. Seinfeld, and P. Koutrakis, Coupling thermodynamic theory with measurements to characterize acidity of atmospheric particles, *Aerosol Science and Technology*, **19**:279-293, 1993.
- Sisler, J.F., Spatial and seasonal patterns and long term variability of the composition of the haze in the United States: An analysis of data from the IMPROVE network, Cooperative Institute for Research in the Atmosphere (CIRA), Colorado State University, Fort Collins, Colorado 80523, ISSN: 0737-5352-32, 1996.
- Sisler, J.F., D. Huffman, D.A. Latimer, W.C. Malm, and M.L. Pitchford, Spatial and temporal patterns and the chemical composition of the haze in the United States: An analysis of data from the IMPROVE network, 1988-1991, Cooperative Institute for Research in the Atmosphere Report, Colorado State University, Fort Collins, ISSN: 0737-5352-26, 1993.
- Sloane, C.S., Optical properties of aerosols-comparison of measurements with model calculations, *Atmospheric Environment*, **17**:409-416, 1983.
- Sloane, C.S., Optical properties of aerosols of mixed composition, *Atmospheric Environment*, **18**:871-878, 1984.
- Sloane, C.S., Effect of composition on aerosol light scattering efficiencies, *Atmospheric Environment*, **20**:1025, 1986.
- Sloane, C.S., and G.T. Wolff, Prediction of ambient light scattering using a physical model responsive to relative humidity: validation with measurements from Detroit, *Atmospheric Environment*, **19**:669-680, 1985.
- Stelson, A.W, and J.H. Seinfeld, Relative humidity and temperature dependence of the ammonium nitrate dissociation constant, *Atmospheric Environment*, **15**:983, 1982.
- Tang, I.N., W.T. Wong, and H.R. Munkelwitz, The relative importance of atmospheric sulfates and nitrates in visibility reduction, *Atmospheric Environment*, **15**(12): 2463, 1981.
- Tombach, I., and S.A. Thurston, The quality of the SCENES measurements: the roles of data quality goals and evolving technology, in Proceedings Aerosols and Atmospheric Optics: Radiative Balance and Visual Air Quality, Air & Waste Management Association, Pittsburgh, PA, 1994.
- Trijonis, J.C., and M. Pitchford, Preliminary extinction budget results from the RESOLVE program, edited by P.S. Bhardwaja, Visibility Protection Research and Policy Aspects, Air Pollution Control Association, Pittsburgh, Pa., 1987.

- Trijonis, J.C., W.C. Malm, M. Pitchford, W.H. White, R. Charlson, and R. Husar, Visibility: Existing and historical conditions-Causes and effects, in State of Science Technology Report 24, National Acid Precipitation Assessment Program, Washington, D.C., 1990.
- Trijonis, J.C., M. McGown, M. Pitchford, D. Blumenthal, P. Roberts, W. White, E. Macias, R. Weiss, A. Waggoner, J. Watson, J. Chow, and R. Flocchini, RESOLVE Project Final Report: Visibility Conditions and Causes of Visibility Degradation in the Mojave Desert of California, NWC TP #6869, Naval Weapons Center, China Lake, CA, 1988.
- Twomey, S., Comparison of constrained linear inversion and an iterative non-linear algorithm applied to the indirect estimation of particle size distributions, *Journal Comput. Phys.*, **18**:188-200, 1975.
- vandeHulst, H.C., Light scattering by small particles, Dover Publications, New York, 1981.
- Waggoner, A.P., R.E. Weiss, N.C. Ahlquist, D.S. Covert, S. Will, and R.J. Charlson, Optical characteristics of atmospheric aerosols, *Atmospheric Environment*, **15**(10/11):1891-1909, 1981.
- Watson J.G., J.C. Chow, L. W. Richards, W.D. Neff, S.R. Andersen, D.L. Dietrich, and I. Olmez, The 1987-88 Metro Denver brown cloud study, Desert Research Institute, Document No. 8810 1F2, Reno Nevada, 1988.
- Watson, J.G., J.C. Chow, L.C. Pritchett, L.W. Richards, D.L. Dietrich, J. Molenaar, J. Faust, S.R. Andersen, and C.S. Sloane, Comparison of three measures of extinction in Denver, CO, paper #89-151.4, presented at the Air Pollution Control Association Annual Meeting, 1989.
- Watson, J.G., J.C. Chow, L.W. Richards, D.L. Haase, C. McDade, L.D. Dietrich, D. Moon, L. Chinkin, and C. Sloane, The 1989-90 Phoenix urban haze study. Volume I: program plan. DRI document 8931.1F, prepared for Arizona Department of Environmental Quality, Phoenix, AZ, by Desert Research Institute, Reno, NV, 1990a.
- Watson, J.G., J.C. Chow, L.W. Richards, D.L. Haase, C. McDade, D.L. Dietrich, D. Moon, L. Chinkin, and C. Sloane, The 1989-90 pilot Tucson urban haze study. Volume I: program plan. DRI document 8931.3F, prepared for Arizona Department of Environmental Quality, Phoenix, AZ, by Desert Research Institute, Reno, NV, 1990b.
- Wexler A., and J. Seinfeld, Second-generation inorganic aerosol model, *Atmospheric Environment*, **25A**(12): 2731, 1991.
- White, W.H., On the theoretical and empirical basis for apportioning extinction by aerosols: a critical review, *Atmospheric Environment*, **20**:1659, 1986.
- White, W.H., Contributions to light scattering, in: Acidic Deposition: State of Science and Technology Report 24, J. Trijonis (lead author), National Acid Precipitation Assessment Program, Washington, D.C., pp85-102, 1990.

White, W.H., and P.T. Roberts, On the nature and origins of visibility-reducing aerosols in the Los Angeles air basin, *Atmospheric Environment*, **11**:803-812, 1977.

White, W.H., E.S. Macias, R.C. Ninger, and S. Schorran, Size-resolved measurement of light scattering by ambient particles in the southwestern U.S.A., *Atmospheric Environment*, **28**(50):909-921, 1994.